

QATAR UNIVERSITY

COLLEGE OF ARTS AND SCIENCES

NiP/ZnO-DOPED C<sub>3</sub>N<sub>4</sub> NANOCAPSULES: A NEW HIGHLY CORROSION-RESISTANT

ELECTROLESS-PLATED COATING WITH SUPERIOR MECHANICAL AND

ANTIBACTERIAL PROPERTIES

BY

FATMA FATHI MOHAMED NABHAN

A Thesis Submitted to

the College of Arts and Sciences

in Partial Fulfillment of the Requirements for the Degree of

Masters of Science in Material Science and Technology

June 2021

## COMMITTEE PAGE

The members of the Committee approve the Thesis of  
Fatma Fathi Nabhan defended on 28/04/2021.

---

Dr. Aboubakr M. Abdullah  
Thesis/Dissertation Supervisor

---

Prof. Ahmed Elzatahry  
Committee Member

---

Dr. Mohammad K. Hassan  
Committee Member

---

Prof. Talal Altahtamouni  
Committee Member

---

Dr. Kamel Eid  
Committee Member

Approved:

---

Ibrahim AlKaabi, Dean, College of Arts and Sciences

## ABSTRACT

NABHAN, FATMA F., Masters: June : 2021, Material Science and Technology

Title: NiP/ZnO-Doped C<sub>3</sub>N<sub>4</sub> Nanocapsules: a New Highly Corrosion-Resistant Electroless-Plated Coating with Superior Mechanical and Antibacterial Properties

Supervisor of Thesis: Dr. Aboubakr M. Abdullah.

Carbon nitride (C<sub>3</sub>N<sub>4</sub>) nanomaterials has superior mechanical, thermal and tribological properties, which make them attractive for various applications including corrosion resistant coatings. In this research, newly synthesized C<sub>3</sub>N<sub>4</sub>/ZnO nanocapsules with different concentrations (0.50, 1.00 and 2.00 g) of doped ZnO were incorporated in the NiP metallic coating using electroless deposition technique. The nanocomposite coating was heat treated at 400 °C for 1h. The as-plated and heat treated nanocomposite coatings were characterized for their structure, elemental composition, thickness, morphology, roughness, wettability, hardness and corrosion protection properties to evaluate the influence of undoped and doped C<sub>3</sub>N<sub>4</sub> with ZnO on the NiP coating. The results indicated that the microhardness of as-plated and heat treated nanocomposite coatings was significantly improved after the incorporation of undoped C<sub>3</sub>N<sub>4</sub> nanocapsules. About 21% further improvement is done with 0.5g ZnO doped C<sub>3</sub>N<sub>4</sub> nanocapsules, where the NiP-C<sub>3</sub>N<sub>4</sub>/0.5g ZnO composite coating showed the maximum microhardness of 680 and 1,330 HV<sub>200</sub>, before and after heat treatment, respectively. Electrochemical impedance spectroscopy (EIS) and potentiodynamic polarization (PP) outcomes revealed that the corrosion resistance of heat treated undoped and doped NiP- C<sub>3</sub>N<sub>4</sub> coatings are higher than the corresponding as-plated

ones. The highest corrosion resistance is achieved on the as-plated and heat treated NiP- $C_3N_4$  coatings that is doped with 1.00 g ZnO. Although the presence of ZnO in the  $C_3N_4$  capsules increased its surface area and porosity, the  $C_3N_4/ZnO$  nanocapsules prevent the localized corrosion and enhance the corrosion resistance of the nanocomposite coatings by filling the micro defects and pores of the NiP matrix. Furthermore, the colony counting method used to evaluate the antibacterial behavior of the as-plated and heat-treated coatings demonstrated superior antibacterial properties, namely after heat treatment. Therefore, the novel prospective  $C_3N_4/ZnO$  nanocapsules can be utilized as a reinforcement nanomaterial in improving the mechanical and anticorrosion performance of NiP metallic coatings in chloride media, together with providing superior antibacterial properties.

## DEDICATION

*This thesis is dedicated to my beloved mother, who always believed in me, and shined my life with her prayers and love, my dear father, who always empowered my soul with his encouraging words, and husband, my soulmate who always supported me with care, motivation, and love, and finally, my kids, the shining stars of my life.*

## ACKNOWLEDGMENTS

I would like to express my deepest appreciation to my supervisor, Dr. Aboubakr M. Abdullah, for his endless support and consistent guidance during the journey of working on this thesis. Without his supervision and persistent support, I could not have written this thesis in such a precise and concise manner.

My deepest gratitude goes also to Dr. Eman M. Fayyad who inspired me to optimally achieve this work on time. Despite all the challenges I faced, she always supported me and helped me overcome them all. Words cannot truly reflect my gratefulness to her limitless support, guidance, and persistent help that she provided with care, love, and patience.

In addition, I would like to thank Dr. Mostafa M. Selim for his continuous support to me, especially in the preparation of nanocapsules applied in my research and in solving some technical issues that encountered me in the lab. A special thank-you goes to Mr. Mohammed Saleh, Mr. Abdullah Ashraf, Eng. Yusuf Moinuddin Mohamed, and Dr. Peter Kasak for providing prompt help whenever needed, and for assisting me in characterizing and analyzing my samples. I am also thankful for Mr. Ahmad Bahghat, and Eng. Abdulrahman Mohammed Moussa for their endless cooperation, and for always giving me the priority to work on the Gamry device.

I am furthermore indebted to the central lab units (CLU) team for providing assistance in the SEM and TEM analysis of my samples. Finally, I would like to express my gratitude for my faculty, committee members, and colleagues in the “materials science and technology” master’s program for their support, constructive discussions, and valuable comments that motivated, benefited me and enriched my thesis.

## TABLE OF CONTENTS

DEDICATION.....	v
ACKNOWLEDGMENTS .....	vi
LIST OF TABLES.....	xi
LIST OF FIGURES .....	xii
Chapter 1: INTRODUCTION.....	1
1.1. Background .....	1
1.2. Thesis Outline .....	2
1.3. Thesis Objectives .....	4
Chapter 2: literature review .....	5
2.1 Introduction.....	5
2.2 Types of Coatings and Factors Affecting their Durability in Oil and Gas Industries .....	9
2.3 Electroless Plating Versus Electroplating Technique .....	11
2.4 Electroless Ni-P Coatings.....	14
2.4.1 Electroless NiP in Acidic Bath .....	19
2.4.2 Electroless in Alkaline Bath.....	19
2.5 Effect of Heat Treatment on Electroless NiP Coatings.....	20
2.6 Electroless Ni-P Composite Coatings and their Advantages .....	22
2.7 Properties of Electroless Ni-P and its Composites Coatings.....	24

2.7.1	Microstructure and Melting Point.....	24
2.7.2	Porosity and Density .....	26
2.7.3	Adhesion .....	26
2.7.4	Hardness and Ductility.....	27
2.7.5	Tensile Strength and Internal Stresses .....	27
2.7.6	Fatigue Properties .....	28
2.7.7	Wear and Corrosion Resistance .....	29
2.8	Application of Electroless Ni-P Coating in Oil and Gas Industry .....	30
2.9	Carbon Nitride (C <sub>3</sub> N <sub>4</sub> ) Materials and their Application in Corrosion Resistant Coatings.....	32
2.9.1	History, Structure, and Unique Properties of Carbon Nitride Materials	32
2.9.2	Preparation Methods and Various Shapes of Triazine-Based Graphitic Carbon Nitride Structures.....	35
2.9.3	Carbon Nitride in Polymer-based Coatings .....	36
2.9.4	Carbon Nitride Corrosion Resistant Thin films .....	40
2.9.5	Carbon Nitride Corrosion Resistant Multilayered systems .....	41
2.9.6	Carbon Nitride in Metallic based coatings.....	42
Chapter 3: Materials and Methodology .....		46
3.1	Materials.....	46
3.2	Preparation of C <sub>3</sub> N <sub>4</sub> Nanocapsules with and without ZnO as a Dopant .....	47



3.3	Pretreatment of Specimens.....	48
3.4	Electroless Deposition.....	50
3.5	Heat Treatment.....	51
3.6	Characterization .....	52
3.6.1	Structural analysis (XRD).....	52
3.6.2	Surface Morphology and Compositional Analysis .....	53
3.6.3	Surface roughness .....	56
3.6.4	Water Contact Angle (WCA).....	57
3.6.5	Mechanical analysis.....	58
3.6.6	Corrosion Study .....	60
3.6.7	Antibacterial Study .....	63
Chapter 4: Results and discussion.....		64
4.1	Structural Analysis (XRD).....	64
4.2	Morphology and Compositional Analysis.....	67
4.2.1	SEM Analysis .....	67
4.2.2	EDX Analysis .....	71
4.2.3	Cross Section Analysis .....	75
4.2.4	TEM Analysis .....	82
4.3	Surface Roughness (AFM) and Water Contact Angle (WCA) Measurements	

4.3.1	AFM Analysis .....	83
4.3.2	WCA Measurements .....	86
4.4	Mechanical Performance Analysis .....	89
4.4.1	Vicker's Microhardness Measurements .....	89
4.4.2	Nanoindentation Test .....	91
4.5	Electrochemical Corrosion Analysis .....	94
4.5.1	Electrochemical Impedance Spectroscopy (EIS) .....	94
4.5.2	Potentiodynamic polarization (Tafel curves) .....	107
4.6	Antibacterial Analysis .....	110
Chapter 5: Conclusions and Future work .....		115
Conclusions .....		115
Future Work .....		118
References .....		119
APPENDICES .....		139
<b>Appendix A:</b> TEM Analysis for C <sub>3</sub> N <sub>4</sub> /ZnO Nanocapsules .....		139
<b>Appendix B:</b> BET Measurements .....		140

## LIST OF TABLES

Table 1. Requirements for electroless NiP deposition process.....	16
Table 2. Summary of used materials.....	46
Table 3. Weight % composition of API-X120 C-Steel.....	48
Table 4. Operational parameters and bath constituents of electroless plating process	50
Table 5. EDX analysis for the elemental composition of the different as-plated coatings .....	72
Table 6. EDX analysis for the elemental composition of the different heat-treated coatings. ....	73
Table 7. Water contact angle (WCA) measurements for the different as-plated and heat- treated coatings. ....	88
Table 8. The penetration depths for the different coatings. ....	93
Table 9. EIS-equivalent circuits fitting parameters of the substrate and the as-plated NiP, NiP-C <sub>3</sub> N <sub>4</sub> and NiP-C <sub>3</sub> N <sub>4</sub> /ZnO nanocomposite coatings, with different concentrations of ZnO dopant, in 3.5 wt. % NaCl solution at room temperature. ....	102
Table 10. EIS-equivalent circuits fitting parameters of the heat-treated NiP, NiP-C <sub>3</sub> N <sub>4</sub> and NiP-C <sub>3</sub> N <sub>4</sub> /ZnO nanocomposite coatings, with different concentrations of ZnO dopant, in 3.5 wt. % NaCl solution at room temperature. ....	106
Table 11. Tafel fitting results of the different coatings before and after heat treatment. .....	109

## LIST OF FIGURES

Figure 1. Anticorrosive coating system in oil and gas industry, and the factors that affects its durability [34].....	10
Figure 2. Electroplating of Me metal with copper (Cu) [38].....	12
Figure 3. Schematic diagram for the general setup used in electroless plating technique [8].....	12
Figure 4. Uniform electroless coating compared to nonuniform coating from electroplating [3].....	13
Figure 5. The effect of heat treatment on hardness by heating NiP coating for 1 h, extracted from ref. [38].....	21
Figure 6. Triazine (a) and tri-s-triazine (b) crosslinked structures. Adapted from ref. [72].....	33
Figure 7. Schematic diagram of classified carbon nitride materials. Materials that are often named as graphitic carbon nitride (g-C <sub>3</sub> N <sub>4</sub> ) are indicated in the dashed box, extracted from ref. [11] .....	34
Figure 8. Various shapes and morphologies of g-C <sub>3</sub> N <sub>4</sub> materials. Retrieved from ref. [72].....	36
Figure 9. Potentiodynamic polarization curves of Q235 steel, pure epoxy, and g-C <sub>3</sub> N <sub>4</sub> /epoxy nanocomposite samples at different concentrations of C <sub>3</sub> N <sub>4</sub> nanosheets after 1 h immersion in (a) 3.5% NaCl and (b) 0.1 M H <sub>2</sub> SO <sub>4</sub> solution. Ref. [84].....	37
Figure 10. Photos of (a, a') epoxy coating, and (b, b') g-C <sub>3</sub> N <sub>4</sub> /epoxy nanocomposite coating containing 2 wt. % g-C <sub>3</sub> N <sub>4</sub> nanosheets, before and after adhesion test, respectively. Extracted from ref. [84] .....	38
Figure 11. (a) Plots of water uptake in epoxy coatings as a function of immersion time,	

(b) Schematic demonstration of reduced water absorption by epoxy coating upon the addition of nanofiller, adapted from ref. [18]. .....39

Figure 12. Tafel curves for uncoated and a-C:N coated (a) CoCrMo and (b) Silicon substrates deposited with various substrates bias [89].....41

Figure 13. Microhardness of as plated and heat treated electroless NiP and NiP-C<sub>3</sub>N<sub>4</sub> composite coatings in comparison to bare C-steel substrate [10].....44

Figure 14. Bode and phase angle plots (a, b) for C-steel substrate, as plated and heat treated electroless NiP, and NiP-C<sub>3</sub>N<sub>4</sub> nanocomposite coating [10]. .....44

Figure 15. Pretreatment steps for C-steel specimens: (a,b) grinding and polishing, (c) acetone sonication, and (d) alkaline cleaning .....49

Figure 16. (a) Electroless plating bath and (b) C-steel specimen coated with NiP- C<sub>3</sub>N<sub>4</sub>/ ZnO composite coating. ....51

Figure 17. MTI Tube furnace used for heat treatment of deposited specimens. ....51

Figure 18. Schematic of X-ray diffraction in solid crystals as stated by Bragg's law for constructive interference [96]. .....53

Figure 19. Scanning electron microscope (SEM), a schematic showing main components. [98].....54

Figure 20. SEM and EDX device that was utilized in the central lab units, Qatar University.....54

Figure 21. HRTEM device used for morphological imaging .....56

Figure 22. Asylum research atomic force microscope, MFP3D.....57

Figure 23. Interaction of water molecules with hydrophobic and hydrophilic surfaces. ....58

Figure 24. Graphical representation of sessile drop technique for measuring WCA. .58

Figure 25. Vicker's microhardness tester, Future-Tech Corp., Japan model .....	59
Figure 26. Typical Tafel polarization curve. Ref. [108].....	61
Figure 27. GAMRY 3000 device used for electrochemical measurements.....	62
Figure 28. Three electrodes configuration in the corrosion cell. ....	62
Figure 29. XRD pattern of NiP, NiP-C <sub>3</sub> N <sub>4</sub> , and NiP-C <sub>3</sub> N <sub>4</sub> /ZnO with different concentrations of doped ZnO (0.50, 1.00, and 2.00 g) (a) before and (b) after heat treatment at 400 °C for 1 h. ....	64
Figure 30. SEM images of (a,a') NiP, (b,b') NiP-C <sub>3</sub> N <sub>4</sub> , (c,c') NiP-C <sub>3</sub> N <sub>4</sub> / 0.50g ZnO, (d,d') NiP-C <sub>3</sub> N <sub>4</sub> / 1.00g ZnO, and (e,e') NiP-C <sub>3</sub> N <sub>4</sub> / 2.00g ZnO, before and after heat treatment at 400°C for 1 h. ....	70
Figure 31. Cross-sectional SEM image of (a) as-plated NiP coating, and (b-d) EDX mapping of its elements. ....	76
Figure 32. Cross-sectional SEM image of (a) heat-treated NiP coating, and (b-d) EDX mapping of its elements. ....	77
Figure 33. Cross-sectional SEM image of (a) as-plated NiP-C <sub>3</sub> N <sub>4</sub> coating, and (b-f) EDX mapping of its elements. ....	78
Figure 34. Cross-sectional SEM image of (a) heat-treated NiP-C <sub>3</sub> N <sub>4</sub> coating, and (b-f) EDX mapping of its elements. ....	79
Figure 35. Cross-sectional SEM image of (a) as-plated NiP-C <sub>3</sub> N <sub>4</sub> /0.5g ZnO coating, and (b-h) EDX mapping of its elements. ....	80
Figure 36. Cross-sectional SEM image of (a) heat-treated NiP-C <sub>3</sub> N <sub>4</sub> /0.5g ZnO coating, and (b-h) EDX mapping of its elements. ....	81
Figure 37. TEM images of (a) carbon nitride (C <sub>3</sub> N <sub>4</sub> ) nanocapsules, and (b) electroless coating of NiP-C <sub>3</sub> N <sub>4</sub> .....	82

Figure 38. AFM images of (a,a') NiP, (b,b') NiP-C<sub>3</sub>N<sub>4</sub>, (c,c') NiP-C<sub>3</sub>N<sub>4</sub>/0.5g ZnO, (d,d') NiP-C<sub>3</sub>N<sub>4</sub>/1.00g ZnO, and (e,e') NiP-C<sub>3</sub>N<sub>4</sub>/2.00g ZnO coatings, before and after heat treatment at 400°C for 1 h, respectively..... 85

Figure 39. Microharness measurements of the prepared NiP, and NiP- C<sub>3</sub>N<sub>4</sub>/ZnO, with different concentration of ZnO dopant (0.00, 0.50, 1.00 and 2.00 g), nanocomposite coatings before and after HT at 400 °C for 1h..... 91

Figure 40. Loading-unloading curves obtained from the nanoindentation test for NiP, NiP/C<sub>3</sub>N<sub>4</sub> and NiP- C<sub>3</sub>N<sub>4</sub>/ZnO nanocomposite coatings, with different concentrations (0.50, 1.00 and 2.00 g) of ZnO dopant, before and after heat treatment at 400 °C for 1h. .... 93

Figure 41. (a) Bode and (b) phase angle plots of the substrate and the as-plated NiP, NiP-C<sub>3</sub>N<sub>4</sub> and NiP-C<sub>3</sub>N<sub>4</sub>/ZnO nanocomposite coatings, with different concentrations of ZnO dopant, in 3.5 wt.% NaCl solution at room temperature ..... 96

Figure 42. Nyquist plots of (a) the substrate and (b) the as-plated NiP, NiP- C<sub>3</sub>N<sub>4</sub> and NiP- C<sub>3</sub>N<sub>4</sub>/ZnO nanocomposite coatings, with different concentrations of ZnO dopant, in 3.5 wt% NaCl solution at room temperature. Inset is the enlargement of the low frequency region. .... 98

Figure 43. Two-time constants equivalent circuit that fits the experimental impedance results of the different as-plated and heat-treated coatings..... 101

Figure 44. (a) Bode and (b) phase angle plots of the heat-treated NiP, NiP-C<sub>3</sub>N<sub>4</sub> (undoped) and NiP-C<sub>3</sub>N<sub>4</sub>/ZnO (doped) nanocomposite coatings, with different concentrations of ZnO dopant, in 3.5 wt% NaCl solution at room temperature. .... 105

Figure 45. Nyquist plots of the heat-treated NiP, NiP-C<sub>3</sub>N<sub>4</sub> (undoped) and NiP- C<sub>3</sub>N<sub>4</sub>/ZnO (doped) nanocomposite coatings, with different concentrations of ZnO

dopant, in 3.5 wt.% NaCl solution at room temperature. The inset is the enlargement of the low frequency regions.....	105
Figure 46. Tafel curves for a) the as-plated and b) the heat-treated NiP, NiP-C <sub>3</sub> N <sub>4</sub> (undoped) and NiP-C <sub>3</sub> N <sub>4</sub> /ZnO (doped) nanocomposite coatings, with different concentrations of ZnO dopant, in 3.5 wt% NaCl solution at room temperature. The heat treatment at 400 °C for 1h. The scan rate was 0.167 mV s <sup>-1</sup> . Tafel plot of the substrate is in a.....	109
Figure 47. Antibacterial activity of the different coupons, (a) Photographs of S.aureus exposed to substrate (A), NiP (B) and NiP-C <sub>3</sub> N <sub>4</sub> undoped (C), NiP-C <sub>3</sub> N <sub>4</sub> doped with 0.5 (D), 1.0 (E) and 2.0 g (F) ZnO nanocomposite coatings. (b) CFU of S.aureus bacterial cells.....	114
Figure 48. TEM measurements for C <sub>3</sub> N <sub>4</sub> nanocapules (undoped) (a), and doped C <sub>3</sub> N <sub>4</sub> with (b) 0.5, (c) 1.0 and (d) 2.0 g ZnO.....	139
Figure 49. N <sub>2</sub> adsorption-desorption isotherms at 77 K for mesoporous g-C <sub>3</sub> N <sub>4</sub> nanocapsules doped with (a) 0.0 , (b) 0.5 , (c) 1.0 and (d) 2.0g ZnO, respectively..	140
Figure 50. Pore size and volume characterization for mesoporous g-C <sub>3</sub> N <sub>4</sub> nanocapsules doped with (a) 0.0 , (b) 0.5 , (c) 1.0 , and (d) 2.0g ZnO, respectively.....	141



## CHAPTER 1: INTRODUCTION

### 1.1. Background

Corrosion is one of the major problems, which lead to great economic loss and catastrophic failures. The rising demands to enhance the corrosion protection methods, namely coatings, which are commonly used in oil and gas pipelines, automotive equipment, and various engineering applications, have recently encouraged extensive research [1]. Electroless deposited nickel phosphorous (NiP) coatings have specifically triggered researchers' interest, due to its superior hardness, corrosion and wear resistance [2]–[5]. Additionally, electroless NiP coatings will always form a uniform deposit on any shape of substrates, even the ones with complicated shapes [6], [7].

In electroless plating technique, NiP is autocatalytically deposited on the substrate by using a reducing agent, as a source of electrons, rather than applying external power [8]. Nevertheless, NiP coatings are still showing limitations in various aggressive environments, and numerous investigations have been conducted to enhance its overall performance and expand its applications. On the other hand, it is of great importance to reduce biocorrosion which is induced by the formation of bacterial film on the surface of pipelines. Various electroless NiP-based nanocomposite coatings were designed for this purpose, such as NiP-ND, NiP-PTFE, and NiP-TiNi. It was reported that these nanocomposites have significantly reduced the bacterial adhesion to the metal surface, which lead to enhanced antibacterial properties of the coated surfaces [9]. The incorporation of reinforcement particles in the NiP matrix, such as  $C_3N_4$ , have significantly enhanced the mechanical and corrosion resistance properties compared to pure electroless NiP coatings [10]. Despite all the significant properties of carbon nitride ( $C_3N_4$ ) nanomaterials, as being a hard material, and thermally and chemically stable [11], only few investigations have reported the use of such incredible material in

metallic NiP coatings.

Moreover, carbon nitride can be produced in various shapes, e.g. nanosheets, nanorods, nanoflowers, nanospheres, etc [12]–[16], however, only the use of C<sub>3</sub>N<sub>4</sub> nanosheets in electroless NiP coatings have been reported [10], [17]. Several researchers investigated the use of carbon nitride nanosheets as nanofillers in polymer-based matrix, which have greatly enhanced the surface protective and barrier performance of these coatings against corrosive environments [18]. However, to the best of our knowledge, none of these investigations has reported the antibacterial behavior of carbon nitride-incorporated protective coatings.

In this research, we aim to investigate the use of newly synthesized C<sub>3</sub>N<sub>4</sub> nanocapsules in electroless NiP coating, with and without zinc oxide (ZnO) as a dopant. The newly fabricated undoped C<sub>3</sub>N<sub>4</sub> nanocapsules and doped one with different concentrations (0.50, 1.00 and 2.00 g) of ZnO dopant, are incorporated in the electroless NiP matrix, and its effect on the physical, chemical, mechanical and corrosion, and antibacterial properties of NiP-nanocomposite coating is studied. Moreover, this work explores the impact of heat treatment on the physical, mechanical, corrosion resistance, and antibacterial properties of the prepared undoped and doped NiP-C<sub>3</sub>N<sub>4</sub> nanocomposite coatings.

## 1.2. Thesis Outline

### ➤ **Chapter 1: Introduction**

This chapter basically introduces the topic of the thesis. It highlights the corrosion problem, and the importance of finding durable mitigation methods, such as using hard and highly corrosion resistant coatings. The recent advances and research findings in this field are addressed, and the gap in literature, specifically in regards to previous research work related to electroless NiP-matrix nanocomposite coating, are

highlighted.

➤ **Chapter 2: Literature review**

This chapter discusses the metallic coatings used in oil and gas industries, and it focuses on electroless nickel phosphorous (ENP) coatings and its composites.

The literature review will mainly summarize all the previous research work relevant to electroless NiP coating. Additionally, this chapter will provide a thorough image of some important types of metallic nanocomposite electroless NiP coatings that are beneficial for oil and gas industries, based on the research work that was achieved recently. Moreover, some basic techniques used for synthesizing these coatings, which reflect on their various interesting properties, durability, and marketability, are highlighted. It also provides a description of the advantages of electroless plating over the electroplating technique, and the different conditions that should be considered to enhance the properties of electroless NiP-based metallic composite coatings.

Furthermore, this chapter highlights the gaps in the literature, and how this research is going to fill one or more of these gaps. Moreover, a clear statement of the research hypothesis for the selected thesis topic is written.

➤ **Chapter 3: Research methodology**

This chapter includes the methods/techniques used in the proposed research, materials, detailed experimental procedures, characterization techniques, and methods used for data collection and data analysis.

➤ **Chapter 4: Results and discussion**

The main findings and results from the experimental work are properly presented in this chapter. The obtained findings and outcomes are also discussed in this chapter, and compared with other previous work reported in the literature.

➤ **Chapter 5: Conclusions and future work**

Main conclusions are finally summarized, in addition to highlighting the limitations of the current research. Finally, some recommendations for possible applications and future research are included.

### 1.3. Thesis Objectives

The main objective of this research is to investigate a newly synthesized NiP-C<sub>3</sub>N<sub>4</sub>/ ZnO nanocomposite coating for its physical, chemical, mechanical, corrosion and antibacterial properties. In this work, our main objectives are:

- To synthesis the nanocapsules of graphitic C<sub>3</sub>N<sub>4</sub> with and without ZnO as a dopant.
- To prepare electroless corrosion resistant NiP-C<sub>3</sub>N<sub>4</sub> nanocomposite coatings through the incorporation of undoped and doped C<sub>3</sub>N<sub>4</sub> nanocapsules.
- To characterize the prepared novel NiP-C<sub>3</sub>N<sub>4</sub>/ZnO nanocomposite coatings, for its physical, chemical, mechanical, antibacterial and corrosion properties.
- To investigate the effect of heat treatment on the physical, mechanical, antibacterial and corrosion resistance properties of the prepared NiP-C<sub>3</sub>N<sub>4</sub>/ZnO nanocomposite coatings.

## CHAPTER 2: LITERATURE REVIEW

### 2.1 Introduction

Corrosion is a natural phenomenon that attacks metals and alloys in an effort to return them to their original state. Many factors increase the corrosion rate of metals, such as temperature, the relative size of anodic and cathodic areas involved, and the type of electrolyte. Electrolytes, can be very aggressive and cause metals to corrode, which commonly can be water, acids or alkalis [19].

Nowadays, metals and alloys are used in various applications, e.g. carbon steel is widely used in most industrial pipelines and engineering tools and equipment, where they are in direct contact with acidic, water of high salt content or aggressive environments, which is often accompanied with problems related to corrosion. Accordingly, it is of great interest to prevent corrosion by applying protection methods that are durable and effective [20]. Generally, it is hard to stop corrosion completely, but the corrosion rate can be decreased by applying several methods, such as anodic protection, cathodic protection, addition of inhibitors, and using protective coatings [21]. Coatings are usually used to prevent corrosion by eliminating the contact between the metal surface and its surrounding, or sometimes by acting as sacrificial surfaces [17]. In many cases coatings help in improving the surface properties of the substrate, such as the corrosion and wear resistance, wettability, and other properties based on the type of applied coating [22]. Generally, the types of coatings are categorized as organic and inorganic. Organic coatings are based on organic binders, such as zinc epoxy, whereas inorganic coatings are based on silicate, ceramic or metallic materials, e.g. zinc silicate based coatings, TiN, Al<sub>2</sub>O<sub>3</sub>, etc. [23].

Many types of coatings, such as epoxy-based coatings, polymer tapes, and

several composite coatings were developed for protecting the industrial pipelines from corrosion, namely in oil and gas industries. However, they have shown various limitations when tested in aggressive and highly corrosive environments [24]. Accordingly, researchers have developed metallic coatings using different techniques, such as electroplating, mechanical plating, and electroless plating, where each technique has its own advantages and disadvantages in terms of the handling process and coating properties [25], [26].

Recently, due to its relatively high wear resistance, microhardness, and corrosion resistance properties, electroless nickel phosphorous (Ni-P) coatings are considered one of the best choices for industrial pipelines. Also NiP coatings have so many other advantages, such as forming a uniform deposit on any shape of substrates, even with intricate shapes [6]. Furthermore, electroless deposition technique is an autocatalytic process which occurs by using a reducing agent as a source of electrons, rather than using external power [10]. In spite of all the attractive properties of NiP coatings, researchers are still trying to improve its overall performance.

Doping of NiP matrix with various types of particulates was widely investigated and revealed significant enhancement in the physical, mechanical, corrosion and wear resistance of the electroless NiP metallic coating [4]. Depending on the type of doped organic or inorganic material, the NiP composite coatings can be categorized as lubricating and wear resistant. Co-deposition of solid lubricants such as graphite and MoS<sub>2</sub> reduces the friction coefficient of the NiP composite coating compared to blank electroless NiP coating, whereas doping with hard materials such as diamond and SiC increases its hardness and wear resistance [27].

Many researchers succeeded to incorporate various different nanoparticles in the NiP matrix, which significantly enhanced the overall properties of electroless NiP

coatings, namely mechanical, corrosion, and wear resistance, e.g.  $ZrO_2$ ,  $TiO_2$ ,  $Al_2O_3$ ,  $C_3N_4$ , etc. Other types of incorporated nanomaterials in electroless NiP, such as TiNi, enhanced the coating's antibacterial properties, in addition to the mechanical and anticorrosion performance [28]. Hence, various nanoparticles potentially can be used to improve the electroless NiP coating performance against biocorrosion, by reducing the bacterial adhesion on its surface [29], [30].

Fayyad et al. have synthesized a novel NiP- $C_3N_4$  nanocomposite through the co-deposition of  $C_3N_4$  nanosheets with the NiP matrix, which resulted in a significant enhancement in the microhardness and corrosion resistance properties compared with pure NiP coating [10].

In fact, carbon nitride ( $C_3N_4$ ) nanomaterials have significant properties, which open the door for many future advancements and applications. It is a very hard material, as hard as diamond, and thermally and chemically stable [11]. Consequently, such incredible nanomaterial will definitely outperform when added to NiP matrix. Moreover, carbon nitride possesses a novel photocatalytic activity in the visible light region and can be synthesized in different shapes, e.g. nanosheets, nanorods, nanoflowers, nanospheres, etc. [12]–[16]. Numerous investigations has reported the enhancement of photocatalytic activity of carbon nitride as the shape of  $C_3N_4$  nanoparticles is changed [31]. As the photocatalytic activity of  $C_3N_4$  nanomaterials is varied as its shape changes, this would also be expected to have an impact on the corrosion resistance applications. Only few reports have investigated the effect of  $C_3N_4$  nanosheets on the physical, mechanical and corrosion resistance of electroless NiP coatings [10], [17]. Kumar et al. reported an improvement in the corrosion resistance performance of pure epoxy (PE) nanocomposite coating by using ZnO doped – graphitic carbon nitride (ZnO/GCN) nanosheets as a nanofiller in the epoxy (PE)

matrix. The corrosion assessment in their research showed that ZnO/GCN nanosheets have greatly enhanced the surface protective and barrier performance of PE against corrosive 3.5% NaCl environment [18]. However, to the best of our knowledge, the effect of using different shapes, morphology and nature of  $C_3N_4$  nanomaterial on the corrosion performance of metallic NiP coatings has not been addressed yet. Moreover, the antibacterial behavior of  $C_3N_4$ -incorporated NiP composite coating, has never been investigated before.

This chapter describes the types of coatings that are commonly used in oil and gas industry, and the factors that influence their durability, and sheds light specifically on electroless nickel phosphorous (ENP) coatings. It also defines the electroless deposition technique, and provides a thorough image of some important types of metallic nanocomposite ENP coatings that are beneficial for oil and gas industries, based on the research work that was achieved recently. Additionally, the techniques used for synthesizing these coatings, which reflect on their various interesting properties, durability, and marketability are highlighted. Moreover, the advantages of electroless plating over the electroplating technique and the different conditions that should be considered to enhance the properties of electroless NiP-based metallic composite coatings are described in this chapter. Furthermore, the literature review focuses on  $C_3N_4$  nanomaterials, which have numerous unique properties, making them very attractive in various applications, such as photocatalysis, biomedical, and most importantly corrosion resistant composite coatings. The structure, synthesis, various shapes, and unique properties of  $C_3N_4$  nanomaterials will be described. Finally, the important types of  $C_3N_4$ -incorporated coatings that were recently investigated and revealed enhancement in the mechanical, wear, and corrosion resistance properties of various coatings are comprehensively discussed.



## 2.2 Types of Coatings and Factors Affecting their Durability in Oil and Gas Industries

According to statistical reports, one-third of the energy supply today comes from oil and gas industry. In this field, several types of metal or alloy-based equipment are used for extracting oil and gas from underground, such as drills, pumps, and separators, as well as, pipeline systems that are used for transporting petroleum products. However, these units are continuously subjected to corrosion problems, which are sometimes accompanied with erosion due to the aggressive environment, and the nature of constant-thrashing processes, such as drilling. Consequently, it was found that 25% of failures experienced in oil and gas industry are associated with corrosion problems, where more than 50% of these failures occur due to internal and external corrosion of pipelines [32]. Accordingly, to reduce this risk, which indeed reflects negatively on the production process, researchers have been trying to understand the corrosion mechanisms, and design mitigation strategies to increase the lifecycle of equipment and pipelines.

Coating surfaces is one of the most important mitigation approaches available in industrial pipelines to prevent corrosion. These coatings either perform as a barrier or provide sacrificial protection, i.e. protection is attained by sacrificial corrosion of an electrochemically more active metal, which is in electrical contact with the substrate [33]. Generally, the types of surface coatings applied in oil and gas industries can be categorized as metallic, organic, and inorganic. All these types have been widely used for the protection of pipelines and various industrial equipment against corrosion. However, coatings different from metallic ones have shown limitations at specific conditions, mostly at high temperatures and harsh conditions, especially for long-term

protection [34]. The coating failures that occur in oil and gas industries are mainly a result of the complicated coating-substrate system and the numerous number of parameters involved in the different processes. Figure (1) below represents a schematic diagram of the various factors that affect the durability of anticorrosive coating systems in oil and gas industry.

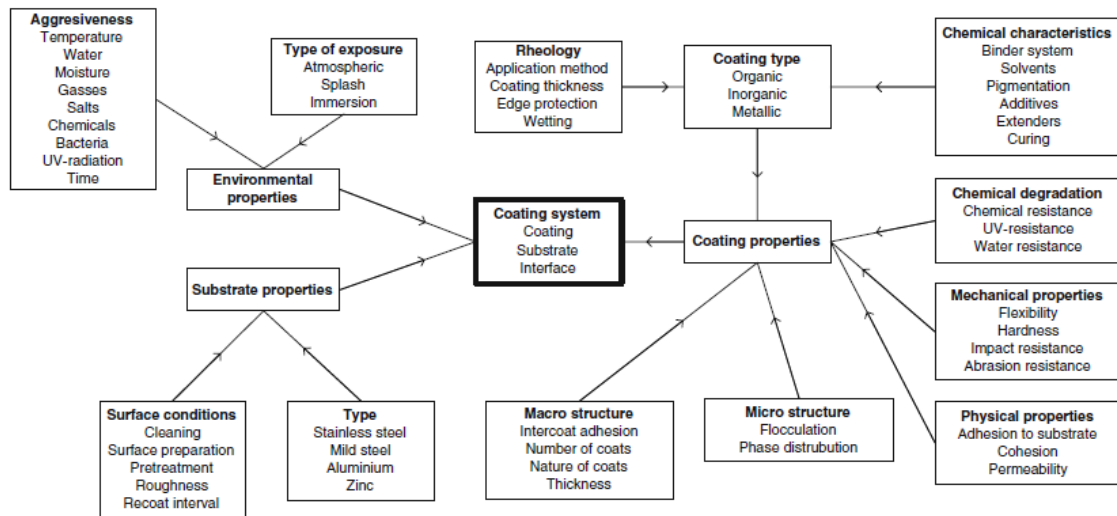


Figure 1. Anticorrosive coating system in oil and gas industry, and the factors that affects its durability [34]

Therefore, to design an anticorrosive coating that can perform effectively in this aggressive environment, it must be intrinsically durable, tough, flexible, and adhesive to the substrate to a high extent. Additionally, it should possess other superior mechanical properties to withstand stress, weathering, and mechanical abuse. It is also important to take into consideration that some external parameters affect the durability of a coating, such as the substrate type, coating thickness, and pretreatment of substrate, as well as, the coating composition, can highly affect the performance of the anticorrosive coatings [35].

Metallic coatings have shown outstanding properties and durability, which expanded their usage for many applications, namely in oil and gas industries. The most commonly used techniques for metallic coating are electrolytic, electroless, and mechanical deposition, as well as, hot dipping. However, metallic coatings produced by electroless deposition have shown distinctive characteristics, which made this method the most marketable compared to other techniques. In addition to the desirable properties obtained by this technique, it can be applied to any type of substrate material, and it is easy to handle [36]. In the following sections, a special type of metallic coating, i.e. electroless NiP-based coatings, will be the focus of this review.

### 2.3 Electroless Plating Versus Electroplating Technique

Metallic coatings can be achieved using two methods, electroplating and electroless plating. Electroplating (or electrodeposition) is referred to the use of electrical power to deposit a thin layer of metal atoms on top of a substrate [37]. In this method, an electric current is passed through a solution that conducts electricity called an electrolyte. To create this current two electrodes are dipped into the electrolyte solution and connected to an electric power supply, where the positively charged electrode is the anode, and the negatively charged electrode is the cathode. The electrodes and electrolyte are carefully chosen based on the type of material that needs to be plated on a specific substrate. As a result, the plating is accomplished when metal ions are reduced to metal atoms, which are eventually deposited at the cathode (substrate). Figure (2) shows the electroplating of Me metal with copper as an example [38].

On the other hand, electroless plating does not require electricity. In this technique, the plating is achieved by the use of a series of chemical reactions carried

out simultaneously that result in the deposition of a metal, evenly, across the surface of a substrate. In other words, electroless plating is a catalytic reduction process in which a reducing agent is used in an electrolyte containing the soluble salt of the coating metal to reduce the metal ion into the metal state. This process results in an evenly deposited metal layer at the surface of the inferior metal without the use of electricity [8]. The general setup for electroless plating process is shown in figure (3).

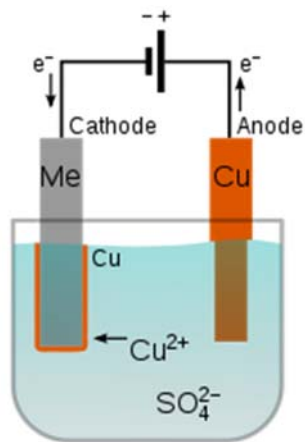


Figure 2. Electroplating of Me metal with copper (Cu) [38].

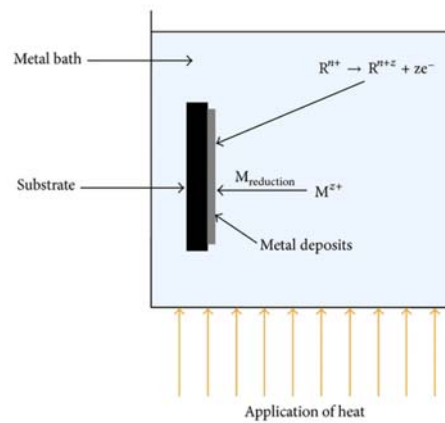


Figure 3. Schematic diagram for the general setup used in electroless plating technique [8].

Actually, both electro and electroless plating are considered to be effective techniques for surface coating. However, the selection of the suitable method to be utilized in a specific application mainly depends on the chemical composition of the substrate that need to be plated, as well as, the type of metal used for plating.

There are many advantages of electroless plating technique over the electroplating, one of them is related to the uniform thickness of the electroless coating all over the plated metal. Figure (4) shows a schematic diagram for the uniform electroless coating compared to the electroplated one. Additionally, the superior mechanical properties of the electroless deposit are also uniform all over the coating thickness, due to the uniformity of the deposit. Furthermore, electroless plating technique can be used for any kind of object, metal or non-metal, as electrical energy is not required. Unlike electroplating in which the cathode (substrate) has to be conductive to allow for the current to flow and the metal particles of the deposit bind to it. Moreover, high deposition rate of around 20-22 mm/hr., can be achieved by electroless plating. This rate is considered appropriately fast for industrial applications, and can be accomplished by the correct selection of the solution pH, composition and the operating temperature. On the other hand, due to the recent advancements in electroless coatings, great improvements have been achieved in the ductility of electroless deposits, namely nickel-based deposits, which in turn lead to the easiness of post-plating processes such as forming or pressing [3].

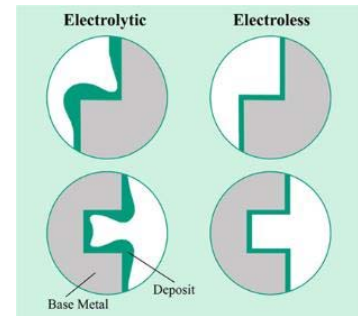


Figure 4. Uniform electroless coating compared to nonuniform coating from electroplating [3].

In oil and gas industries specifically, electroless coatings are essential for plating the internal parts of pipes and some other equipment and tools, such as pumps,

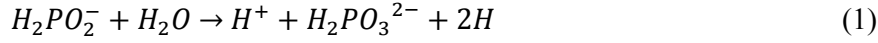
valves, and risers. It is mainly because they can uniformly plate items with complicated geometries [17]. Electroless NiP coating is an ideal type of coating for metals and alloys used in many industries, which will be discussed in more details throughout the following sections.

#### 2.4 Electroless Ni-P Coatings

The credit of inventing electroless nickel plating goes to Brenner and Riddell in 1946 as they were the first ones to discover the unusual reducing properties of the hypophosphites. They came up with their invention through their work in developing a plating process for the internal walls of tubes using an alloy called nickel-tungsten with an insoluble anode. Since that time, this type of coating has been implemented for many industrial applications for its outstanding corrosion and wear resistance [39].

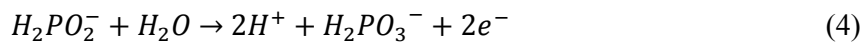
More than 95% of the electroless coatings in the industry are composed of electroless NiP. These coatings are classified in three main categories based on the phosphorus level: low (1 - 7 wt. %), medium (7 – 10 wt. %), and high (10 – 12 wt. %) phosphorus content. Generally, the higher the phosphorus content in Ni-P coatings, the better the corrosion and wear resistance. Additionally, the phosphorus level highly affects the metallurgical properties of alloys [40].

The kinetics of NiP coatings using electroless process was well described by Gould et al. and others [41]. The reaction kinetics are based on several main steps, starting first with the capacities of atomic hydrogen that are formed and adsorbed by the surface of the metal. Then the nickel ions ( $\text{Ni}^{2+}$ ) and hypophosphite ions are reduced, and the nickel and phosphorus atoms are co-deposited on the surface of the metal. The following equations represent the chemical reactions that occur in the deposition of electroless NiP [42].



As clarified in the reactions (1-3), the hypophosphite ions ( $H_2PO_2^-$ ) react with water, which result in producing hydrogen atoms that are desorbed onto the surface of the metal. Next the ions present in the bath, i.e. nickel ( $Ni^{2+}$ ) and hypophosphite ( $H_2PO_2^-$ ) ions, are reduced by the produced hydrogen atom, hence codepositing nickel and phosphorus (Ni-P) are formed, Then the atomic hydrogen is adsorbed into the formed deposit of Ni-P, and a new Ni and P are co-deposited. Finally, the adsorbed atomic hydrogen is consumed, leading to the co-deposition of nickel and phosphorus.

On the other hand, as electroless NiP plating is considered a catalytic process, the electrochemical mechanism by which the plating happens is summarized as the following. It is assumed that a catalytic oxidation occurs for the hypophosphite ions, whereas nickel and hydrogen ions undergo a reduction reaction along the catalytic surface. The anodic reaction is given as follows,



While the cathodic reactions are given as,



It is important to understand the challenges associated with the above mentioned chemical reactions in the electroless plating process. Actually, some reactions can be unfavorable during the deposition, for instance, instead of forming atomic hydrogen

during the reactions of hypophosphite with water, molecular hydrogen can be formed. This diminishes the reducing influence and is actually destructive for the deposition. Another issue is related to the reduction of nickel concentration in the bath due to the precipitation of nickel as nickel orthophosphate. These precipitates can deposit on the coating, generating a rougher coating [43]. Consequently, the efficiency of the electroless NiP coating will be reduced. In order to solve these issues, the addition of complexing agent is very important, which will stop the formation of Ni<sup>2+</sup> precipitates. Examples of complexing agents can be some organic acids such as succinic, tartaric, and maleic acid. Also, some of these organic acids can be added to reduce the speed of Ni-P deposition, and to prevent the creation of a porous coating [42].

Generally, there are some key requirements for the electroless process of NiP deposition [10], which can be summarized in the following table:

Table 1. Requirements for electroless NiP deposition process.

<b>Requirement</b>	<b>Example</b>	<b>Function</b>
Ni <sup>2+</sup> ions source	nickel chloride or nickel sulfate	Ni <sup>2+</sup> ions accept electrons from the electron donor (reducing agent), and get reduced to Ni metal atoms, which are deposited on the surface of the substrate.
Reducing agent	Sodium hypophosphite monohydrate	- The source of electrons (or electron donor) required to reduce Ni <sup>2+</sup> ions. - Helps in reducing nickel ions to metal and source of the phosphorus portion of the deposited alloy.



		<ul style="list-style-type: none"> <li>- Using sodium hypophosphite bath produces highly corrosion resistant NiP coating.</li> </ul>
Complexing agents	<p>organic acids or their salts, such as malic, acetic, citric or succinic</p>	<ul style="list-style-type: none"> <li>- They act as a controller for the electroless reactions and inhibit solution decomposition.</li> <li>- Also, act as buffers and prevent the precipitation of nickel phosphite</li> <li>- Generally affects the deposit's quality, porosity level and internal stress.</li> </ul>
Stabilizers or accelerators	<ul style="list-style-type: none"> <li>- Some of the most frequently used stabilizers are As, Mo, Sn, Pb, Cd, thioureas, and malic.</li> <li>- Succinic acid is widely used as an accelerator.</li> </ul>	<ul style="list-style-type: none"> <li>- They increase the rate of deposition.</li> <li>- Facilitate the phosphorus adsorption onto the surface of the catalyst, as it helps to weaken the bond between phosphorus hydrogen atoms in hypophosphite.</li> </ul>

Heating/Temperature	The electroless NiP deposition occurs at 60 °C temperatures and above	<ul style="list-style-type: none"> <li>- To obtain a high quality electroless coating, temperatures have to be controlled, as it affects the rates of deposition reactions and its kinetics</li> <li>- The temperature is exponentially proportional to the plating rate. Accordingly, an increase in the bath temperature results in an exponential increase in the plating rate.</li> <li>- On the other hand, a very high temperature is undesirable for the electroless bath as it leads to instability. As reported, the optimum operating temperature ranges from 85 to 90 °C.</li> <li>- Bath temperatures more than 90 °C, result in increased potential for solution decomposition, as a result of the decreased phosphorus content in the deposit.</li> </ul>
pH regulator	sodium hydroxide or sulfuric acid	<ul style="list-style-type: none"> <li>- It controls the pH with deposition time</li> <li>- It is crucial to control the pH, as it reflects on the phosphorus content in the deposit, As the pH value increases, the phosphorus content in the deposit is less, and vice versa.</li> </ul>

#### *2.4.1 Electroless NiP in Acidic Bath*

As established by Brenner and Riddell [39], the composition stability in acidic baths of electroless NiP is higher than alkaline baths. Therefore, acid baths are more advantageous in the electroless process as they provide high quality coatings, better deposition and thickness levels, as well as, contributing to having no loss of complexant by evaporation.

The use of acid baths in electroless NiP deposition provide easiness in controlling the amount of phosphorus content present in the deposit. In fact, regulating the percentage of phosphorus content leads to controlling the properties of the obtained deposit. Moreover, acidic baths are thermally stable, which means that even when they undergo heating they are not decomposed [44]. Accordingly, in oil and gas industries, acid solutions are selected, namely for corrosion protection applications.

#### *2.4.2 Electroless in Alkaline Bath*

Unlike acid bath, alkaline bath is disadvantageous in the electroless NiP deposition as it is thermally unstable, i.e. decompose at high temperatures. Additionally, it is very hard to control the pH at high temperature (higher than 90 °C), due to the loss of ammonia which is added to increase the bath pH. Furthermore, alkaline baths provide deposits with lower corrosion resistance and adhesion, which does not provide a thick layer of coating, and cannot be used for plating metal substrates like steel. This is explained by the increase in hypophosphite levels which is directly proportional to the rate of nickel deposition. Thus, the bath becomes unstable as a consequence of homogeneous deposition in the bulk [44].

## 2.5 Effect of Heat Treatment on Electroless NiP Coatings

Heat treatment is considered a very important step in the preparation of the electroless NiP coatings, as it greatly enhances the hardness and wear resistance. Annealing temperatures up to around 350 °C can sufficiently increase these properties [45]. In fact, heat treatment also affects the structure of electroless NiP coatings, and influences many other properties. If an as-deposited electroless NiP coating is annealed/heated at various temperatures, it passes through changes in its structure. Generally, these structural changes can be different depending on the microcrystalline nickel constituent and phases present in the coating. There are two different behaviors that can be shown; either as an alloy, in the amorphous phase and microcrystalline nickel is not a major constituent in it, or as a deposited-state alloy which have microcrystalline Ni as a major component. However, reports show that annealing consistently lowers the corrosion resistance of electroless coatings. As reported, a deposited coating containing microcrystalline Ni as a prime constituent and 10.8% of phosphorus can be heat-treated under a temperature range of 200 - 300 °C, with annealing time of 4 hours. In this case, the annealing process causes the formation of some phases, which include Ni<sub>12</sub>P<sub>5</sub> and Ni<sub>3</sub>P under all temperatures. Moreover, when the coating is annealed at above 400 – 600 °C, phases of Ni<sub>3</sub>P and Ni microcrystalline are detected [46].

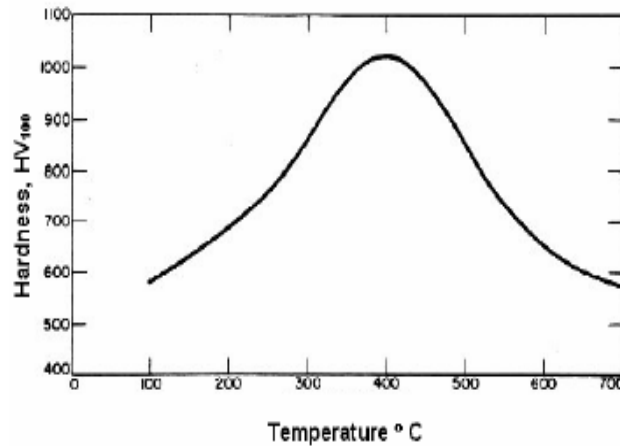


Figure 5. The effect of heat treatment on hardness by heating NiP coating for 1 h, extracted from ref. [38]

Actually, the reason of the increase in hardness upon heating the electroless NiP coating, precisely for around 1 hour at a temperature of 300-400 °C, is mainly referred to the Ni<sub>3</sub>P phase that is formed at this temperature range. Figure (5) shows the heat treatment effect on the hardness through heating an electroless NiP coating for 1 hour [38]. Nevertheless, at temperatures higher than 400°C, the hardness starts to be decreased as lattice defects start forming, and Ni<sub>3</sub>P particles become coarser [47].

The properties of NiP alloys in the amorphous phase were studied under the influence of annealing at low temperature by Zhao et al [48]. The results have shown a decrease in microhardness at the beginning, then it started to increase gradually during the time of heating/annealing. Other results included noticeable changes in some properties including wear resistance, frictional properties, as well as, conductivity, and resistivity [42], [49]. Another study considered the corrosion resistance properties of electroless NiP deposit containing 10.6% phosphorus. It was shown that increasing the annealing temperature sufficiently decreased the corrosion resistance[50].

## 2.6 Electroless Ni-P Composite Coatings and their Advantages

Heat treatment is not the only method that can enhance the properties of electroless NiP coatings, namely the hardness, wear resistance, and corrosion resistance. However, the addition of some reinforcements, such as nanoparticles were reported to greatly enhance their overall properties. As mentioned earlier, the most important advantages of electroless NiP coating are mainly related to the outstanding adhesion and wear and corrosion resistances. Another advantage is related to the uniformity of the electroless coatings, in general, which can be applied for any geometrical shapes, no matter how complex they are. However, the mechanical properties of pure electroless NiP coatings still need further improvements in order to broaden their applications, specifically in harsh environments, like the ones present in the industrial processes.

Reinforcements such as titanium dioxide ( $\text{TiO}_2$ ), alumina ( $\text{Al}_2\text{O}_3$ ), and silicon carbide (SiC) were extensively studied in synthesizing electroless NiP-based nanocomposites with superior properties that can be advantageous for oil and gas applications. These additives could greatly enhance the durability, thermal and chemical stability of the coating, as well as, the hardness and wear resistance [3], [42].

Recently, a lot of research work has been achieved on electroless NiP nanocomposites by utilizing the attractive properties of different materials, namely nanomaterials, which greatly enhanced the mechanical properties, wear and corrosion resistance compared to the original electroless NiP coating. For instance, Fayyad et al. have synthesized a novel NiP-  $\text{C}_3\text{N}_4$  nanocomposite through the co-deposition of  $\text{C}_3\text{N}_4$  nanosheets with the NiP matrix, which resulted in a significant enhancement in the microhardness and corrosion resistance properties compared with NiP coating [10]. In

fact, the properties of carbon nitride ( $C_3N_4$ ) nanomaterials are very attractive, which opens the door for many future advancements and applications. It is a very hard material, as hard as diamond, and thermally and chemically stable [51]. Consequently, it is expected that using such materials in NiP nanocomposite coatings will significantly enhance the mechanical, thermal, and corrosion resistance properties.

At the beginning, researchers were unsuccessful to prepare NiP composite coatings [3]. They found that the addition of fine particles resulted in having an unstable bath, as they increased the surface area of the bath. After that, they were able to overcome this challenge by adding an appropriate stabilizer, and they could easily prepare electroless Ni-P composite coatings. One of the most important requirements for a durable composite coating is having a high cohesion between the electroless NiP matrix and the added particles. Conditions, such as stability of the bath, agitation, size and concentration of added particles, as well as, the surfactant type, all play a significant role in promoting the quality of prepared electroless NiP based composite coatings [52].

To enhance the bath stability, malic acid or thiourea can be used [53]. On the other hand, agitation is crucial to prevent the suspended hard particles from rotating. Accordingly, in order to obstruct them in the prepared deposit/coating, it is important to keep their surfaces in the upward orientation. Moreover, it is well established that the particles distribution in the prepared electroless NiP nanocomposite coatings is critically accompanied with the size and concentration of the added particles. Accordingly, it is highly important to select the appropriate size and shape of the particles, and make sure that they are well suspended. In addition, added particles must contain no impurities, and should be insoluble in the bath. Additionally, to avoid agglomeration of the added particles, appropriate concentration must be used in the bath [54].

Properties of prepared electroless NiP-based nanocomposites differ from one another, depending on many factors including, the type and concentration of added nanoparticles and their properties, as well as, the added surfactant. For instance, hardness of electroless NiP coating can be increased by adding 25 vol. % of silicon carbide (SiC) to the bath, while adding the same amount of different material may decrease its hardness, such as polytetrafluoroethylene (PTFE) [55]. Appropriate surfactants also must be selected to make sure that the added particles are highly incorporated within the matrix. Examples of some used surfactants that uniformly distribute PTFE particles in electroless NiP matrix can be acetyl trimethyl ammonium bromide and polyvinylpyrrolidone [42].

Lately, new types of additives for preparing electroless nanocomposite coatings has triggered researchers' interests. Some examples include carbon nitrides ( $C_3N_4$ ) [10], Silicon oxide ( $SiO_2$ ) [56], carbon nanotubes (CNTs) [57], ferrites [58], hexaferrites [59], zinc oxide ZnO [60], and  $Al_2O_3-TiO_2$  [61]. These types of nanocomposites can open the potential for a wide range of applications in the future.

## 2.7 Properties of Electroless Ni-P and its Composites Coatings

### 2.7.1 *Microstructure and Melting Point*

It is very important to study the microstructural characteristics of electroless NiP coatings, as they are directly related to their properties. Also, understanding the microstructure of the deposits assists us to recognize the deposition mechanism and to evaluate the electroless coatings properties.

Actually, the phosphorus level present in the electroless deposit plays a key role in changing the microstructure and the resulting properties. Although the microstructure of electroless NiP deposits is still not very clearly explained, it has been described as to be amorphous, crystalline, or in between where both structures co-exist.



It is reported that generally electroless NiP coatings with low phosphorus content (1 - 5 wt. % P) have a crystalline structure, whereas coatings with a medium level of phosphorus content (6 - 9 wt. % P) consists of both amorphous and crystalline, and those that have high phosphorus level (10 -13 wt. % P) are amorphous. If they undergo annealing/heating they crystallize to nickel and several forms of nickel phosphides [42], [62].

Moreover, the crystallinity degree is affected by various factors (besides the phosphorus content), which in turn reflects on the resulting properties. Some of these factors include temperature and time of heat treatment, rate of heating, as well as, the thermal history. The effect of heat treatment on the microstructural transformation of electroless NiP coating from amorphous to crystalline has been extensively studied by Zhang and Yao [62]. They reported that added particles such as titanium dioxide (TiO<sub>2</sub>) did not influence the structure of the electroless NiP matrix at all. However, others particles were found to alter the nickel crystallite orientation, examples of these particles include: B<sub>4</sub>C and SiC [63].

The melting point of electroless NiP coating depends on the microstructure of the deposit and the presence of any impurities (if any) in the coating. Pure nickel has a melting point of 1455 °C, which is very close to the melting point of electroless NiP - that deposited from electroless bath containing hydrazine reducing agent - having a  $T_m = 1440 \text{ °C} \pm 1.0 \text{ °C}$ . Based on previous studies, the melting point of electroless decreases with the proportional increase of codeposited alloying elements, such as phosphorous, boron, lead, etc., as well as, co-deposited organic or inorganic impurities. For instance, the melting point of electroless NiP deposits that have phosphorus content of 7.9 wt. % is 890 °C [37].

### 2.7.2 Porosity and Density

In general, nickel-based coatings produced by electrodeposition technique have higher or equal porosity than electroless nickel-based deposits, namely under similar thickness and identical conditions of surface preparation. Additionally, annealing or heat treatment result in lowering the porosity of Ni-based coatings, accordingly, higher corrosion resistance is obtained from electroless Ni-based coatings than electrodeposited ones of equal thickness. Multistage deposition can be also carried out for further reduction of the porosity in electroless NiP coatings. Generally, it is important to reduce the porosity of a coating in order to reduce the corrosion potentials [64].

On the other hand, as the phosphorus content increases, the density of electroless NiP coating decreases, thus the density of the electroless NiP coating is inversely proportional to the phosphorus level. Typical densities of electro and electroless deposits are 8 - 9 g/cc; and 7 - 9 g/cc, respectively [65].

### 2.7.3 Adhesion

Electroless NiP coatings generally have better adhesion than electrodeposits on various metallic substrates, such as iron, nickel, and copper and their alloys. The adhesion of electroless NiP deposits can be additionally increased by heat treatment at 200 °C to 400 °C for 1 hour. Namely, it is required to improve the adhesion of electroless NiP coatings on stainless steel, high carbon steel, chrome steels, and aluminum alloys by annealing or heat treatment [37].

#### 2.7.4 *Hardness and Ductility*

Electroless NiP deposit usually have a hardness value of around 450 - 750 VHN, and upon heat treatment at 350 – 400 °C for 1 hour the hardness can be increased to around 900 - 1000 VHN. However, above 400°C the hardness starts to decrease, and it can be subsequently returned back by cooling [37], [66].

Another factor that affects the hardness of electroless NiP deposit is the phosphorus (P) content. Deposits with higher P level, have lower hardness value. However, the hardness value of electroless NiP deposits can be relatively doubled by undergoing heat treatment above a temperature of 250 °C, due to electroless NiP deposits generally having amorphous structure. However, upon heating, intermetallic compounds are formed depending on the phosphorus content. Accordingly, it can be said that phosphorus content, heat treatment temperature, and time are vital factors affecting the hardness of electroless NiP deposits.

Another important property is the ductility of electroless NiP coatings. Their ductility is mostly less than 2 pct. This value is unfortunately less than the ductility of their analogs formed from the molten state, which have a ductility range of (3 - 30 pct). Actually, this can be disadvantageous, because it is important for any selected metallic materials to have relatively good elastic and plastic properties. There is a quantitative measurement technique that is used to measure ductility called, micromechanical bulge test, which is an improved and preferred measurement method compared to the traditional Ericson technique [37], [42].

#### 2.7.5 *Tensile Strength and Internal Stresses*

Generally, the properties of tensile strength and internal stresses of electroless NiP deposits are highly dependent on the phosphorus content. Tensile strength values

of electroless NiP coatings - in the as-plated conditions - with low phosphorus level are typically between 450 and 550 N/mm<sup>2</sup>. After heat treatment at temperatures ranging between 300 - 600 °C, the tensile strength values decrease to between 200 to 320 N/mm<sup>2</sup>. When steel substrates are coated with electroless NiP coating containing more than 10 wt. % phosphorus, neutral compressive stresses are produced. Whereas, coatings with less phosphorus values develop tensile stresses because of the thermal expansion difference between the substrate and the coating [37], [42].

Cracking and porosity are both promoted at high levels of stresses in NiP coatings. As the microstructure of electroless NiP deposits changes upon annealing/heat treatment at temperatures more than 220°C, this results in volumetric shrinkage of deposits 4-6 wt.% phosphorus. This volumetric shrinkage, in turn, lowers the compressive stresses and rises the tensile stresses [67].

#### *2.7.6 Fatigue Properties*

Using electroless NiP coatings slightly lowers the fatigue strength of steels. Nevertheless, heat treatment of these coatings results in a significant reduction in fatigue strength. There are several factors that affect the magnitude of reduction in fatigue strength, namely, the composition and thickness of electroless NiP coating, and the heat treatment. In addition, the original fatigue strength of the steel is added to the previously mentioned factors. Many studies have reported that using electroless NiP coatings results in the reduction of fatigue strength and endurance limit of steel substrate of about 10 – 50 %. However, electroless NiP deposits from hypophosphite bath might be used for coating high-strength steel with tensile strength larger than 1400 N/mm<sup>2</sup>, without loss of strength. Though, there are some reports suggesting that using electroless NiP coatings causes strength reduction, and few reports show an increase in

strength [68].

#### *2.7.7 Wear and Corrosion Resistance*

Electroless NiP coatings are characterized by their excellent wear resistance, due to their high hardness and good ductility. Actually, the wear resistance of electroless nickel coatings is as good as hard chromium in respect to various environments, and hence can be used as a substitute for hard chromium in several applications. Electroless NiP coatings with phosphorus level of 9 wt.% have shown a taber wear index (TWI) of 17, which is comparable with watts nickel that has a TWI of around 25. The taber wear index is simply defined as weight loss per 1000 revolutions under a loading of 10 N with CS 10 wheels. A previous study have shown that a taber wear index of electroless NiP coating is comparable to hard chromium with TWI values of 9.6 and 0.5-0.7, respectively [42].

Another important property and highly required in oil and gas applications is the corrosion resistance. In electroless NiP coatings, the corrosion resistance properties are highly affected by the composition and the phosphorus content. Most of the investigated electroless NiP deposits have shown naturally passive and corrosion resistive features in various environments. In neutral or acidic environments, alloys having phosphorus content higher than 10 wt.% have shown more resistance to corrosion attack than those of lower P content. On the other hand, alloys with 3-4 wt.% phosphorus (low phosphorus levels) have shown to be more resistant to corrosion in strong alkaline environment compared to electroless NiP deposits with high phosphorus levels [37].

Furthermore, heat treatment of electroless Ni-P deposits at high temperatures above 220 °C, results in the formation of nickel phosphide particles, which in turn

reduces the phosphorus content of the remaining material. Accordingly, this results in reducing the corrosion resistance of the coating. Moreover, active/passive corrosion cells are created by added particles, which further helps in the destruction of the electroless deposits. Annealing these deposits at 190 °C have not caused a significant increase in corrosion resistance. However, hardening caused a high increase in the corrosion rate from 15  $\mu\text{m}/\text{year}$  to more than 900  $\mu\text{m}/\text{year}$ . Generally, it was found that amorphous alloys are more resistive to corrosive environments compared to analogous polycrystalline materials. The main reason is related to their freedom from the formed grain boundaries and glassy films, which passivates their surfaces [37], [42].

## 2.8 Application of Electroless Ni-P Coating in Oil and Gas Industry

Metallic coatings, namely the electroless NiP coatings and their composites are widely used in oil and gas industries as they provide superior anticorrosive properties, high hardness, and wear resistance. Usually corrosion resistance is the primary requirement in prepared coatings for oil and gas applications, followed by wear resistance and hardness.

Generally, electroless NiP coatings are mostly required in applications that need uniform thickness of coating, including some tools and equipment with complex shapes, and large internal surfaces. Also, it is highly required in some process units where surfaces are exposed to wear. Sometimes they can be used for the purpose of replacing costly metallic vessels (e.g. stainless steel vessels), which can be more durable and cost effective.

Additionally, they are applied for repairing some machine parts that are plated with metallic Ni, and to enhance the coating adhesion on steel. Specific tools and equipment that cover large area of application of electroless NiP coatings include the

inner surfaces of valves, pumps, tubes, pipes, gasoline tanks and vessels, storage tanks, screws, etc.

Furthermore, many parts that require improved wear and abrasion resistance under lubricating conditions, including piston cylinders, cylinders for hydraulic pumps, piston rings, rotating shafts, bearing surfaces, motor blades, etc., are usually plated with electroless NiP coatings.

Mostly, electroless NiP coatings with high phosphorus levels has found extensive applications in oil and gas industry, due to the exceptional corrosion resistance and many other enhanced properties. Other than possessing attractive properties, it is considered an inexpensive alternative for other construction materials, such as stainless steel. Actually, nickel cladding or titanium has an extremely high cost as a construction material when used in the assembly of reaction vessels. In comparison, electroless NiP deposit with high P levels, offers a cheaper alternative [41].

## 2.9 Carbon Nitride ( $C_3N_4$ ) Materials and their Application in Corrosion Resistant Coatings

### 2.9.1 *History, Structure, and Unique Properties of Carbon Nitride Materials*

Carbon nitride materials have a relatively long history, which started back in 1830s, when the general formula  $(C_3N_3H)_n$  was reported by Berzelius, and Liebig created the “melon” notation [69], [70]. Then in 1989, Liue and Cohen’s predicted that a super hard material could be obtained from a  $\beta$ -polymorph of hydrogen-free carbon nitride ( $C_3N_4$ ) [71]. In the meantime, scientists and researchers recognized graphitic carbon nitride (g- $C_3N_4$ ) as the most stable allotrope, which triggered great attention for its unique properties. In fact, g- $C_3N_4$  has a similar structure to that of graphite with strong C-N covalent bonds instead of the C-C van der waals bonds in graphite layers. In simple words, g- $C_3N_4$  can be defined as nitrogen-bridged poly (tri-s-triazine), defect-rich substances. Figure (6) shows rings of triazine or tri-s-triazine are crosslinked together by nitrogen atoms assembling extended networks. This represents how graphitic carbon nitride, which is considered the most stable among carbon nitride materials under ambient conditions, can be built up either from the basic blocks triazine ( $C_3N_3$ ), or from tri-s-triazine ( $C_6N_7$ ) units. However, the tri-s-triazine rings are, energetically, more favored and stable than triazine [72].



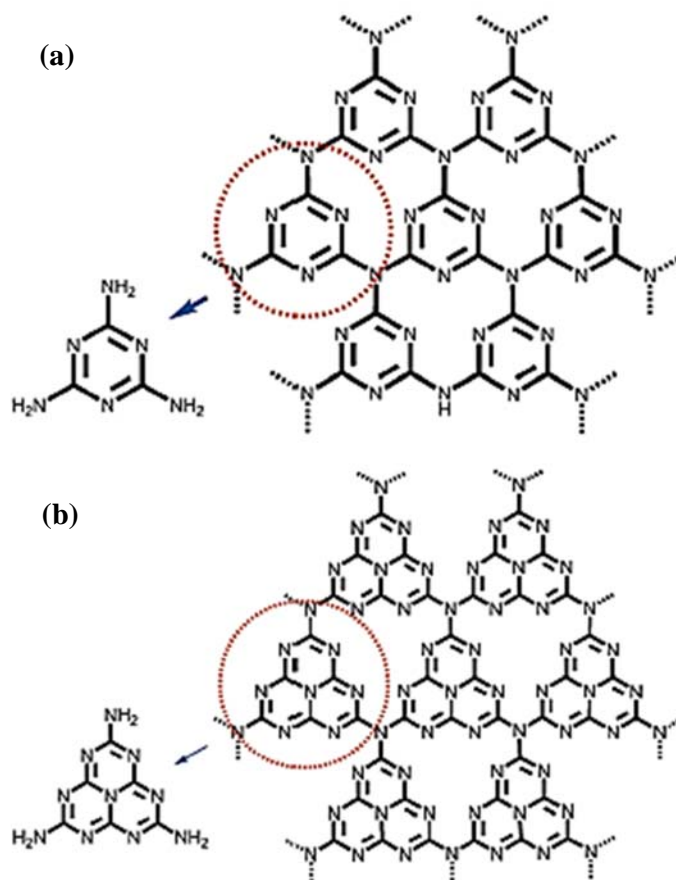


Figure 6. Triazine (a) and tri-s-triazine (b) crosslinked structures. Adapted from ref. [72]

It is important to mention that there are so many different classes of carbon nitride materials, shown in Figure (7), depending on the physical or chemical routes that were used to produce them. Actually, most of the synthesized carbon nitride materials, up to date, contain considerable quantities of hydrogen (H) as an essential component in their structures, in addition to carbon (C) and nitrogen (N). These materials can be denoted as “C<sub>x</sub>N<sub>y</sub>H<sub>z</sub>” compounds. However, as mentioned earlier, graphitic carbon nitride (g-C<sub>3</sub>N<sub>4</sub>) compounds are those that have structures based on triazine (C<sub>3</sub>N<sub>3</sub>) rings, or tri-s-triazine blocks (heptazine, C<sub>6</sub>N<sub>7</sub>) [11], [73].

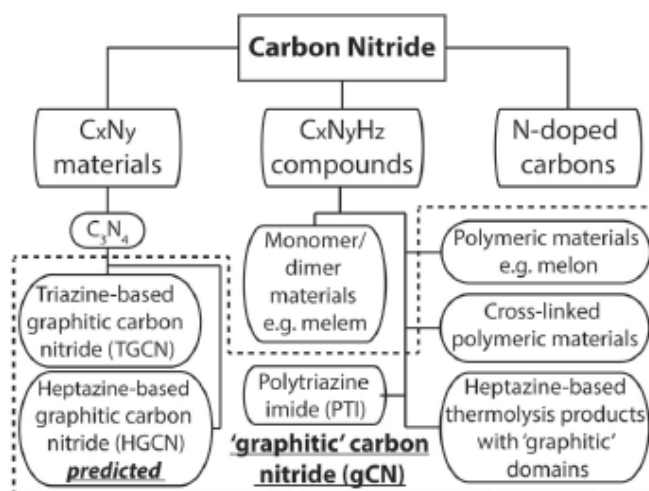


Figure 7. Schematic diagram of classified carbon nitride materials. Materials that are often named as graphitic carbon nitride (g-C<sub>3</sub>N<sub>4</sub>) are indicated in the dashed box, extracted from ref. [11].

The unique structure of tri-s-triazine ring with high-condensed degree gives high chemical and thermal stability for the polymer, i.e. these compounds are stable at temperatures up to 600°C in air, and chemically stable under, basic, acidic, and organic solvents. Moreover, they possess a distinctive electronic structure, having a medium bandgap, and featured as an indirect semiconductor. These important features allow them to be utilized in multifunctional applications, such as catalysts, fuel cells, biomedical applications, and corrosion resistant coatings, etc. [74]

Generally, graphitic carbon nitride (g-C<sub>3</sub>N<sub>4</sub>) have various advantages when compared to other carbon nanostructures. Most importantly, they possess a facile preparation method, simple composition, lower cost, high chemical, mechanical, and thermal stability, and distinctive catalytic behavior [75].

### 2.9.2 *Preparation Methods and Various Shapes of Triazine-Based Graphitic Carbon Nitride Structures*

Graphitic carbon nitride can be prepared using common methods like chemical vapor deposition (CVD), physical vapor deposition (PVD), single-step nitridation, thermal condensation, and solvothermal method. However, the most commonly used method is thermal condensation, for its simplicity and low cost, where precursors, such as cyanamide, urea, dicyanamide, etc. are thermally condensed. Subsequently, either chemical, thermal oxidation, or ultrasonic exfoliation method can be applied to obtain a single layer of g-C<sub>3</sub>N<sub>4</sub> [76]. Nevertheless, the chemical exfoliation approach is considered the best among other methods, as it provides the highest efficiency, with a relatively low cost [77]–[80].

The rising demands of new materials in various applications, namely in energy, sustainability, and biomedical fields have recently encouraged intensive research to improve new generations of g-C<sub>3</sub>N<sub>4</sub> materials with diverse shapes and morphologies. Researchers succeeded to develop new synthesis methods, which resulted in novel micro and nanostructures of g-C<sub>3</sub>N<sub>4</sub>, e.g. amorphous or bulky, thin films, nanosheets, mesoporous, 1-dimensional shapes such as nanorods, nanowires, and nanotubes, and 0-dimensional quantum dots. Examples of produced g-C<sub>3</sub>N<sub>4</sub> shapes are presented in Figure (8).

In fact, many factors affect the final shape and morphology of produced g-C<sub>3</sub>N<sub>4</sub> materials, which are being rapidly improved. These factors include the preparation methods, process conditions such as condensation temperature, and materials composition. This indeed reflects on the attained properties and functionality of the prepared g-C<sub>3</sub>N<sub>4</sub> materials, which in turn expand their applications [72].

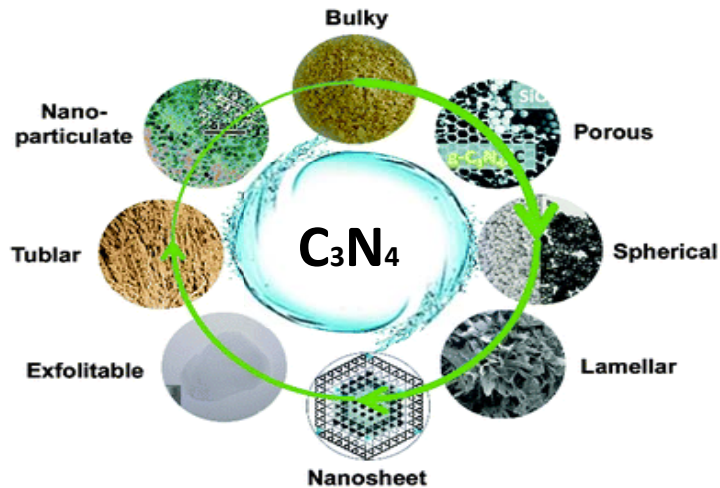


Figure 8. Various shapes and morphologies of g-C<sub>3</sub>N<sub>4</sub> materials. Retrieved from ref. [72]

### 2.9.3 Carbon Nitride in Polymer-based Coatings

Polymer based coatings are widely used in industry and various applications for its effective anticorrosive and barrier properties. However, some kinds of polymer coatings, such as epoxy, suffer from microporous defects that appear during the curing process, which allow for the diffusion of electrolyte into the substrate. Consequently, this leads to the emergence of adhesion loss in a very short time, hence reduce the barrier properties of the coating [81]–[83]. Recently, the incorporation of g-C<sub>3</sub>N<sub>4</sub> nanoparticles into polymer matrix to prepare a polymer nanocomposite has demonstrated great enhancement in anticorrosive properties of various polymer coatings.

Yan et al. [84] synthesized g-C<sub>3</sub>N<sub>4</sub> nanosheets, and applied them as a nanofiller in the fabrication of g-C<sub>3</sub>N<sub>4</sub>/epoxy nanocomposite coatings. Several epoxy-based nanocomposites were prepared with different concentrations (1.00, 1.50, 2.00, 2.50, and 3.00 wt. %) of g-C<sub>3</sub>N<sub>4</sub> nanosheets and used as a coating for Q235 steel substrate. The

corrosion resistance study in 3.5% NaCl and 0.1 M H<sub>2</sub>SO<sub>4</sub> electrolyte solutions generally showed great enhancement of corrosion resistance behavior of g-C<sub>3</sub>N<sub>4</sub>/epoxy nanocomposite coatings compared to pure epoxy in both previously mentioned corrosive electrolytes, as shown in Figure (9).

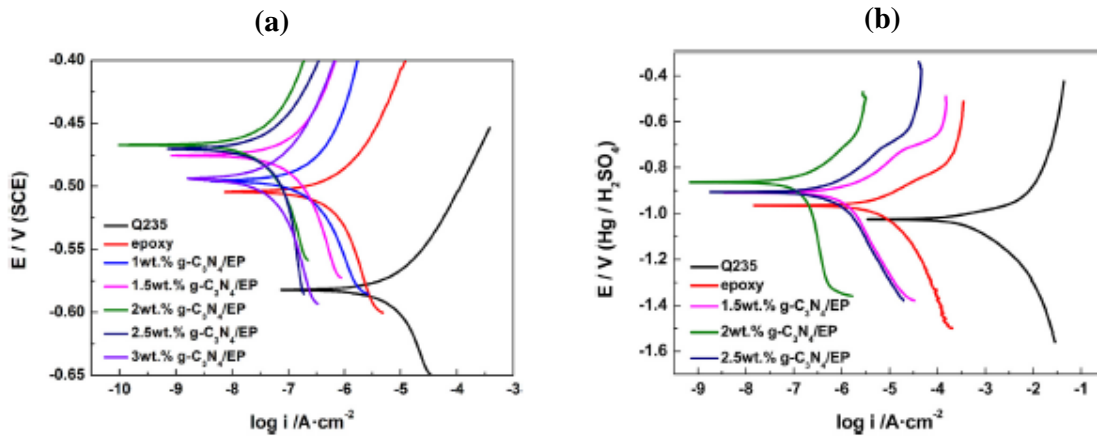


Figure 9. Potentiodynamic polarization curves of Q235 steel, pure epoxy, and g-C<sub>3</sub>N<sub>4</sub>/epoxy nanocomposite samples at different concentrations of C<sub>3</sub>N<sub>4</sub> nanosheets after 1 h immersion in (a) 3.5% NaCl and (b) 0.1 M H<sub>2</sub>SO<sub>4</sub> solution. Ref. [84]

Moreover, it was found that the 2 wt. % of g-C<sub>3</sub>N<sub>4</sub> nanosheets, which was uniformly dispersed in the epoxy matrix showed the highest anticorrosion behavior of epoxy coating. Furthermore, the results revealed that the g-C<sub>3</sub>N<sub>4</sub> nanosheets positively interacted with the epoxy matrix, which enhanced the coating's adhesion on steel substrate [84], as indicated in Figure (10).

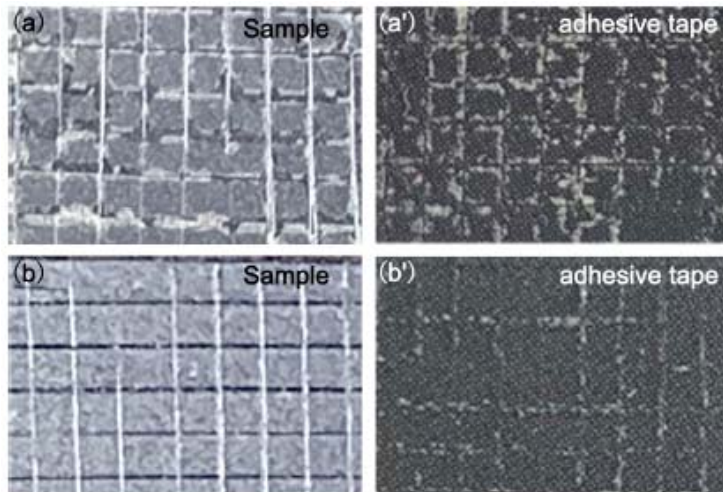


Figure 10. Photos of (a, a') epoxy coating, and (b, b') g-C<sub>3</sub>N<sub>4</sub>/epoxy nanocomposite coating containing 2 wt. % g-C<sub>3</sub>N<sub>4</sub> nanosheets, before and after adhesion test, respectively. Extracted from ref. [84]

On the other hand, ZuO et al. [79] used the chemical oxidative polymerization method to synthesize polyaniline/g-C<sub>3</sub>N<sub>4</sub> composite coating, which resulted in superior anti-corrosive coating with enhanced barrier behavior compared to pure counterparts. The best corrosion protection was obtained by the polyaniline/g-C<sub>3</sub>N<sub>4</sub> composite coating with a mass ratio of 3:1, which could be accredited to the mutualistic anticorrosion effect between polyaniline and g-C<sub>3</sub>N<sub>4</sub>.

Kumar et al. [85] modified the surface of g-C<sub>3</sub>N<sub>4</sub> by using MoO<sub>x</sub>, which promoted a uniform dispersion in epoxy coatings. Their outcomes indicated that the best corrosion resistance was obtained when 3 wt.% of g-C<sub>3</sub>N<sub>4</sub>/MoO<sub>x</sub> nanoparticles were added to epoxy. This result was attained without affecting the coating's adhesion strength on aluminum substrates. They concluded that the high corrosion resistance mainly raised from filling the coating porosities by g-C<sub>3</sub>N<sub>4</sub> nanoparticles, which improved the resistance against electrolyte permeation, and coatings degradation.

Another investigation conducted by Kumar et al. [18] showed great improvement in the corrosion protection performance of pure epoxy coating on carbon steel in NaCl solution. Their study addressed synthesizing ZnO/g-C<sub>3</sub>N<sub>4</sub> nanosheets and applying them as nanofillers in pure epoxy to enhance its corrosion resistance. Their outcomes indicated that the use of ZnO/g-C<sub>3</sub>N<sub>4</sub> nanosheets acted as a barrier for water absorption and enhanced the surface protective characteristics; hence, the corrosion resistance performance of pure epoxy has improved, as clarified in Figure (11).

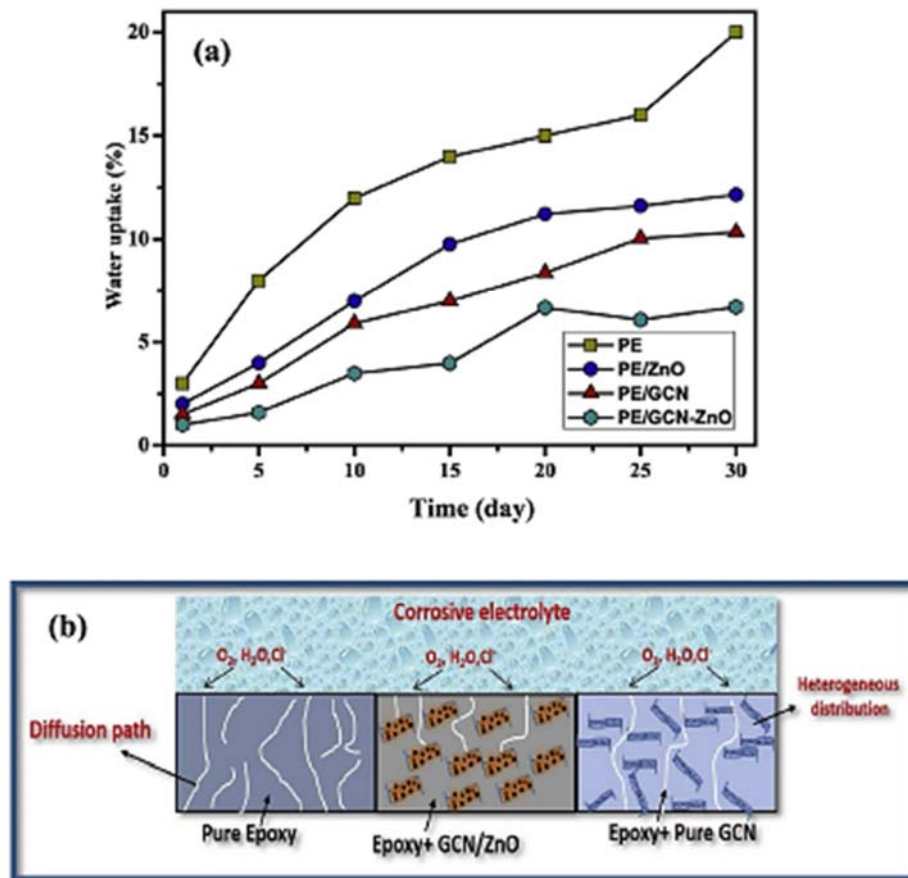


Figure 11. (a) Plots of water uptake in epoxy coatings as a function of immersion time, (b) Schematic demonstration of reduced water absorption by epoxy coating upon the addition of nanofiller, adapted from ref. [18].

Moreover, Xu et al. [86] prepared a smart anticorrosive nanocomposite coating to protect Al alloys. They used g-C<sub>3</sub>N<sub>4</sub> as a nanofiller in poly (urea-urethane) matrix. Through their investigation they found that, even under high humidity conditions, the poly (urea-urethane)-g-C<sub>3</sub>N<sub>4</sub> composite coating showed outstanding barrier performance and self-healing ability.

Furthermore, Xia et al. [87] worked on enhancing the dispersion of g-C<sub>3</sub>N<sub>4</sub> (GCN) nanosheets in waterborne epoxy coating through the co-modification of GCN nanosheets by dopamine and silane coupling agent. The results of electrochemical corrosion and salt spray tests revealed that the modified GCN nanosheets are promising nanofillers that significantly improve the anticorrosion performance of waterborne coatings.

#### *2.9.4 Carbon Nitride Corrosion Resistant Thin films*

In certain applications, such as biomedical implants, it is of great importance to develop biocompatible materials with enhanced mechanical, wear, and corrosion resistance properties. Thin films of amorphous carbon nitride material are considered as promising coatings that promote the performance of standard medical metal alloys, e.g. CoCrMo and Ti<sub>6</sub>Al<sub>4</sub>V. They proved to be chemically inert with a biocompatible nature that suppress the harmful and undesirable biological reactions [88].

Marton et al. [89] used vacuum glow discharge sputtering technique to deposit nitrogen doped amorphous carbon (a-C:N) films on silicon and medical CoCrMo alloy substrates. In their research, they investigated the effect of using different deposition conditions, i.e. varying substrate bias, on the electrochemical corrosion behavior for Si and CoCrMo substrates in 0.89 wt. % NaCl solution. The main outcomes of their study indicated that, generally, the coated samples with amorphous carbon nitride thin films



are more resistant to corrosion than uncoated samples. Moreover, the coating deposited with substrate bias around  $-0.6$  kV gave the highest  $E_{\text{corr}}$  for CoCrMo alloy. Results obtained from polarization tests are presented in Figure (12).

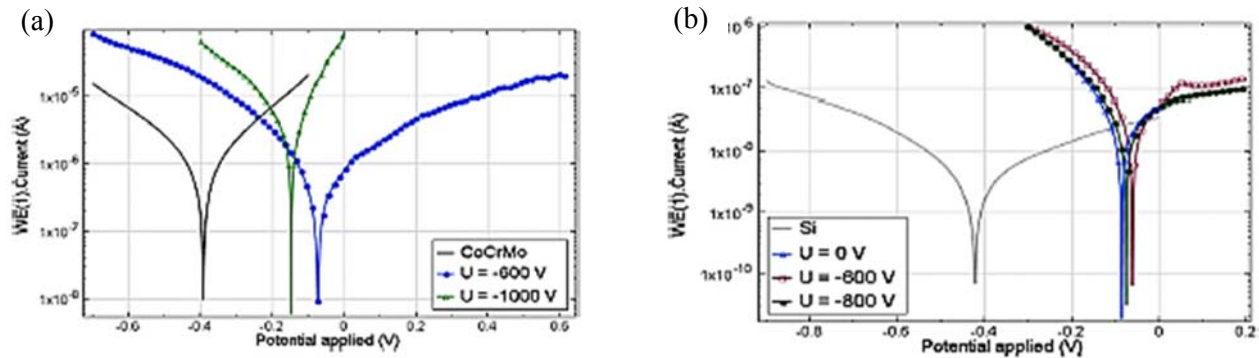


Figure 12. Tafel curves for uncoated and a-C:N coated (a) CoCrMo and (b) Silicon substrates deposited with various substrate bias [89].

### 2.9.5 Carbon Nitride Corrosion Resistant Multilayered systems

Numerous researchers have been studying the development of single layered systems, such as TiCN, AlCN, etc., as well as, multilayered structures, or superlattices to investigate their use as hard and protective coatings. The demand of multilayered structures is mainly due to their enhanced mechanical and tribological performance [90], [91].

Examples of multilayered systems that triggered major attention due to their high hardness include ceramic/ceramic and metal/ceramic structures with nanometer thickness. It is worth mentioning that these combinations often produce high hardness values while retaining relatively ductile and highly anticorrosive coatings [92].

Various research works studied the anticorrosive behavior of nitride coatings made of single and multilayers. Generally, it was found that multilayered nitride

coatings show higher corrosion resistance compared to single layer under corrosive environment. This is due to the enhanced interface number and microstructural features in multilayered systems, which is supported by previous works showing that nitride coatings usually initiate corrosive failures at structural defects, such as microcracks and pores. Additionally, other works demonstrated that nitride single layer coatings possess up to 5% porosity level, which varies from the porosity of multilayer nitride coatings that decreases to 1%, which indeed reflects on their anticorrosive performance [93].

Caiced et. al. [90] deposited multilayered coatings of  $[\text{TiCN}/\text{TiNbCN}]_n$  using r.f. magnetron sputtering method. They investigated the effect of changing the deposition parameters, i.e bilayer periods ( $\Lambda$ ) and bilayer number ( $n$ ), on the anticorrosion performance of the coatings. The results confirmed the deposition of distinct multilayered structures, which showed the best anticorrosion behavior for the coating with a bilayer period ( $\Lambda$ ) = 15 nm and bilayer number ( $n$ ) = 200. The authors suggested that the improved corrosion resistance in multilayer coating with  $\Lambda$  = 15 nm, and  $n$  = 200 may be attributed to the unique microstructure of the deposited multilayer coating, i.e. free porosity obtained by their distinctive orientation, and interfaces.

#### *2.9.6 Carbon Nitride in Metallic based coatings*

Metallic coatings, in general, triggered great attention in oil and gas industries due to their superior mechanical and corrosion resistance properties. As mentioned earlier, electroless plating technique used in the deposition of metallic coatings is very advantageous, mainly because it provides a uniformly deposited coating, even for objects with sophisticated geometries such as valves, pumps, nuts, etc. [42], [94]–[96]. Numerous research have been conducted on various types of metallic coatings for the improvement of their overall performance, namely, the electroless plated NiP coatings,

which are widely used in various industries [95], [97]–[99].

Few research works reported the use of carbon nitride materials in electroless NiP metallic coating as a nanofiller, which in fact resulted in great enhancement of its overall performance, namely the mechanical and corrosion resistance properties.

Fayyad et al. [10] successfully fabricated NiP-C<sub>3</sub>N<sub>4</sub> nanocomposite coating to protect C-steel substrate through dispersing C<sub>3</sub>N<sub>4</sub> nanosheets in the electroless NiP bath. The authors investigated and reported the best electroless deposition conditions that provide the best overall properties of the prepared NiP-C<sub>3</sub>N<sub>4</sub> nanocomposite coating. Moreover, they studied the effect of heat treatment on the coating's mechanical and anticorrosive behavior. Their results showed that the presence of the C<sub>3</sub>N<sub>4</sub> nanosheets, which were uniformly dispersed within the NiP matrix, lead to approximately 50 % improvement in the microhardness of the NiP coating. Furthermore, the corrosion tests in 3.5% NaCl solution, including EIS measurements, indicated a higher corrosion resistance of as-plated NiP-C<sub>3</sub>N<sub>4</sub> nanocomposite coatings, showing a 95% protection efficiency, compared to pure NiP coating that shows only 81% protection efficiency. The results after heat treatment, presented a great enhancement in the microhardness, clarified in Figure (13), and a slight decrease in the corrosion resistance of the composite coatings, due to the formation of a new crystalline Ni<sub>3</sub>P phase. However, the corrosion measurements still showed higher resistance than that of pure NiP coating. The corrosion resistance results are presented in Figure (14), where a larger |Z| value at low frequency represents a better anticorrosive property of the coating.

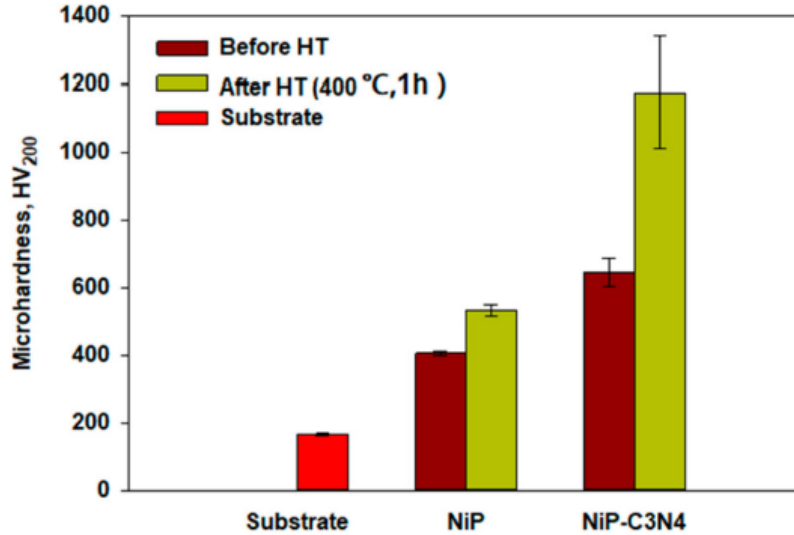


Figure 13. Microhardness of as plated and heat treated electroless NiP and NiP-C<sub>3</sub>N<sub>4</sub> composite coatings in comparison to bare C-steel substrate [10].

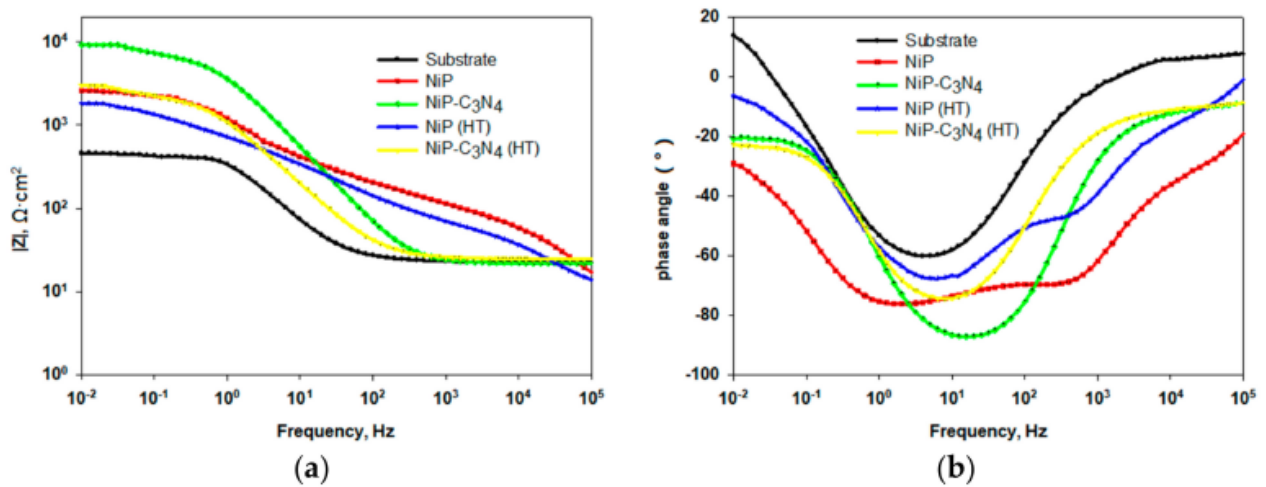


Figure 14. Bode and phase angle plots (a, b) for C-steel substrate, as plated and heat treated electroless NiP, and NiP-C<sub>3</sub>N<sub>4</sub> nanocomposite coating [10].

In summary, graphitic carbon nitride materials, have many attractive features, namely facile synthesis, low cost, and unique structure, which make them broadly utilized in various applications. However, research works mainly focused on graphitic

carbon nitride for photocatalytic applications, biomedical applications, fuel cells, and polymer-based anticorrosive coatings. Very few reports investigated the insertion of carbon nitride materials to enhance the corrosion resistance properties of metallic coatings. The synthesis of NiP-C<sub>3</sub>N<sub>4</sub> nanocomposite coating using C<sub>3</sub>N<sub>4</sub> nanosheets has been reported, and shown excellent results in terms of enhancing the overall performance compared to pure NiP coatings. However, to the best of our knowledge, the effect of changing the shape, morphologies and nature of C<sub>3</sub>N<sub>4</sub> nanomaterial on the mechanical and corrosion resistance properties of electroless NiP-based coating have never been addressed before. In the present work, we intend to close part of this gap and investigate the effect of using newly synthesized ZnO/C<sub>3</sub>N<sub>4</sub> nanocapsules, on the overall performance of NiP-C<sub>3</sub>N<sub>4</sub> nanocomposite coatings.

## CHAPTER 3: MATERIALS AND METHODOLOGY

### 3.1 Materials

Table 2. Summary of used materials

<b>Material</b>	<b>Required Specifications</b>	<b>Purpose</b>
API X120 C-steel	Grinded, polished, and pretreated Size: 20 × 20 × 10 mm <sup>3</sup>	Used as a substrate
Acetone	Ultrasonicated – analytical grade	Used for degreasing the specimens.
NaOH, Na <sub>3</sub> PO <sub>4</sub> , and Na <sub>2</sub> CO <sub>3</sub>	A mixture of 50 g/L NaOH, 30 g/L Na <sub>3</sub> PO <sub>4</sub> , and 30 g/L Na <sub>2</sub> CO <sub>3</sub> (analytical grade solutions)	Used for specimens alkaline cleaning step.
Acidic H <sub>2</sub> SO <sub>4</sub> Solution	15 wt. % H <sub>2</sub> SO <sub>4</sub>	Used for etching the C-steel specimens as a pretreatment step.
Deionized water	Ultrapure	Deionized water was used to wash the specimens after each pretreatment step.
Nichem 3010 electroless solution, from Atotech Inc., Berlin, Germany	Standard commercial electroless NiP deposition solution	Electroless nanocomposite coating bath
Carbon nitride (C <sub>3</sub> N <sub>4</sub> ) nanocapsules	Synthesized and characterized ZnO/C <sub>3</sub> N <sub>4</sub> nanocapsules	Raw material used in the electroless plating bath for the synthesis of nanocomposite coating
Sodium chloride (NaCl)	Analytical grade	Used to prepare 3.5 wt.% NaCl used for corrosion tests

### 3.2 Preparation of C<sub>3</sub>N<sub>4</sub> Nanocapsules with and without ZnO as a Dopant

Sodium hydroxide (NaOH), functionalized mesoporous silica (SBA-15 silica), acid (HF), 3-Aminopropyl trimethoxysilane (APTMS), and zinc oxide 50 nm were delivered from Sigma Aldrich Co., Ltd., and ammonia solution (25 wt % NH<sub>4</sub>OH in water), formaldehyde, ethanol, resorcinol, and melamine were purchased from VWR Chemical Industries Ltd.

ZnO-doped and undoped C<sub>3</sub>N<sub>4</sub> nanocapsules were prepared using silica-based template. This includes dissolving SB-15 nanoparticles (1 g) in an aqueous solution of ethanol (100 mL) containing ZnO nanoparticles (with different amounts). The loading amount of ZnO was changed to 0, 0.5, 1.0, and 2 g, for preparing C<sub>3</sub>N<sub>4</sub>, C<sub>3</sub>N<sub>4</sub>/0.5 ZnO, C<sub>3</sub>N<sub>4</sub>/1.0g ZnO, and C<sub>3</sub>N<sub>4</sub>/2.0g ZnO, respectively. The solution was stirred at room temperature for 1 h followed by the addition of NH<sub>4</sub>OH (6.5 mL of 25 Wt. %). APTMS (1 mL) solution was added to the previous solution under refluxing for 6 h at 90 °C under magnetic stirring, and then the solution was centrifuged at 800 rpm and washed 3 times by double deionized water to form APTMS@SBA-15 nanoparticles. The formed nanoparticles in (g/mL) were dispersed in ethanol solution under stirring at room temperature, then mixed with an aqueous solution that contains 0.1 mol resorcinol, 0.05 melamine, and 3 mL formaldehyde under stirring at 30 °C room temperature for 1 h, then the temperature was raised to 80 °C, while refluxing for another 24 h.

The obtained precipitate was purified by interval 3 centrifugation cycles at 9000 rpm and 3 washing cycles by ethanol and water (3/1 v/v), then dried at 80 °C for 4 h before being annealed at 750°C for 2 h under nitrogen (N<sub>2</sub>). After cooling to the room temperature, the obtained powder was immersed in NaOH solution for 24 h to etch SBA-15 solution and then washed 3 times by water then dried at 80°C to form the C<sub>3</sub>N<sub>4</sub>

nanocapsules (undoped, and doped with different amounts of ZnO, i.e. 0.5, 1.0, and 2.0g), and kept for any additional use or characterization.

### 3.3 Pretreatment of Specimens

API-X120 C-steel was used as a substrate for the electroless deposition process, as it is a widely used metal in oil and gas industry. The C-steel bar, with a wt. % composition shown in Table (3) below, was cut into  $20 \times 20 \times 10$  mm<sup>3</sup> specimens and pretreated (mechanically and chemically) before the electroless deposition.

Table 3. Weight % composition of API-X120 C-Steel

C	Mn	V	Si	Cr	Cu	Ni	Mo	Fe
0.129	0.541	0.025	0.101	0.039	0.015	0.017	0.0013	balance

The pretreatment process included grinding with various emery papers up to 2000 grit, and polishing until a mirror-finishing surface was obtained. Other pretreatment steps were also required for the specimens, which included chemical degreasing with acetone for 15 minutes, followed by alkaline cleaning for 5 minutes at 80 °C. The alkaline cleaning solution consists of 50 g/L NaOH, 30 g/L Na<sub>3</sub>PO<sub>4</sub>, and 30 g/L Na<sub>2</sub>CO<sub>3</sub>. Subsequently, the specimens were etched in acidic solution of 15 wt. % H<sub>2</sub>SO<sub>4</sub> for 20 seconds, Figure (15) summarized the different pretreatment steps. After each pretreatment step, the specimens were thoroughly washed with ultrapure deionized water to remove any contaminants. Finally, after pretreatment steps, the specimens were ready for electroless deposition step. Solutions of analytical-grade purchased from Sigma-Aldrich (St. Louis, MO, USA) were used for all the experimental preparations.



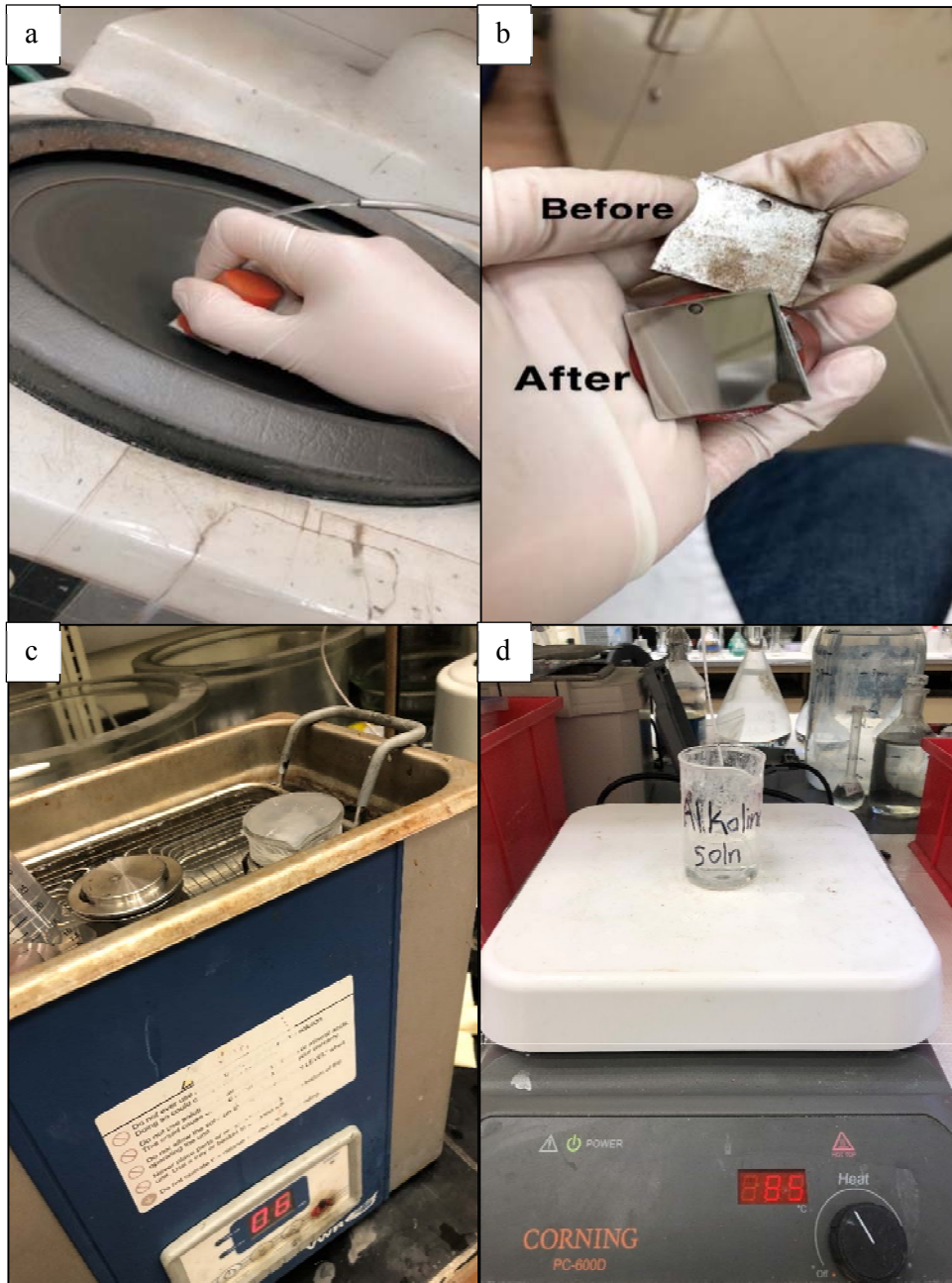


Figure 15. Pretreatment steps for C-steel specimens: (a,b) grinding and polishing, (c) acetone sonication, and (d) alkaline cleaning.

### 3.4 Electroless Deposition

A commercial electroless nickel phosphorus plating solution (Nichem 3010), purchased from Atotech Deutschland GmbH (Berlin, Germany) was used for the different electroless deposition. A concentration of 0.5 g/L  $C_3N_4$  was kept constant for the various prepared electroless NiP- $C_3N_4$  baths. The synthesized  $C_3N_4$  nanocapsules, undoped and doped with different concentrations of ZnO, i.e. 0.50, 1.00, and 2.00 g of ZnO, were separately ultrasonicated for 2 hours in the electroless NiP solution before deposition. This step was essential to ensure well dispersed nanomaterial in the bath and avoid any agglomeration. The composition and operating conditions of NiP- $C_3N_4$  baths during the electroless deposition process are summarized in Table (4) below.

Table 4. Operational parameters and bath constituents of electroless plating process

Bath constituent		Operating parameters	
Electroless NiP solution (L)	1	Plating Temperature ( $^{\circ}C$ )	$89 \pm 1^{\circ}C$
Amount of $C_3N_4$ (g)	0.5	Stirring (rpm)	300
Amount of ZnO doped in $C_3N_4$ (g)	0.50, 1.00, and 2.00 g	Plating time (h)	2
---	---	pH	$4.5 \pm 0.1$

After preparing the electroless baths, the pretreated specimens of API-X120 C-steel were instantly immersed in each bath, the electroless coating process was allowed for 2 hours. Finally, the coated specimens were removed from the bath, washed with deionized water, and dried using blowing air. Figure (16) showed the electroless plating bath and the coated specimen with the NiP-  $C_3N_4$ /ZnO nanocomposite coating.

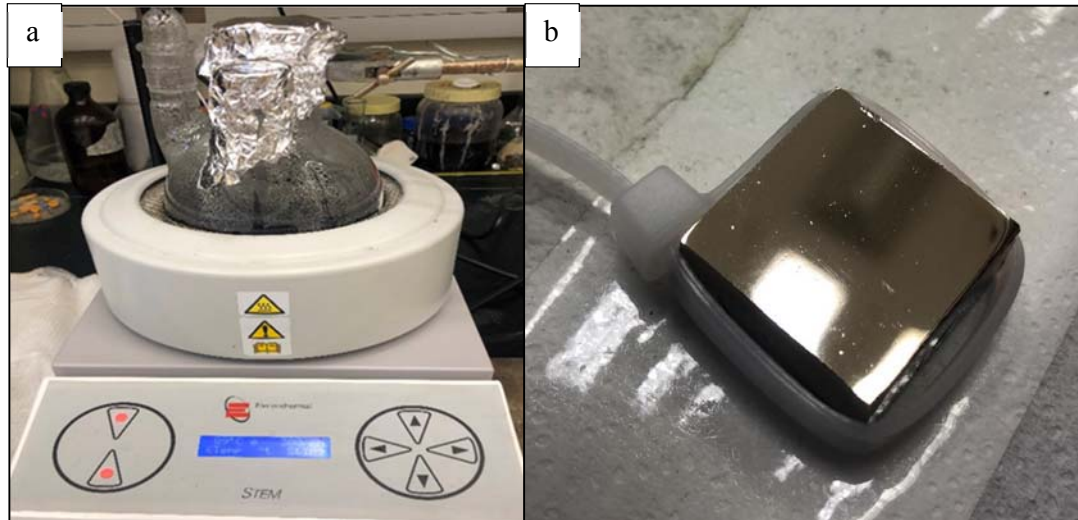


Figure 16. (a) Electroless plating bath and (b) C-steel specimen coated with NiP- C<sub>3</sub>N<sub>4</sub>/ZnO composite coating.

### 3.5 Heat Treatment

After the electroless deposition process, some samples of the various produced nanocomposite coatings were annealed at 400 °C for 1 h using vacuum tube furnace, from MTI (California, USA), which is shown in Figure (17). This step was essential to investigate the mechanical properties and corrosion resistance of the coatings after heat treatment.



Figure 17. MTI Tube furnace used for heat treatment of deposited specimens.

### 3.6 Characterization

The crystal structure, surface morphology and elemental composition, roughness, hydrophobicity, mechanical, and anticorrosive properties of the different prepared coatings, were investigated before and after heat treatment, using various characterization techniques. .

#### 3.6.1 Structural analysis (XRD)

The effectiveness of the undoped  $C_3N_4$  capsules in addition to changing ZnO dopant concentrations, on the crystal structure and phases of electroless NiP and NiP- $C_3N_4$  nanocomposite coatings, respectively, was analyzed using X-ray diffractometer (XRD, Miniflex2 Desktop, Cu K, Rigaku, Tokyo, Japan).

X-ray diffraction (XRD) is a nondestructive characterization technique used to study the structure of materials. It mainly finds out whether the material follows crystalline or amorphous nature. XRD analysis uses Cu/K x-ray source, a radiation ( $\lambda$ ) equals to 1.5406 Å, and it analyzes and detects the unknown elements and compounds using Bragg's law. Furthermore, XRD provides other important information about phases, crystal defects and strain. There are specific parameters that should be identified depending on the requirements for the tested sample. These include voltage and current of x-ray tube, collection time, scan step size, and range. As the test is started, the reflected X-rays from the adjacent crystal planes undergo constructive interference. Accordingly, the path distinction among them is an integer multiple (n) of the wavelength of the X-rays (Bragg's law). The "order" of a reflection wavelength of the X-ray is n, whereas d is the interplanar spacing of the crystal between adjacent crystal planes,  $\lambda$  is the wavelength of the incident X-rays, and theta ( $\theta$ ) is the angle between the scattering plane and incident X-ray beams [100], as clarified in Figure (18).

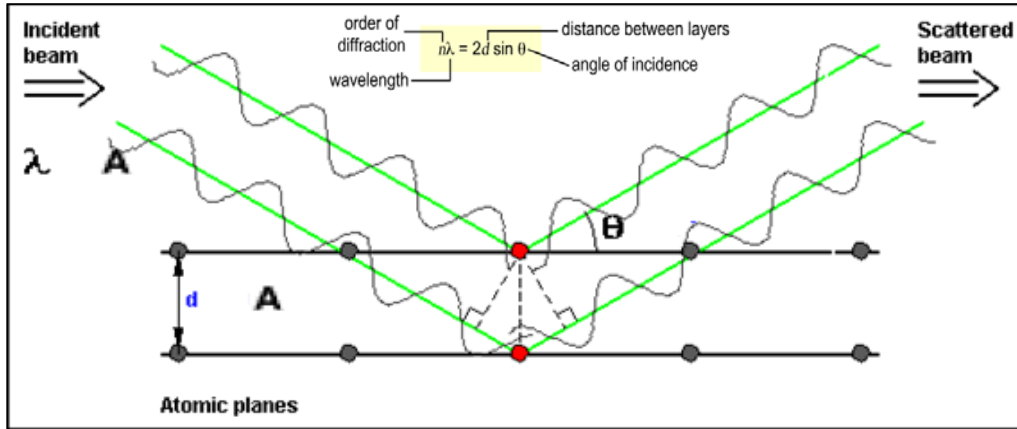


Figure 18. Schematic of X-ray diffraction in solid crystals as stated by Bragg's law for constructive interference [96].

### 3.6.2 Surface Morphology and Compositional Analysis

Scanning electron microscope (SEM, Nova NanoSEM 450, ThermoFischer Scientific, Eindhoven, Netherland) was used to assess the surface morphology and the coating thickness of each sample, and energy-dispersive spectroscopy (EDX, Bruker detector 127 eV, Bruker, Leiderdorp, Netherlands) was utilized for achieving the elemental analysis of the prepared coatings.

Scanning electron microscope (SEM) is a powerful microscope that uses an electron beam, which hits and scans the surface of the targeted sample inside a vacuum chamber, hence produces an image that shows the morphology. As presented in Figure (19), in the top of the chamber there exists a metallic filament that is heated to produce the electron beam. Then, the beam of electrons pass vertically through the microscope's column, which is provided with electromagnetic lenses that direct and focus the electron beam down towards the tested specimen. Once the beam reaches the sample's surface and hits it, backscattered and/or secondary will be emitted. Finally, these emitted electrons (backscattered or secondary) are collected by detectors, which are then

transformed into signals that are viewed on a computer screen as an image [101], [102].

Figure (20) is the SEM and EDX device that was utilized in the central lab units in Qatar University.

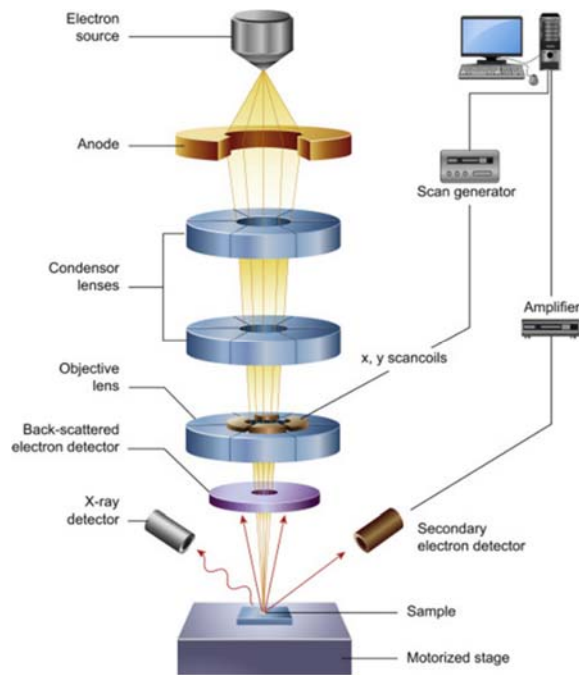


Figure 19. Scanning electron microscope (SEM), a schematic showing main components. [98]



Figure 20. SEM and EDX device that was utilized in the central lab units, Qatar University

In addition, a high resolution transmission electron microscope (HR-TEM, JEOL 2100 F, Japan) was used to analyze the  $C_3N_4$  nanocapsules in the electroless NiP- $C_3N_4$ /ZnO deposits.

TEM is a powerful instrument, similar to SEM, used for characterizing the materials morphology, composition, and imaging. However, TEM technique can be used for very thin samples only, and it uses higher voltage, which provides images with higher magnification and resolution than SEM. Moreover, this technique offers deeper information about the internal structure and composition, as the electron beam can penetrate through the tested sample [103].

In order to get an image, the microscope was operated at 200 kV. The sample preparation was conducted by scratching the surface of coated specimens with various NiP-ZnO/ $C_3N_4$  deposits, followed by rinsing with ethanol. A small quantity of scratched deposit was dispersed in ethanol, and then placed on a copper TEM grid using a syringe. Ethanol solution was allowed to dry under red light, and then the copper grid containing the scratched sample was positioned under the electron beam produced by the electron gun. Figure (21) presents the HRTEM device used in the central lab units in Qatar University for morphological imaging.



Figure 21. HRTEM device used for morphological imaging

### 3.6.3 *Surface roughness*

Measurement of the surface roughness of the synthesized coatings was achieved using an atomic force microscopy (AFM). In fact, AFM is a very effective technique for examining specimens at nanoscale. Additionally, this technique can perform numerous essential surface measurements for different kinds of samples, with simple preparations requirements. It can produce images at the nano scale with 3D features, even for samples with complicated shapes and very rough topographies [104]. Figure (22) pictures the asylum research atomic force microscope, MFP3D, that used in center for advanced materials in Qatar University.

AFM test for the synthesized coatings was performed by operating MFP3D Asylum research atomic force microscope (Asylum Research, Santa Barbara, CA, USA), which was equipped with a silicon probe. The roughness experiments were conducted under a spring constant of  $2 \text{ Nm}^{-1}$ , a resonant frequency of 70 kHz, and the device was run under ambient conditions using the tapping mode in air.



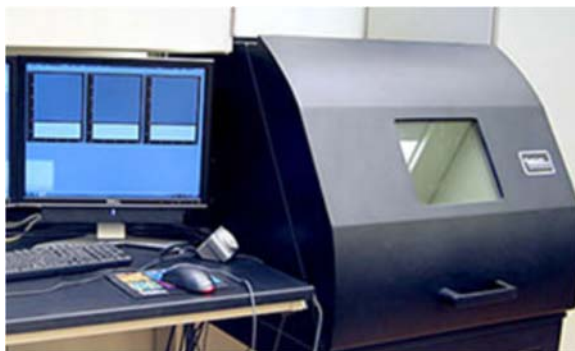


Figure 22. Asylum research atomic force microscope, MFP3D

#### 3.6.4 *Water Contact Angle (WCA)*

The water contact angle (WCA) measurements for the as-plated and heat-treated specimens were performed to identify the level of hydrophobicity and/or hydrophilicity of prepared coatings. This technique was achieved by utilizing a contact angle device (DataPhysics OCA35, DataPhysics Instruments GmbH, Filderstadt, Germany). The used probing liquid was deionized water (4  $\mu\text{L}$ ), and for achieving precise measurements, the contact angle was measured 5 times, where the average value is reported.

Determining the wettability of prepared coatings is very important, which can be indicated through the contact angle parameter. The use of so-called sessile drop method is mostly used for analyzing the contact angle, where the tangent angle is directly measured at three-phase equilibrium interfacial point. However, the wetting property for flat surfaces is directly measured by observing the profile of the water drop. Figure (23) shows the way water molecules interact with different surfaces, i.e. hydrophobic and hydrophilic substrates. In order to trace the outlines, the adhering bubble can be imaged and projected on a screen, hence the angle can be easily measured [105].

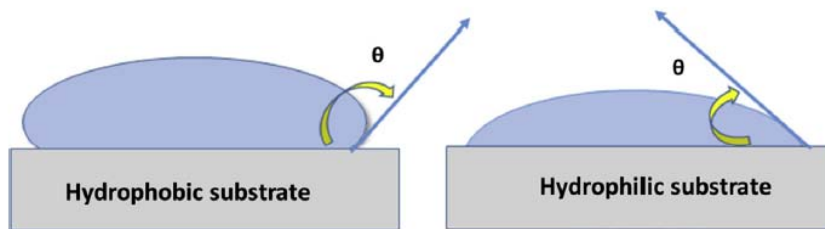


Figure 23. Interaction of water molecules with hydrophobic and hydrophilic surfaces.

It is worth mentioning that using relatively high magnifications provide better accuracy of the method. Figure (24) clarifies the idea of sessile drop technique.

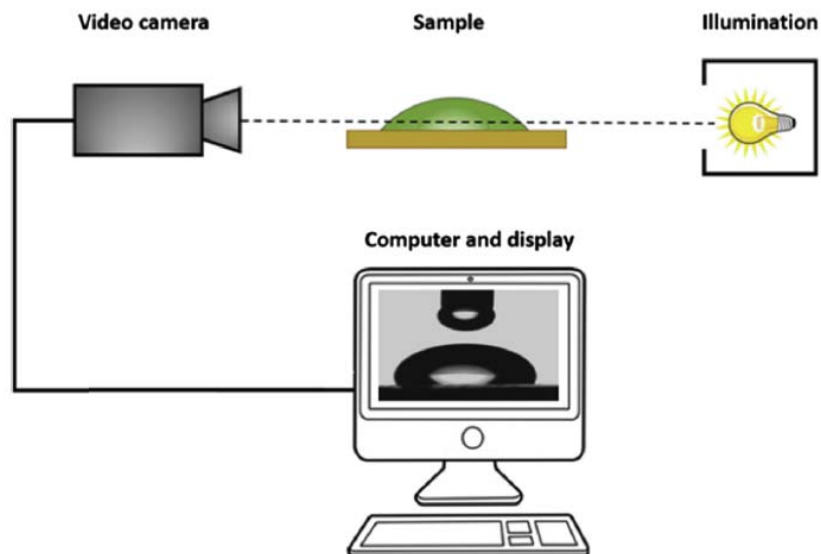


Figure 24. Graphical representation of sessile drop technique for measuring WCA.

### 3.6.5 Mechanical analysis

Microhardness of the prepared coatings was measured using Vickers microhardness tester (FM-ARS9000, Future-Tech Corp., Tokyo, Japan), which is shown in Figure (25). An average value of five microhardness measurements was calculated for each sample at 200 g load for 10s.

The Vickers Hardness tester is equipped with a diamond indenter that has a

pyramid shape, with a  $136^\circ$  apical angle. As the test is started, the indenter is pressed into the sample at a specified load, which creates an indentation with a diamond-like shape, which is then measured from tip-to-tip at x-y axis. Then, the machine automatically converts the average of the resulting measurement into a Vickers Hardness number.

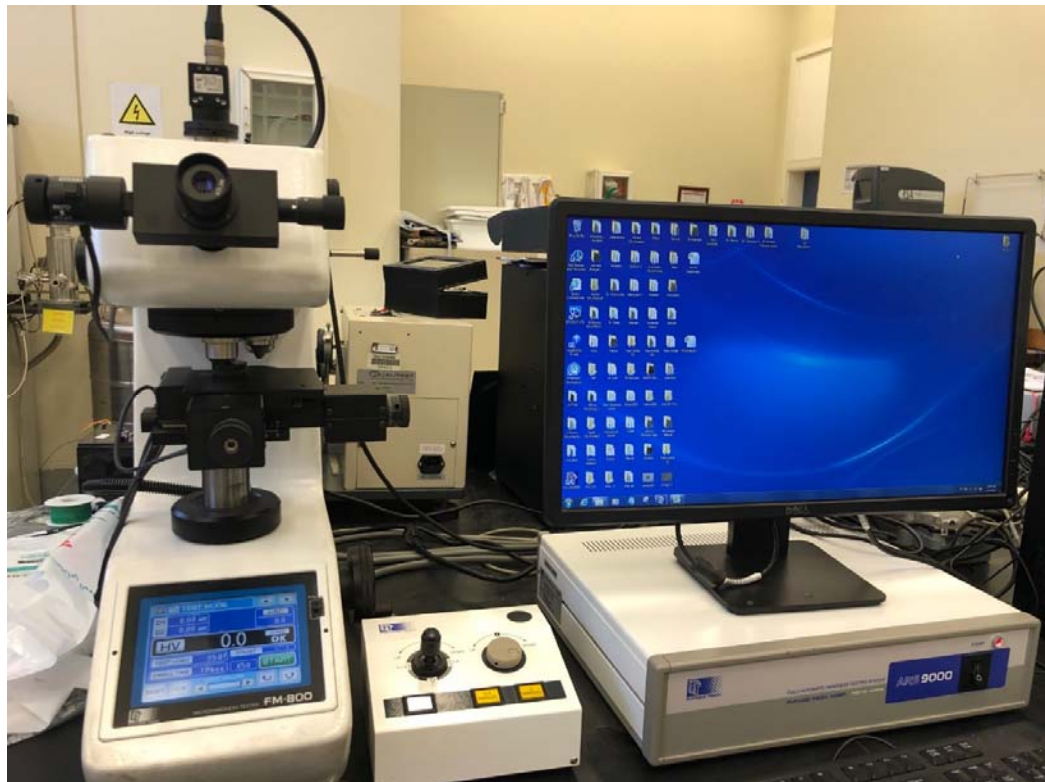


Figure 25. Vicker's microhardness tester, Future-Tech Corp., Japan model

Additionally, the mechanical characterization of the prepared coatings was further emphasized using the nano-indentation test. The measurements were obtained using a nanoindenter head connected to AFM device, at 1 mN maximum indentation force, 200  $\mu\text{N/s}$  loading and unloading rate, and 5s dwell time.

Nano-indentation is probe-based technique, in which a very small tip, with a nano-scale size, presses into the surface of a tested sample at an identified rate and

force. Depending on how far the tip is indented into the sample, the hardness is measured.

### 3.6.6 Corrosion Study

Corrosion can be thought of as an electrochemical process because a small amount of electrical current is also generated as the metals corrode. Four conditions must always exist before corrosion can develop; a metal that corrodes readily (called the anode), a different metal that has less tendency to corrode (called the cathode), and an electrical path between the anode and cathode (usually through metal-to-metal contact), and a conductive liquid called the electrolyte. Electrical current flows from the cathode to the anode through the electrical path which eventually causes the loss of metal in the anode [106].

To study the corrosion resistance of the synthesized NiP and NiP-C<sub>3</sub>N<sub>4</sub> nanocomposite coatings, and to investigate the effect of ZnO concentrations (as a dopant) on the corrosion protection properties, the electrochemical impedance spectroscopy (EIS) and potentiodynamic polarization (PP) (Tafel test) were carried out in a solution of 3.5 wt. % sodium chloride (NaCl) at room temperature.

It is worth mentioning that the EIS plays an important role in fundamental and applied electrochemistry and materials science. In simple words, it is the method of characterizing the electrical behavior of systems in which the overall system behavior is determined by a number of strongly coupled processes, each proceeding at a different rate [107]. On the other hand, Tafel polarization, where the current density can be expressed as a function of the overpotential:

$$\eta = \beta \log (i/i_0),$$

where  $\eta$  is the overpotential,  $\beta$  is the Tafel slope (V),  $i$  is the current density ( $A/m^2$ ), and  $i_0$  is the exchange current density ( $A/m^2$ ). This expression is known as the Tafel equation [108].

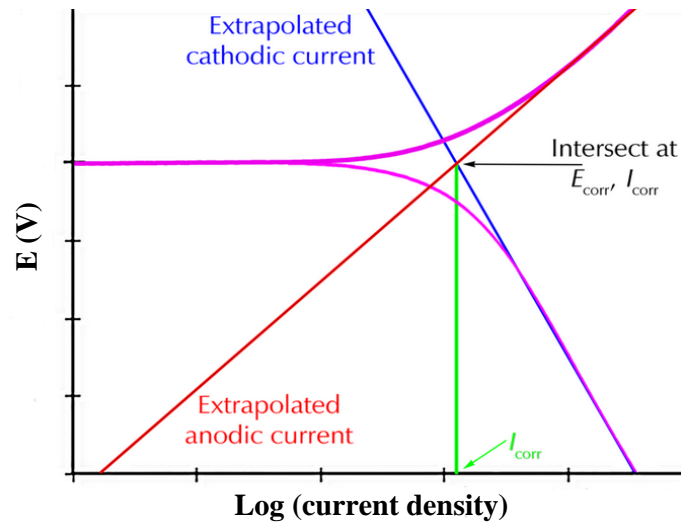


Figure 26. Typical Tafel polarization curve. Ref. [108]

The corrosion resistance measurements were done for all coated samples before and after heat treatment. All corrosion measurements were carried out at 25 °C by utilizing a GAMRY 3000 potentiostat / galvanostat / ZRA device (Warminster, PA, USA) that is shown in Figure (27) and was connected to a three-electrode cell, in which the coated substrate was the working electrode, and the reference and counter electrodes were selected to be Ag/AgCl, and graphite rod, respectively. Figure (28) is a schematic diagram that illustrates the electrochemical corrosion cell. The EIS test was run at an excitation of 10 mV AC, a frequency range between  $1 \times 10^{-2}$  to  $1 \times 10^5$  Hz, and the open circuit potential was always allowed to stabilize before the recording of EIS data starts. On the other hand, the Tafel tests were performed to obtain anodic and cathodic polarization curves by applying a scan rate of  $0.167 \text{ mV s}^{-1}$  within an initial and final

potentials of  $-250$  and  $250$  mV, respectively. The measurements were repeated three times to ensure the reproducibility.

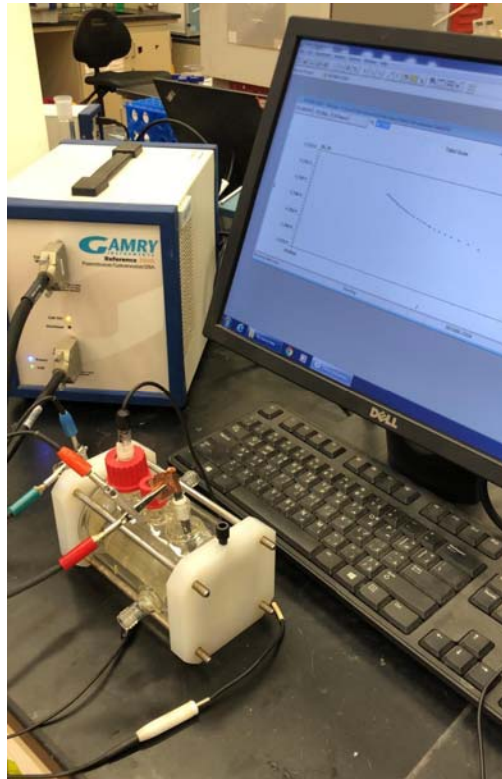


Figure 27. GAMRY 3000 device used for electrochemical measurements.

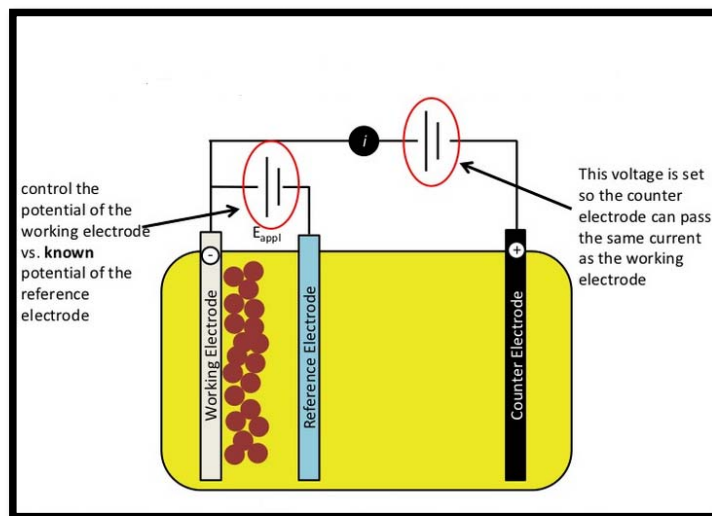


Figure 28. Three electrodes configuration in the corrosion cell.

### 3.6.7 Antibacterial Study

Finally anti-bacterial test was used to investigate the anti-bacterial properties of the prepared nanocomposite coatings before and after heat treatment, which could be achieved using the so-called colony count method.

The prepared specimens of C-steel coated with NiP-C<sub>3</sub>N<sub>4</sub> nanocomposite coatings using undoped and doped C<sub>3</sub>N<sub>4</sub> nanocapsules with different concentrations of ZnO (i.e. 0.5, 1.0, and 2.0g, respectively) were sterilized using 70% ethanol. Using glue and DPX mountant, specimens were glued into a 6 well plates from the lower side where it was not coated. Then, the plate with the specimens were sterilized under UV light for 30 minutes. A bacterial culture of *Staphylococcus aureus* (S.aureus) was allowed to grow in LB broth until the OD at 600nm reached late log phase (1.2 OD). Then, 5ml of the bacterial broth was added to each well having the coated specimen. The plate was incubated in the shaker at 37C° at 50 RPM for 3 hours. After 3 hours, the LB was removed and all specimens were washed with autoclaved distilled water 2 times. After washing, the coated specimens were scraped using a loop and 2ml autoclaved distilled water to remove any bacterial growth if found. Then, the 2ml scrapped bacteria with DW was transferred to Eppendorf tube. A 1:10 serial dilution was performed, then 100ul from the 1:1000 dilution was cultured in agar plate and incubated at 37C° overnight. The next day, bacterial colonies were counted in each plate to calculate colony-forming unit (CFU).

## CHAPTER 4: RESULTS AND DISCUSSION

### 4.1 Structural Analysis (XRD)

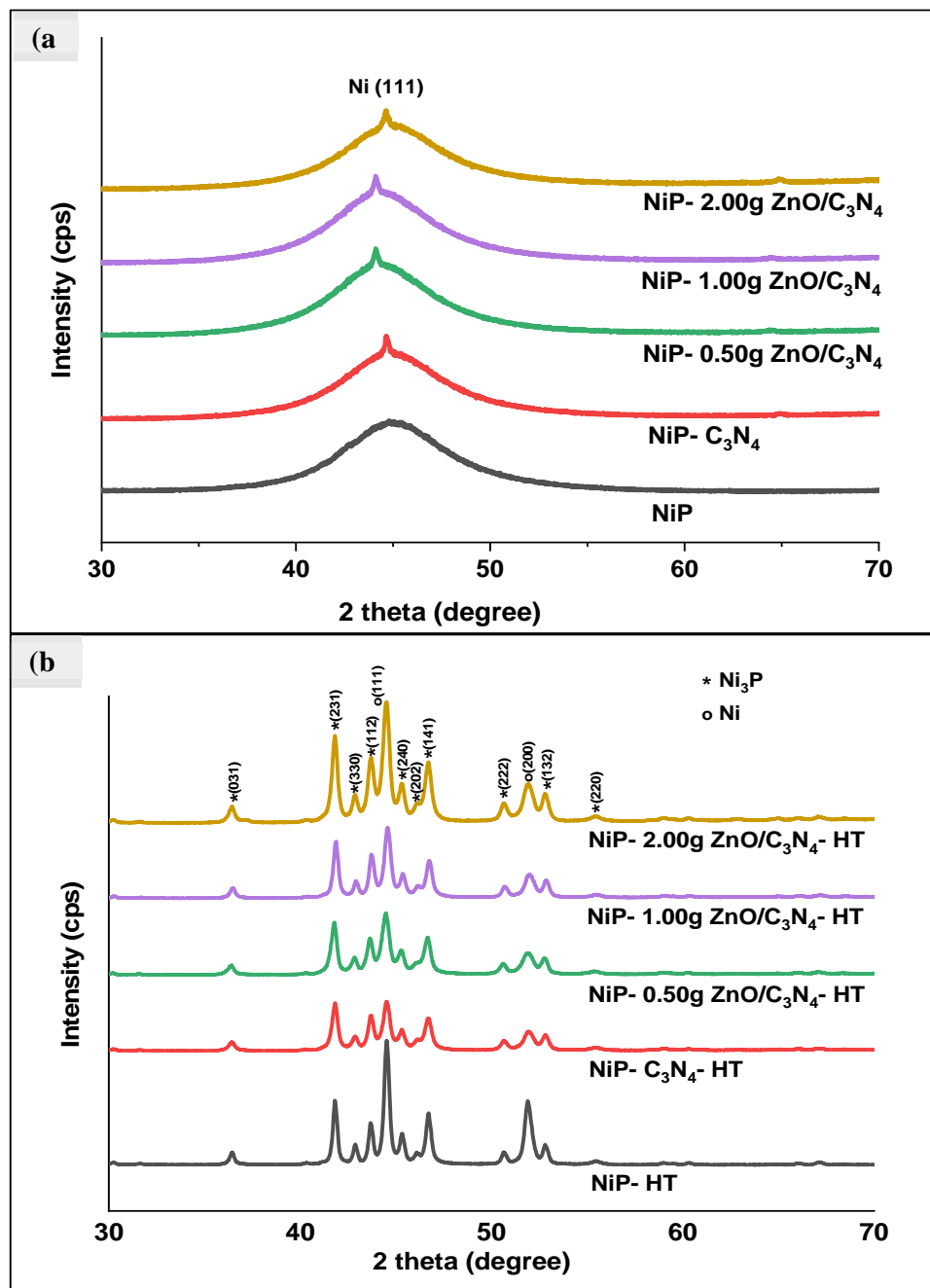


Figure 29. XRD pattern of NiP, NiP-C<sub>3</sub>N<sub>4</sub>, and NiP-C<sub>3</sub>N<sub>4</sub>/ZnO with different concentrations of doped ZnO (0.50, 1.00, and 2.00 g) (a) before and (b) after heat treatment at 400 °C for 1 h.



Figure 29 (a and b) represent the XRD patterns obtained for electroless NiP, NiP-C<sub>3</sub>N<sub>4</sub>, and NiP- C<sub>3</sub>N<sub>4</sub>/ZnO nanocomposite coatings with different concentrations (0.50, 1.00, and 2.00 g) of doped ZnO in C<sub>3</sub>N<sub>4</sub> nanocapsules before and after heat treatment, respectively. It can be seen in Figure (29a) that the as-plated NiP coating has a broad peak extended at the  $2\theta$  position =  $45^\circ$ . This single broad peak is associated with the (111) plane of the face-centered cubic (FCC) Ni. Moreover, all the other nanocomposite coatings show the same single broad peak at the same position, i.e.  $2\theta = 45^\circ$ , and no other peaks that identify C<sub>3</sub>N<sub>4</sub> appear. This might be due to the fine size and small amount of the incorporated C<sub>3</sub>N<sub>4</sub> nanocapsules compared to the high density of the Ni diffraction peaks of the NiP coating. Several researchers have observed a similar result when a small amount of nanomaterial was incorporated in the NiP matrix [28], [109]. Additionally, it can be noticed that after the incorporation of undoped or ZnO doped C<sub>3</sub>N<sub>4</sub>/ZnO nanocapsules in the NiP coating, the structure changes from amorphous to crystalline-amorphous or semi-amorphous state. According to the literature [110], the P content determines the crystal structure of the NiP coating, i.e. high P content ( $\geq 10$  wt.%) gives amorphous structure, whereas medium (5 – 10 wt.%) or low (1 – 5 wt.%) P content leads to a more semi-crystalline or crystalline structure. Since the XRD patterns show amorphous and semi-crystalline structures for C<sub>3</sub>N<sub>4</sub>-free and undoped/doped C<sub>3</sub>N<sub>4</sub> coatings, respectively, the high and medium P content in those coatings is verified, which is in line with the EDX results. Furthermore, the XRD patterns reveal a full width at half-maximum (FWHM) values of 0.6140, 0.5178, 0.5140, 0.5145, and 0.5130 for the NiP, the NiP-C<sub>3</sub>N<sub>4</sub> and NiP-C<sub>3</sub>N<sub>4</sub> that is doped 0.50, 1.00, and 2.00 g with ZnO nanocomposite coatings, respectively. As a result, the refinement of the NiP nodules and the boosting of the crystalline phase formation is achieved in the occurrence of undoped and doped C<sub>3</sub>N<sub>4</sub> in the NiP matrix.

Several studies confirmed that the structure of electroless NiP coating changes from amorphous state to crystalline state by heat treatment [111], which is compatible with the XRD patterns, shown in Figure (29b), obtained for the NiP, NiP-C<sub>3</sub>N<sub>4</sub> and NiP- C<sub>3</sub>N<sub>4</sub>/ZnO with different ZnO concentrations nanocomposite coatings after heat treatment at 400 °C for 1 hour. It can be seen that after heat treatment (HT), NiP crystallizes forming Ni<sub>3</sub>P particles, as well as crystalline Ni phase on the surface of the NiP coating. Additionally, it can be observed that the diffraction peaks of heat-treated undoped and doped NiP-C<sub>3</sub>N<sub>4</sub> nanocomposite coatings match with those obtained for the heat-treated NiP coating with a minor change in the intensity of the resulted peaks, as it slightly decreases for all heat-treated nanocomposite coatings, except for the NiP-C<sub>3</sub>N<sub>4</sub>/2.00g ZnO coating. The reduced peaks' intensity in most of the nanocomposite coatings could have happened due to the decrease in the amount of the deposited Ni and P that occurs upon the incorporation of undoped or doped C<sub>3</sub>N<sub>4</sub> nanocapsules, which are well dispersed in the NiP matrix, as shown in the SEM results. On the other hand, the agglomeration of the doped C<sub>3</sub>N<sub>4</sub> with 2.00g-ZnO nanocapsules in the NiP matrix, as shown in SEM, results in having less or almost no effect on the amount of deposited Ni and P over a wide area of the substrate, as a result of the measurements possibly being taken from such areas.

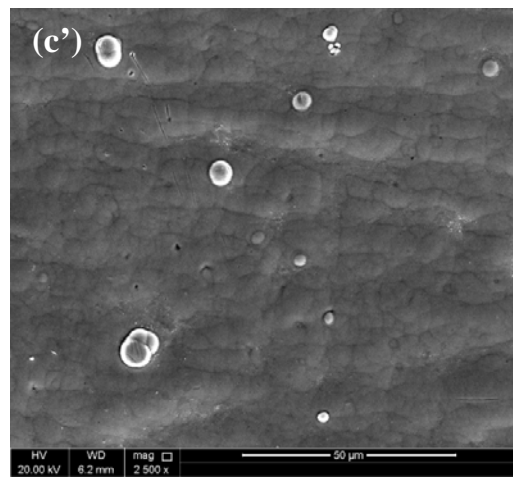
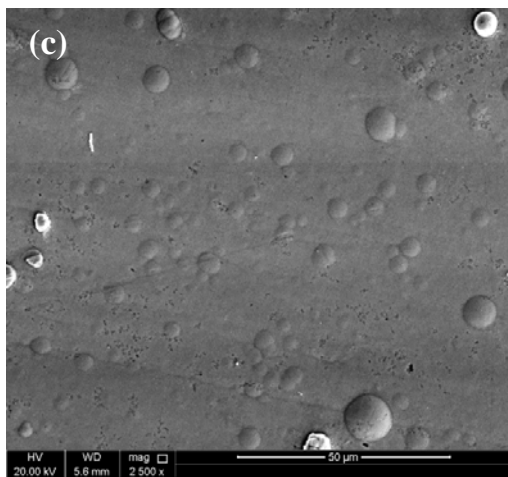
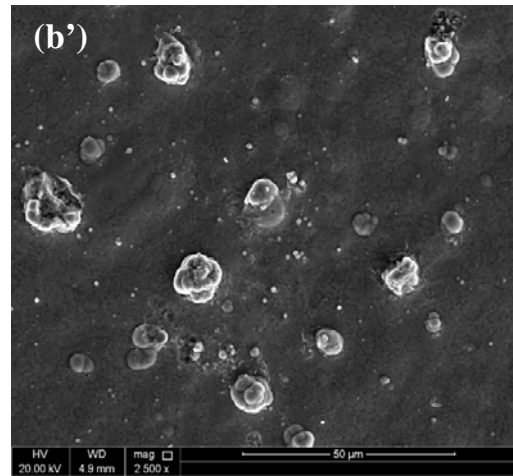
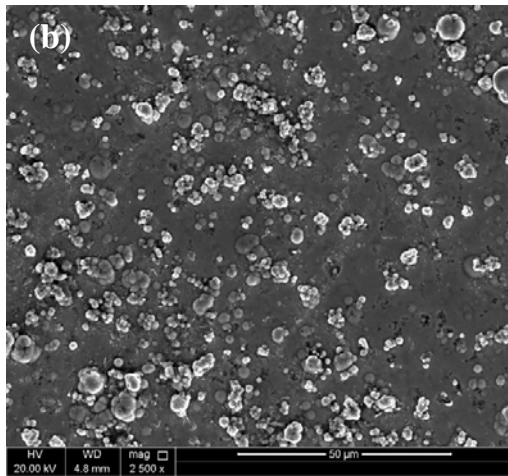
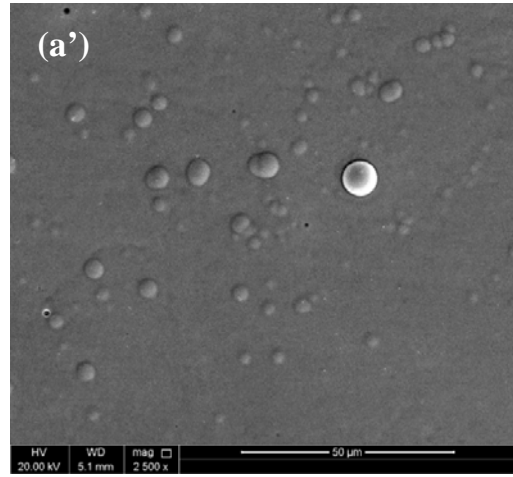
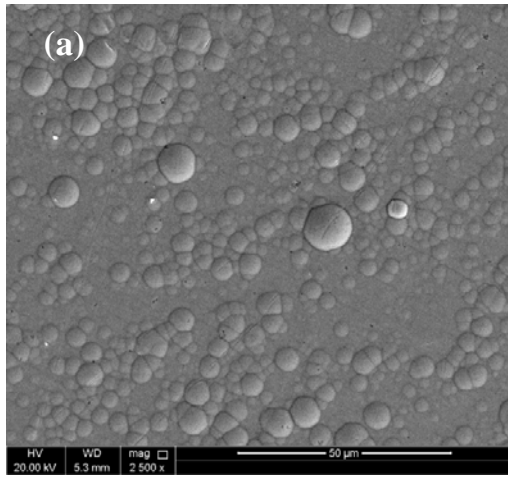
## 4.2 Morphology and Compositional Analysis

### 4.2.1 SEM Analysis

The SEM images shown in Figures 30 (a – e) and (a' - e') represent the surface morphology of as-plated and heat-treated NiP, NiP-C<sub>3</sub>N<sub>4</sub>, and NiP- C<sub>3</sub>N<sub>4</sub>/ZnO coatings doped with different concentrations of ZnO, i.e. 0.5, 1.0, and 2.0 g, respectively. The SEM image of NiP coating shown in Figure (30a) indicates a structure like a cauliflower that is characterized by a feature of spherical nodular, which is similar to the morphology of electroless NiP reported in several works [112], [113]. The incorporation of C<sub>3</sub>N<sub>4</sub> nanocapsules into the NiP matrix does not change the cauliflower shape of the NiP coating, however, it has a considerable effect on the nodules' size and arrangement to some extent. As demonstrated in Figure (30b), which corresponds to as-plated NiP-C<sub>3</sub>N<sub>4</sub> coating, the surface becomes less smooth, and the size of the nodules significantly decreases while their numbers increase. In fact, the change of the morphology confirms that the C<sub>3</sub>N<sub>4</sub> nanocapsules are effectively incorporated in the matrix. Various reports in literature [2], [10], [28] indicated a significant morphology change after the incorporation of other types of nanomaterials in NiP matrix. Doping the C<sub>3</sub>N<sub>4</sub> nanocapsules with ZnO at different concentrations remarkably affects the surface morphology of the nanocomposite coatings, as illustrated in Figures 30 (c - e). It is noticeable that as the concentration of doped ZnO is increased up to 1.00g, the spherical nodules become more homogeneous and compact, which seems outstanding in NiP- C<sub>3</sub>N<sub>4</sub>/1.0 g ZnO. However, as the concentration of the doped ZnO in the C<sub>3</sub>N<sub>4</sub> nanocapsules is further increased to 2.0 g, some agglomeration of nanocapsules clearly emerges on the surface, which greatly affects the uniformity of the coating. Therefore, its homogeneity and compactness is significantly decreased compared to that of 0.50 and 1.00g ZnO doped NiP- C<sub>3</sub>N<sub>4</sub>/ZnO nanocomposite coatings. Furthermore, some pores and voids appear on the surface of NiP-C<sub>3</sub>N<sub>4</sub>/2.00g ZnO composite coating,

which extremely affects the corrosion resistance properties of the coating, as will be discussed later in this chapter. The morphological change of NiP- C<sub>3</sub>N<sub>4</sub>/ZnO nanocomposite coatings is induced by the modification of the nanocapsules' features as the doped ZnO concentration is increased. As proved in various studies [114], increasing the concentration of doped ZnO in C<sub>3</sub>N<sub>4</sub> nanomaterial, significantly increase its surface area and porosity. Moreover, other studies [115], [116] revealed distinctive morphological change of C<sub>3</sub>N<sub>4</sub> nanomaterials upon using different concentrations of doped ZnO.

After heat treatment, the number of nodules significantly decrease and the globular morphology in all of the coatings relatively diminishes compared to the corresponding as-plated coatings. It is also noticeable that the size of the nodules generally decreases and their numbers increase in an ordered manner, which in turn fosters the smoothness of the surface. In general, the surface homogeneity and compactness is enhanced after heat treatment for all of the coatings, namely for that of the HT- C<sub>3</sub>N<sub>4</sub>/1.00g ZnO. The morphology change of the coatings after heat treatment is mostly related to the formation of new phases, as illustrated in XRD analysis. However, at high concentration of doped ZnO, i.e. 2.00g, the surface appears rough, bumpy and agglomerated compared to the HT-0.50 and 1.00g ZnO doped NiP- C<sub>3</sub>N<sub>4</sub>/ZnO nanocomposite coatings. This might be attributed to the high porosity of the nanocapsules induced by the high concentration of doped ZnO, which reduces the overall compactness of the coating, with the newly formed phases after heat treatment.



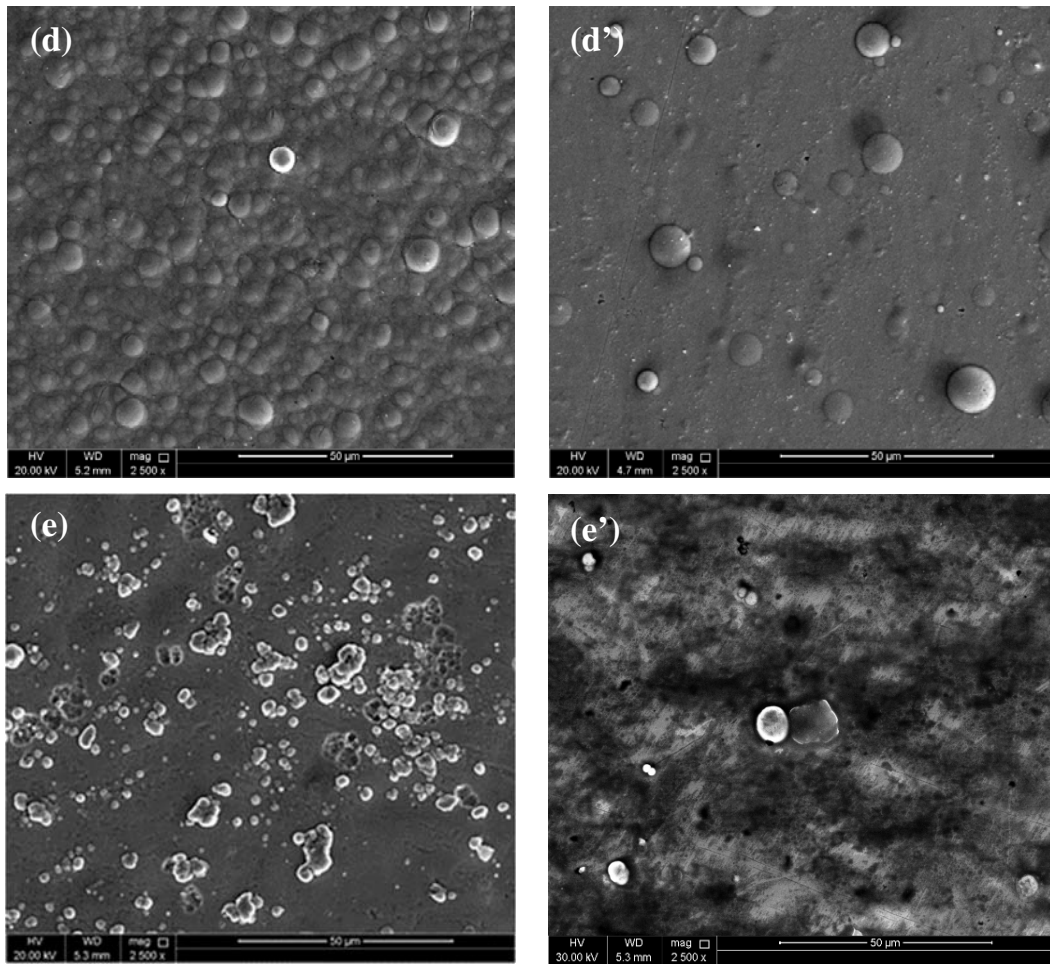


Figure 30. SEM images of (a,a') NiP, (b,b') NiP-C<sub>3</sub>N<sub>4</sub>, (c,c') NiP-C<sub>3</sub>N<sub>4</sub> / 0.50g ZnO, (d,d') NiP-C<sub>3</sub>N<sub>4</sub> / 1.00g ZnO, and (e,e') NiP-C<sub>3</sub>N<sub>4</sub> / 2.00g ZnO, before and after heat treatment at 400°C for 1 h.

#### 4.2.2 EDX Analysis

Tables (5) and (6) summarize the data obtained from the EDX spectra for the different as-plated and heat-treated coatings, respectively. EDX spectra signalize the presence of  $C_3N_4$  nanocapsules in the NiP coating, as the Ni, P, C and N peaks appeared, which confirms their successful incorporation in the coating. The N peak represents the  $C_3N_4$  nanocapsules. In addition, it is observed that the percentage of the P and Ni contents in the  $C_3N_4$  nanocomposite coating is decreased. This can be attributed to the addition of the co-deposited  $C_3N_4$  nanocapsules in the coatings. Moreover, the EDX results of the as-plated coatings show that the phosphorus (P) content is significantly decreased by about 50% after the incorporation of  $C_3N_4$  nanocapsules, i.e. from 18.90 wt. % to 9.63 wt. % P in as-plated NiP and NiP- $C_3N_4$ , respectively. This confirms that the structure of as-plated coatings changes from amorphous to semi-crystalline, which is consistent with the XRD outcomes. As reported in literature [59], [117], the phosphorus amount predicts the microstructure of electroless NiP coatings. For instance the P content is expected to be low (1-5 wt.%) in crystalline structure, medium (5-10 wt.%) in semi-crystalline, and high ( $\geq 10$  wt.%) in amorphous structures.

On the other hand, traces of zinc element (Zn), which is related to the doped ZnO in the nanocapsules, appears only in the EDX spectra of NiP- $C_3N_4$ /ZnO at high concentrations of doped ZnO, i.e. 1.00 and 2.00g. In fact, this is expected as the ZnO nanoparticles are embedded and reacted within the carbon nitride nanostructures, which hardly can be detected by EDX analysis of the coatings, namely at low concentration of ZnO. Since the concentration of either undoped or doped  $C_3N_4$  nanocapsules added to the electroless bath is fixed (0.5 g/L), it is depicted that increasing the concentration of doped ZnO in the different nanocomposite coatings, has a slight effect on the overall compositions of C, N and P content. The slight changes are mainly related to the

variations in the handling process during preparation. However, it is illustrated that the percentages of O in the composite coatings increased, which may be attributed to the increase of the surface area and the porosity of the C<sub>3</sub>N<sub>4</sub> nanocapsules, reflecting on the percentage change of the other elements like Ni.

After heat treatment at 400°C for 1 h, the P content slightly decreases in all the EDX spectra of the heat-treated coatings, which is mainly attributed to the formation of new phases, such as Ni<sub>3</sub>P, as well as the improved crystallinity of the prepared coatings, which confirms the XRD results.

Table 5. EDX analysis for the elemental composition of the different as-plated coatings

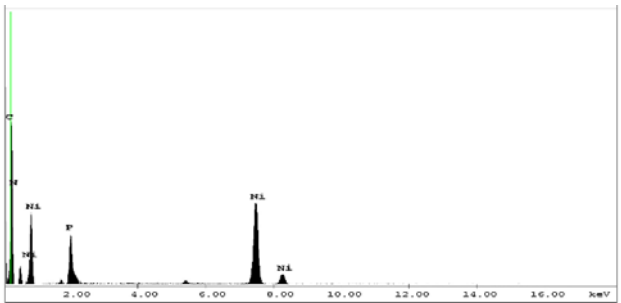
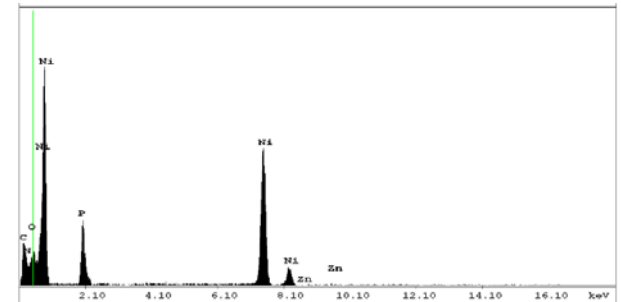
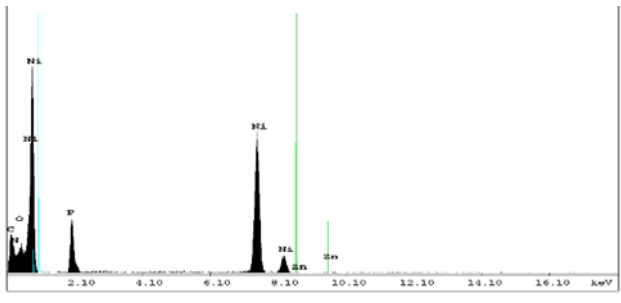
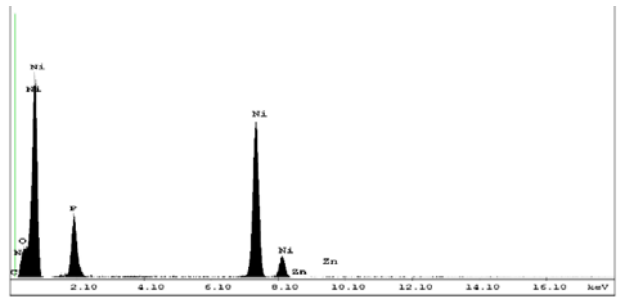
Coating name	Element	Before HT		
		Norm. C (wt. %)	Atom. C (at. %)	Chart
NiP	Ni	81.10	69.36	
	P	18.90	30.64	
	C	---	---	
	N	---	---	
	Zn	---	---	
	O	---	---	
NiP-C <sub>3</sub> N <sub>4</sub>	Ni	65.47	51.21	
	P	9.93	16.90	
	C	15.54	17.19	
	N	8.70	14.70	
	Zn	---	---	
	O	---	---	
NiP-C <sub>3</sub> N <sub>4</sub> (0.50 g ZnO)	Ni	60.03	36.05	
	P	9.23	15.60	
	C	13.32	19.74	
	N	9.00	15.48	
	Zn	0.00	0.00	



	O	8.42	13.13	
NiP-C <sub>3</sub> N <sub>4</sub> (1.00 g ZnO)	Ni	56.04	36.77	
	P	9.59	14.76	
	C	15.17	16.96	
	N	9.61	18.86	
	Zn	0.29	0.30	
	O	9.30	12.35	
NiP-C <sub>3</sub> N <sub>4</sub> (2.00 g ZnO)	Ni	51.22	35.27	
	P	9.11	13.04	
	C	17.51	21.00	
	N	9.71	13.03	
	Zn	0.33	0.38	
	O	12.12	17.28	

Table 6. EDX analysis for the elemental composition of the different heat-treated coatings.

Coating name	Element	After HT		
		Norm. C (wt. %)	Atom. C (at. %)	Chart
NiP	Ni	86.50	77.17	
	P	13.50	22.83	
	C	---	---	
	N	---	---	
	Zn	---	---	
	O	---	---	

NiP-C <sub>3</sub> N <sub>4</sub>	Ni	66.19	48.74	
	P	6.11	11.95	
	C	17.70	24.01	
	N	10.00	15.30	
	Zn	---	---	
	O	---	---	
NiP-C <sub>3</sub> N <sub>4</sub> (0.50 g ZnO)	Ni	44.21	35.68	
	P	06.50	11.03	
	C	25.47	26.62	
	N	14.62	16.73	
	Zn	00.00	00.00	
	O	09.18	11.94	
NiP-C <sub>3</sub> N <sub>4</sub> (1.00 g ZnO)	Ni	45.19	26.77	
	P	06.11	09.89	
	C	26.72	30.32	
	N	14.60	22.00	
	Zn	0.12	00.29	
	O	8.07	10.73	
NiP-C <sub>3</sub> N <sub>4</sub> (2.00 g ZnO)	Ni	44.86	31.60	
	P	05.79	07.93	
	C	25.67	33.32	
	N	13.77	15.65	
	Zn	0.22	0.35	
	O	09.69	11.15	

### 4.2.3 Cross Section Analysis

The cross-section morphology and EDX mapping of the constituent elements for the as-plated and heat-treated NiP, NiP-C<sub>3</sub>N<sub>4</sub>, and NiP- C<sub>3</sub>N<sub>4</sub>/0.5g ZnO (as a representative for other NiP- C<sub>3</sub>N<sub>4</sub>/ZnO nanocomposite coatings), are shown in Figures (31) – (36), respectively. The cross-section micrographs show that all coatings are uniform and have no cracks or defects at the interface between the substrate and the coating, elucidating good coating adhesion. However, the thickness of NiP coating (22 μm) is found to be smaller than that of the NiP-C<sub>3</sub>N<sub>4</sub>, and NiP- C<sub>3</sub>N<sub>4</sub>/0.5ZnO, with thicknesses of (25.4 μm) and (23.7 μm), respectively. Accordingly, the increased thickness is indicative of the induced effect upon the incorporation of C<sub>3</sub>N<sub>4</sub> nanocapsules in the NiP matrix. In fact, previous studies [28] reported that introducing some nanomaterials in the NiP matrix, such as C<sub>3</sub>N<sub>4</sub> nanocapsules in our case, act as a catalytic surface which leads to the acceleration of deposition rate, hence the coating thickness is increased. Moreover, doping the C<sub>3</sub>N<sub>4</sub> nanocapsules with ZnO causes a slight decrease in the thickness of nanocomposite coatings, which is indicative of the improved homogeneity of the coating's morphology. This result is consistent with the highly improved corrosion resistance of NiP-C<sub>3</sub>N<sub>4</sub>/0.5g ZnO and NiP-C<sub>3</sub>N<sub>4</sub>/1.00g ZnO nanocomposite coatings, which will be illustrated later in the electrochemical impedance spectroscopy (EIS) analysis section. Additionally, the EDX mapping of the cross-section clearly shows a uniform distribution and homogeneity of all the constituent elements in all coatings, and confirms that carbon nitride nanocapsules are well dispersed within the thickness of the nanocomposite coatings.

After heat treatment, the thickness of NiP coating considerably decreases from (22 μm) to (14.6 μm), as illustrated in Figure (32), which is mainly attributed to the formation of new phases, and modified crystallographic structure. As previously

demonstrated in the XRD analysis section, after heat treatment at 400°C for 1 h, the structure of NiP coating changes from amorphous to semi-crystalline, which has a more ordered and uniform structure that is consistent with the EDX results and confirms them. On the other hand, only a slight decrease is indicated in the thickness of the nanocomposite coatings, i.e NiP-C<sub>3</sub>N<sub>4</sub> and NiP-C<sub>3</sub>N<sub>4</sub>/0.5ZnO after heat treatment, which are mostly reduced by around 2 to 3 μm. This indicates the incredible effect of the C<sub>3</sub>N<sub>4</sub> nanocapsules (doped and undoped with ZnO) on the enhancement of the coatings thicknesses, which indeed reflects on the excellent corrosion resistivity of the coatings, as illustrated in the EIS analysis outcomes.

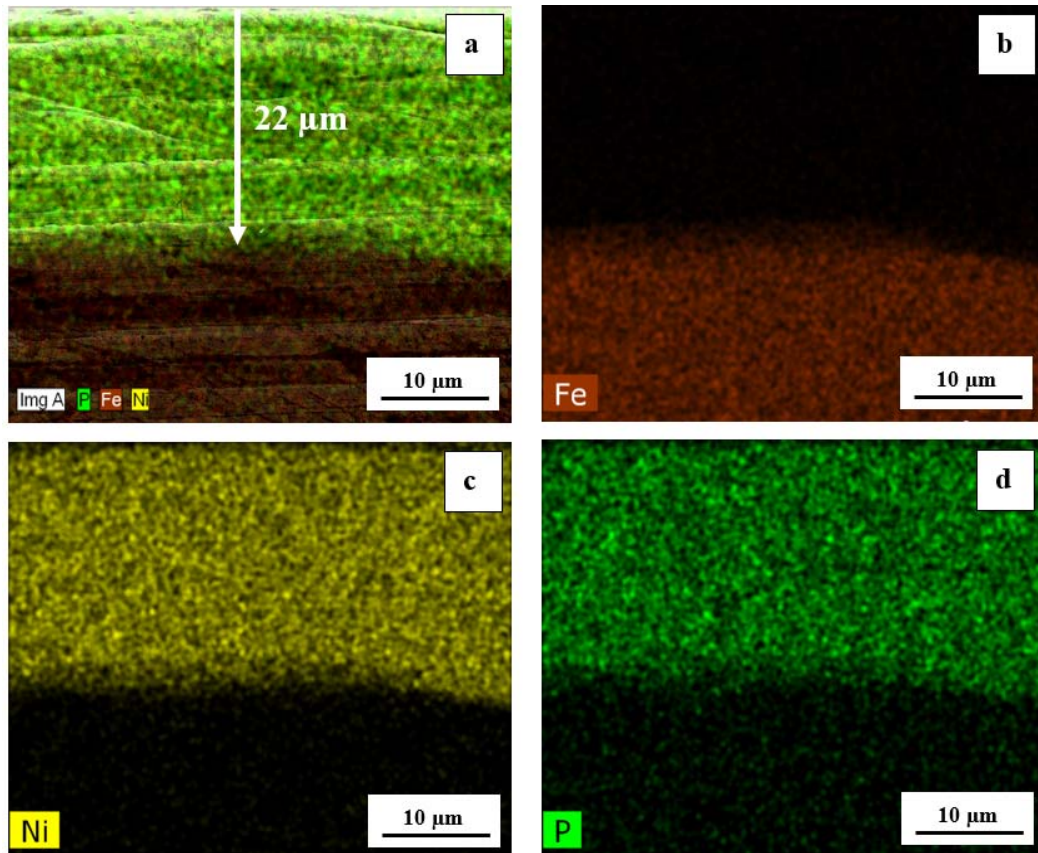


Figure 31. Cross-sectional SEM image of (a) as-plated NiP coating, and (b-d) EDX mapping of its elements.

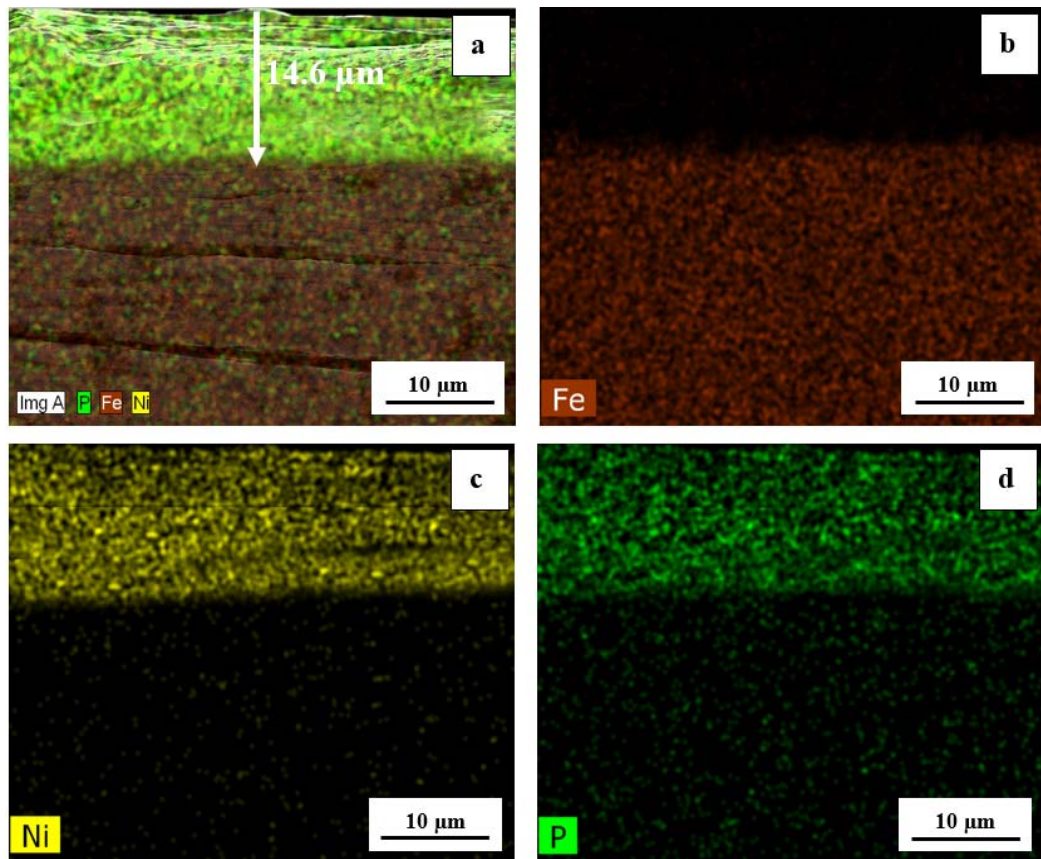


Figure 32. Cross-sectional SEM image of (a) heat-treated NiP coating, and (b-d) EDX mapping of its elements.

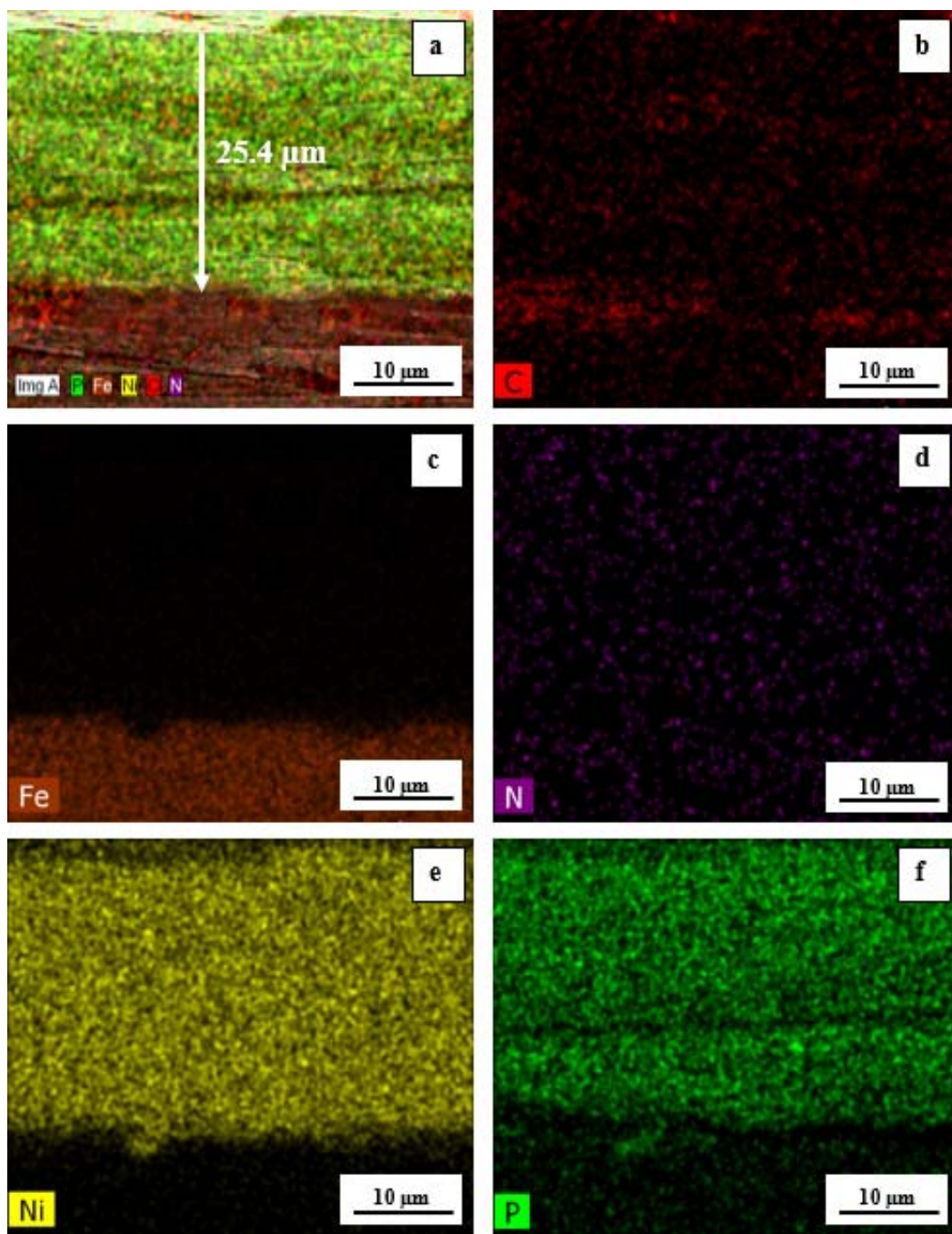


Figure 33. Cross-sectional SEM image of (a) as-plated NiP-C<sub>3</sub>N<sub>4</sub> coating, and (b-f) EDX mapping of its elements.

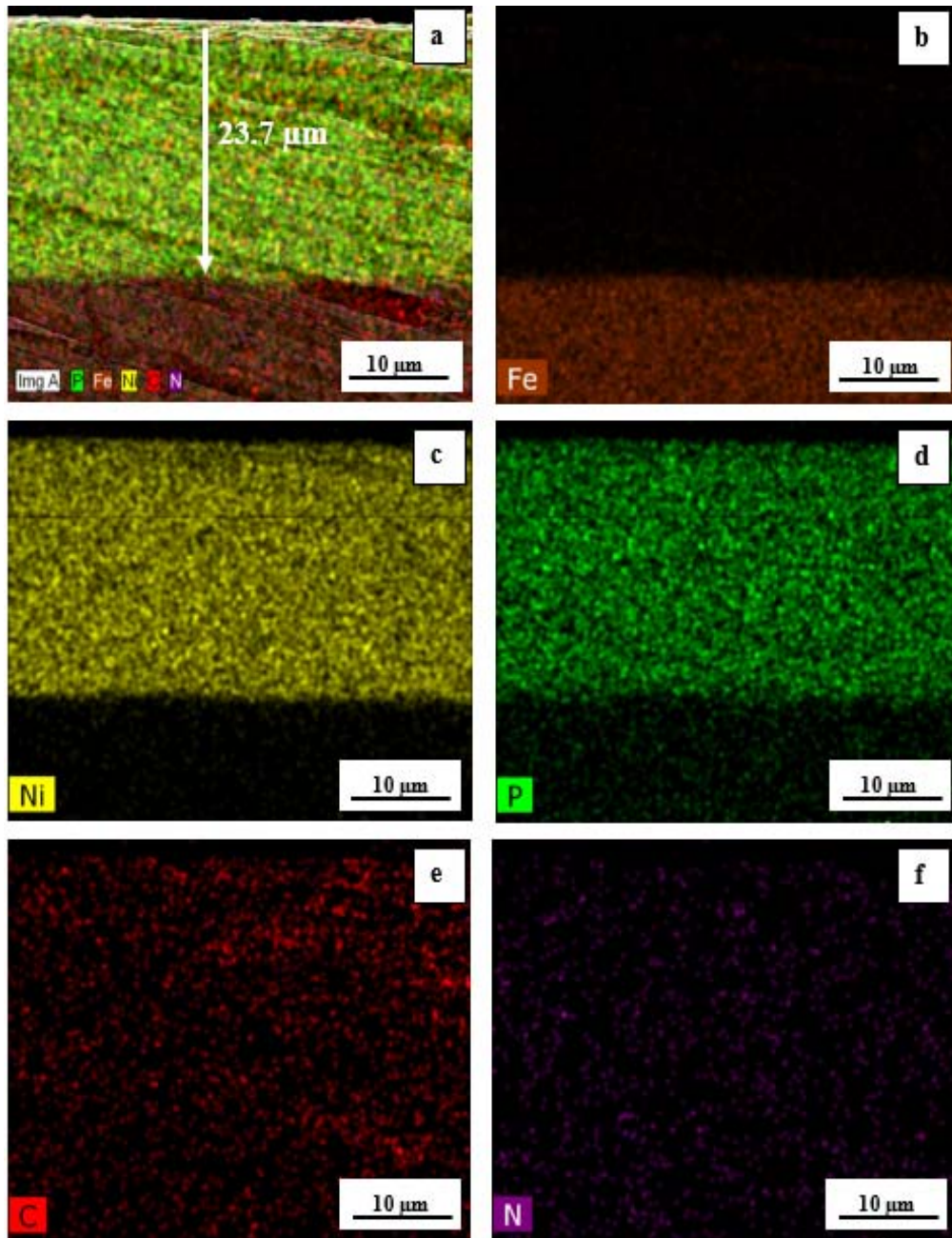


Figure 34. Cross-sectional SEM image of (a) heat-treated NiP-C<sub>3</sub>N<sub>4</sub> coating, and (b-f) EDX mapping of its elements.

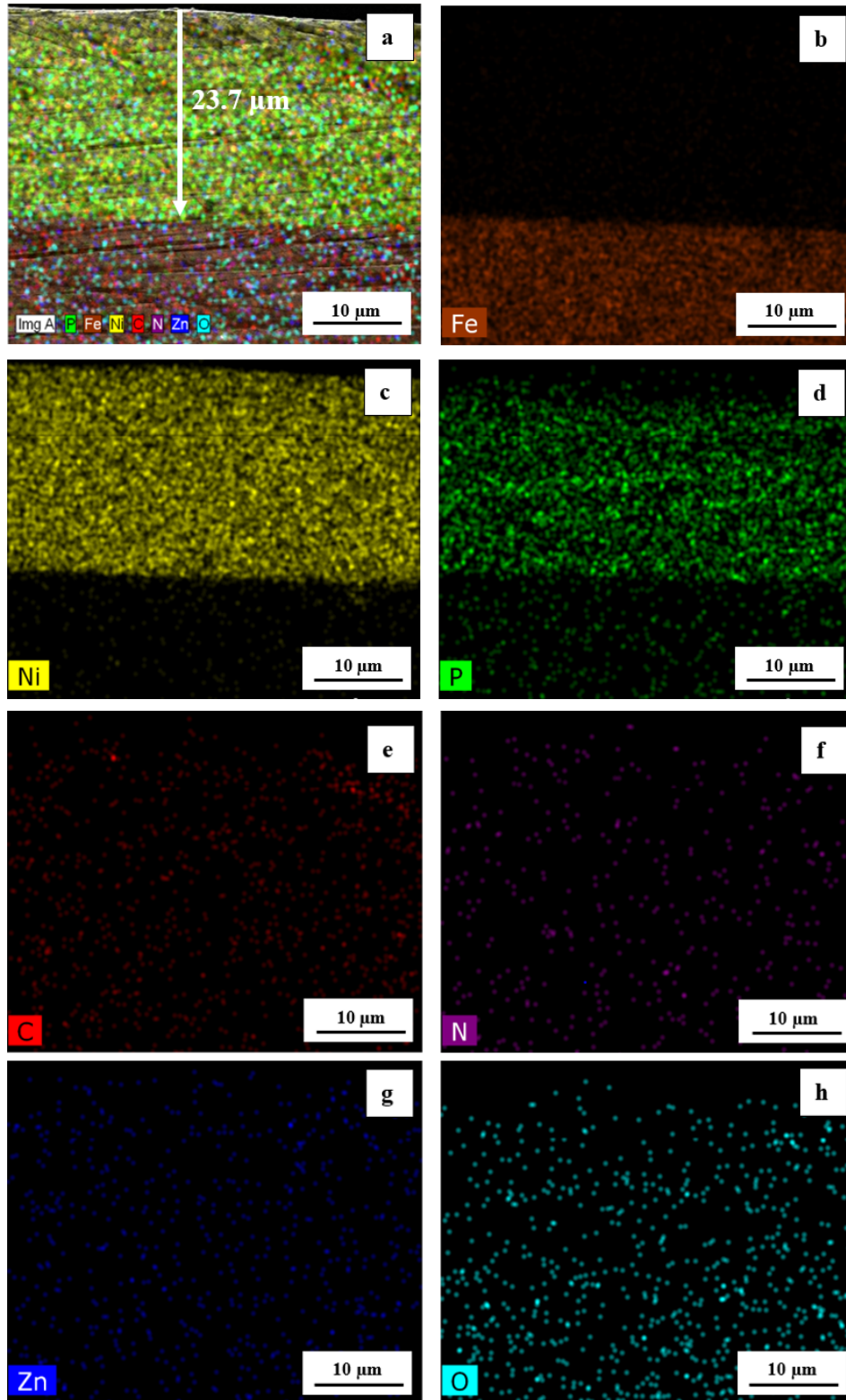


Figure 35. Cross-sectional SEM image of (a) as-plated NiP-C<sub>3</sub>N<sub>4</sub>/0.5g ZnO coating, and (b-h) EDX mapping of its elements.



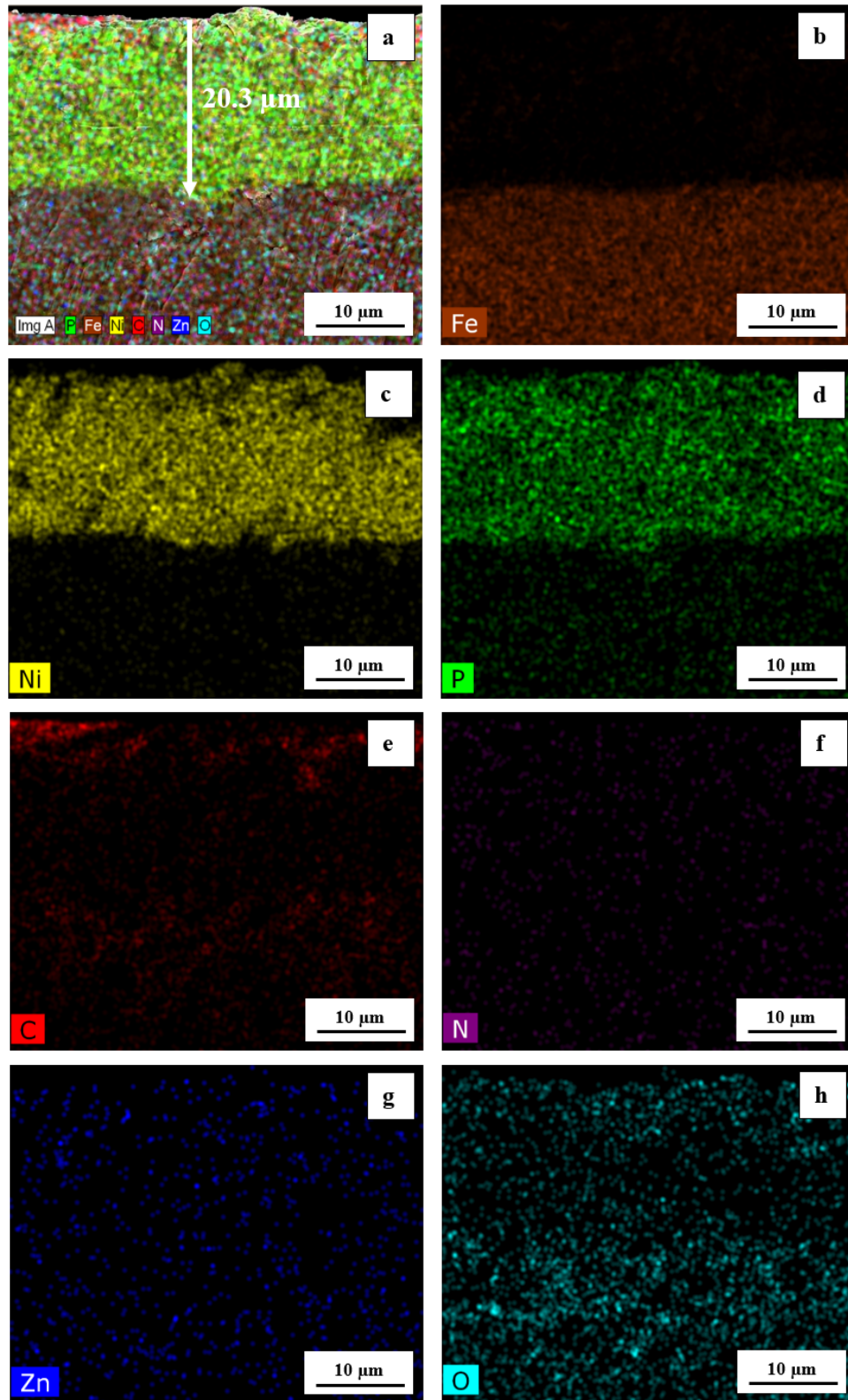


Figure 36. Cross-sectional SEM image of (a) heat-treated NiP-C<sub>3</sub>N<sub>4</sub>/0.5g ZnO coating, and (b-h) EDX mapping of its elements.

#### 4.2.4 TEM Analysis

Figure (37) demonstrates the TEM images of carbon nitride ( $C_3N_4$ ) nanocapsules, and the NiP- $C_3N_4$  nanocomposite coating. It can be seen in in Figure (37a) the successful preparation of capsule-shaped carbon nitride nanomaterial, which was incorporated in the NiP matrix during the preparation of the different nanocomposite coatings. All ZnO-doped and undoped carbon nitride nanocapsules show similar shape and morphology, except for the 2g ZnO doped- $C_3N_4$  nanocapsules reveals a distorted oval-like morphology due to the increased ZnO concentration. The TEM images of all prepared ZnO-doped and undoped  $C_3N_4$  nanocapsules are provided in appendix A. On the other hand, Figure (37b) confirms the excellent distribution of undoped- $C_3N_4$  nanocapsules in the NiP matrix. Doping the nanocapsules with different concentrations of ZnO, i.e. 0.50, and 1.00g, does not affect the homogeneous distribution of nanocapsules in the NiP matrix. However, at high concentration of doped ZnO, i.e. 2.00g, the modified shape of the carbon nitride nanocapsules, leads to its agglomeration in the NiP matrix, which significantly affects the overall mechanical and anticorrosive properties, as will be discussed later in this chapter.

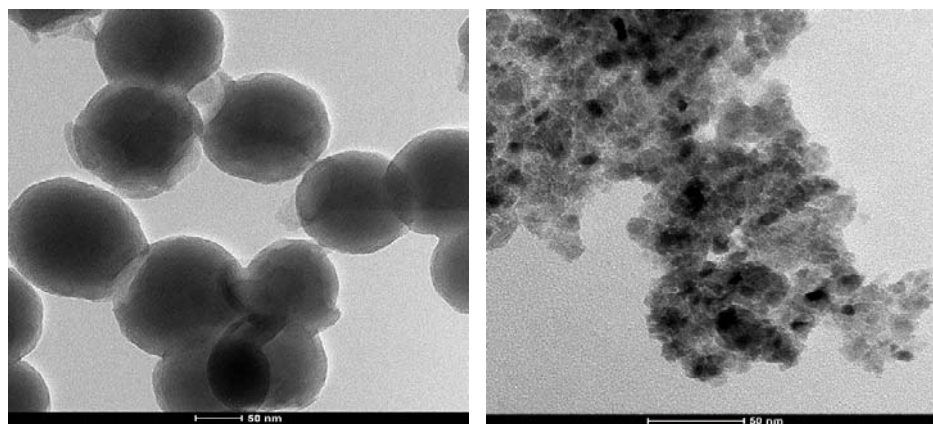


Figure 37. TEM images of (a) carbon nitride ( $C_3N_4$ ) nanocapsules, and (b) electroless coating of NiP- $C_3N_4$ .

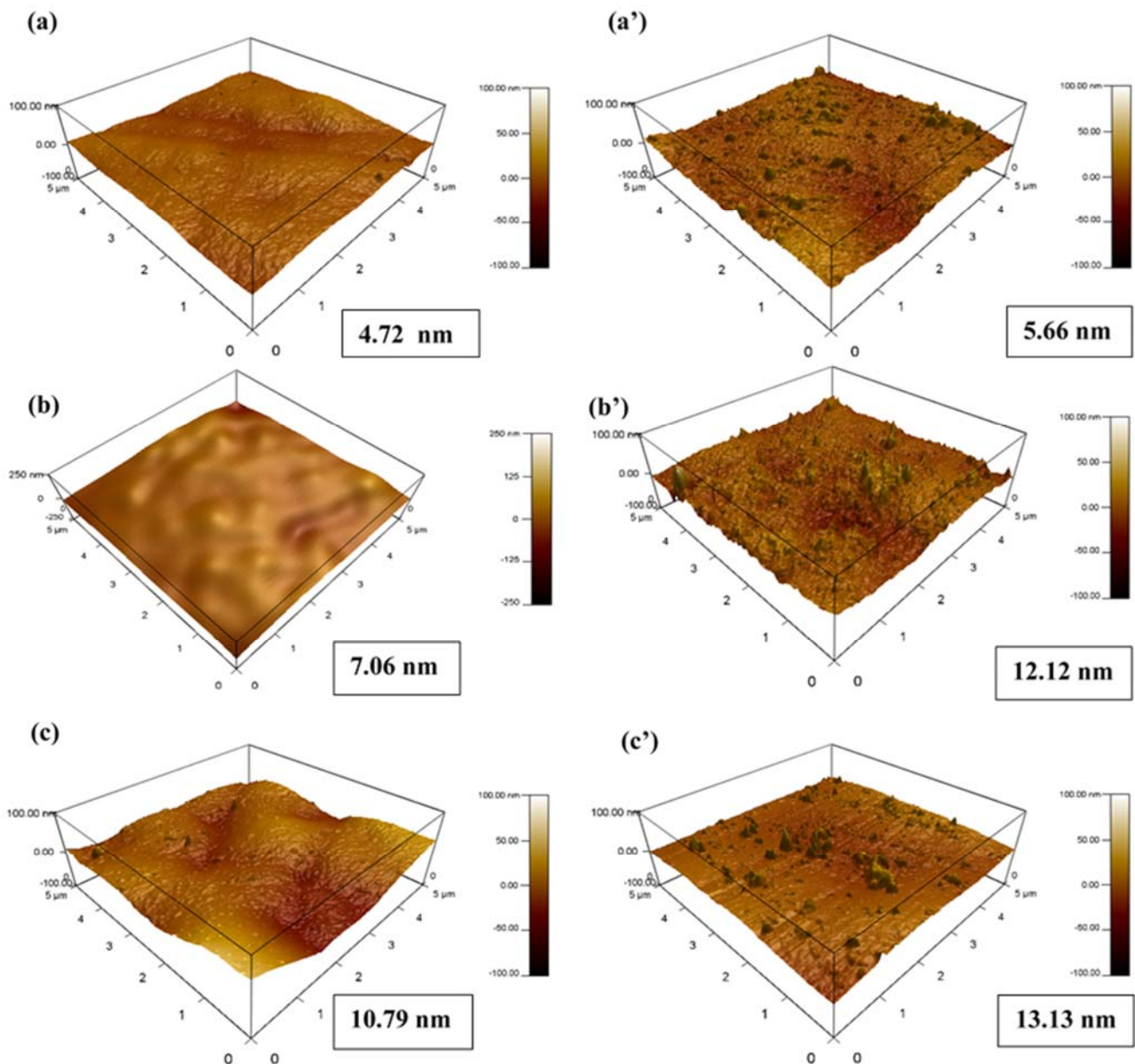
### 4.3 Surface Roughness (AFM) and Water Contact Angle (WCA) Measurements

#### 4.3.1 AFM Analysis

In order to investigate further characteristics of the prepared coatings, Figure 38 shows a 3D AFM images with a measured surface roughness for the different as-plated and heat-treated coatings, obtained by atomic force microscopy (AFM) technique. The measurements indicate that the surface roughness of as-plated NiP is (4.72 nm), whereas that of NiP-C<sub>3</sub>N<sub>4</sub> is (7.06 nm), which reveals that the surface roughness increases after the incorporation of C<sub>3</sub>N<sub>4</sub> nanocapsules in the NiP matrix. Fayyad et al. [10] also reported a significant increase of the surface roughness upon incorporating C<sub>3</sub>N<sub>4</sub> nanosheets in electroless NiP, compared to that of plain NiP coating. Moreover, as shown in Figures 38 (c and d) corresponding to the NiP-C<sub>3</sub>N<sub>4</sub>/0.5g ZnO and NiP-C<sub>3</sub>N<sub>4</sub>/1.00g ZnO nanocomposite coatings, respectively, it is depicted that the surface roughness slightly increases compared to that of NiP-C<sub>3</sub>N<sub>4</sub>, after doping the C<sub>3</sub>N<sub>4</sub> nanocapsules with ZnO. However, increasing the concentration of doped ZnO in the C<sub>3</sub>N<sub>4</sub> nanocapsules from 0.50 to 1.00g shows a negligible effect on the surface roughness, whereas at high concentration of doped ZnO, i.e. 2.00 g, the surface roughness of the coating increases. The slight increase in the surface roughness corresponding to NiP-C<sub>3</sub>N<sub>4</sub>/2.00g ZnO can be attributed to the distorted morphology and agglomeration of the C<sub>3</sub>N<sub>4</sub> nanocapsules upon increasing the concentration of doped ZnO. This result is consistent with the TEM and SEM outcomes that were discussed in the previous sections.

Furthermore, it is noticeable that after heat treatment the NiP coating shows only a slight increase in the surface roughness (less than 1 nm), whereas it remarkably increases for all the nanocomposite coatings. This is indicative of the pronounced effect of the incorporated, doped and undoped, C<sub>3</sub>N<sub>4</sub> nanocapsules on the roughness

properties of the coatings, even after heat treatment. In fact, the results of the surface roughness are, to some extent, in contrary with the XRD and SEM results, which prove more compact and ordered morphology of the nanocomposite coatings after heat treatment. However, it can be said that the increased roughness after heat treatment has a negligible effect on the overall properties of the coatings, namely the corrosion protection efficiency, as will be illustrated in the coming sections.



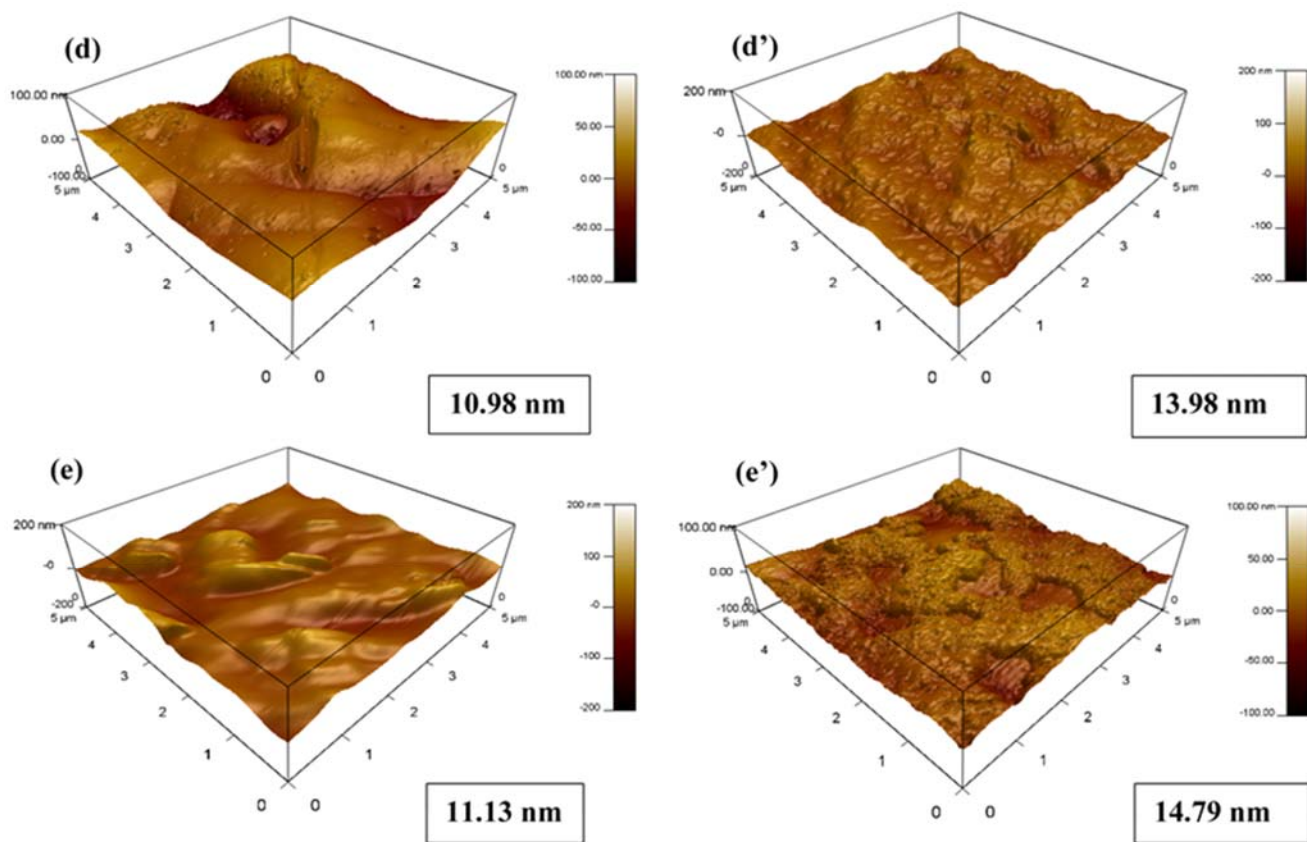


Figure 38. AFM images of (a,a') NiP, (b,b') NiP-C<sub>3</sub>N<sub>4</sub>, (c,c') NiP-C<sub>3</sub>N<sub>4</sub>/0.5g ZnO, (d,d') NiP-C<sub>3</sub>N<sub>4</sub>/1.00g ZnO, and (e,e') NiP-C<sub>3</sub>N<sub>4</sub>/2.00g ZnO coatings, before and after heat treatment at 400°C for 1 h, respectively.

#### 4.3.2 WCA Measurements






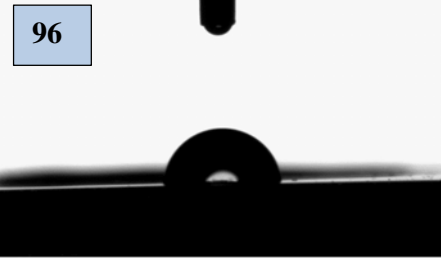

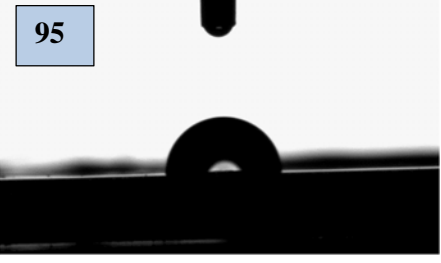


The WCA measurements determine the degree of hydrophobicity or hydrophilicity of a surface, i.e. hydrophilic surfaces exhibit a small water contact angle ( $WCA < 90^\circ$ ), whereas large contact angle ( $WCA > 90^\circ$ ) indicates a hydrophobic surface [118]. As shown in Table (7), the contact angle of NiP is  $100^\circ$ , which reveals hydrophobic behavior. Similarly, Karthikeyan et al. [119] reported hydrophobic behavior of electroless NiP coating. However, the contact angle value increases to  $107^\circ$  for NiP-  $C_3N_4$ , which indicates that the hydrophobic behavior of the coating surface increases after the incorporation of  $C_3N_4$  nanocapsules. On the other hand, doping the  $C_3N_4$  nanocapsules with ZnO has no impact on the wetting properties of the nanocomposite coatings, except at high concentration of doped ZnO, i.e. 2.00g, where the contact angle significantly decreases to  $99^\circ$ . Although NiP- $C_3N_4$ /2.00g ZnO still exhibits hydrophobic behavior, it is considered more hydrophilic compared to all the other as-plated coatings, as they reveal contact angles in the range of ( $100^\circ$ - $107^\circ$ ). It is reported in literature [114], [116] and concluded from BET measurements (Appendix B) that increasing the concentration of doped ZnO in the  $C_3N_4$  nanomaterial significantly increases its porosity, which might eventually influence the compactness of the coating, hence enhances the surface hydrophilicity.

Generally, both the as-plated and heat-treated coatings exhibit hydrophobic surface properties, as the WCA for all of the coatings is higher than  $90^\circ$ . However, the degree of hydrophobicity varies before and after heat treatment. It is noticeable that after heat treatment at  $400^\circ C$  for 1 h, the heat-treated coatings become more hydrophilic compared to the corresponding as-plated coatings. In fact, the increased hydrophilicity under heat treatment conditions contradicts with the surface roughness measurements of the coatings, which increased after heat treatment as illustrated in the AFM analysis.

However, apart from the surface roughness, it is important to consider the microstructure and surface chemistry of the coatings, which play a vital role in determining the surface wettability. As illustrated earlier in XRD and EDX results, new phases form upon heat treatment of the prepared coatings, which led to the reduction of phosphorous content and increase of oxygen. Based on literature [119], the increase in oxygen content is indicative of the formation of an oxide layer on the surface upon heat treatment, which increases the surface wettability. Furthermore, other investigations [120] reported that the modified structure under heat treatment conditions leads to increased surface area which, in turn, increases the wetting area and induces hydrophilic behavior.

Regardless of the slight decrease in the surface hydrophobicity after heat treatment, it is important to keep in mind that the differences in the WCA measurements before and after heat treatment are still considered insignificant. Hence, it does not affect the overall performance of the prepared coatings, namely their corrosion resistance that significantly increases after heat treatment, as illustrated later in the EIS analysis section.

Table 7. Water contact angle (WCA) measurements for the different as-plated and heat-treated coatings.

Coating name	Water contact angle (°)	
	As-plated	Heat-treated
NiP		
NiP-C <sub>3</sub> N <sub>4</sub>		
NiP-C <sub>3</sub> N <sub>4</sub> / 0.50g ZnO		
NiP-C <sub>3</sub> N <sub>4</sub> / 1.00g ZnO		
NiP-C <sub>3</sub> N <sub>4</sub> / 2.00g ZnO		



## 4.4 Mechanical Performance Analysis

### 4.4.1 Vicker's Microhardness Measurements

The microhardness measurements of the deposited NiP- C<sub>3</sub>N<sub>4</sub> nanocomposite coatings without (0.00 g) and with different concentrations (0.50, 1.00 and 2.00 g) of ZnO dopant in comparison with that of the NiP coating, before and after heat treatment, are presented in Figure 39. It can be observed that the incorporation of undoped C<sub>3</sub>N<sub>4</sub> nanocapsules in the NiP matrix considerably increase the microhardness by about 32 %, such that the increase was from 424 to 560 HV<sub>200</sub>. Whereas, the incorporation of the doped C<sub>3</sub>N<sub>4</sub> with 0.50 g ZnO resulted in a further increase of about 21.4 % in the microhardness of the NiP coating reaching a maximum value of 680 HV<sub>200</sub>. Upon further increments in the concentration of ZnO dopant in the C<sub>3</sub>N<sub>4</sub> nanocapsules, namely 1.00 and 2.00 g, the microhardness values of these nanocomposite coatings are decreased to 585 and 450 HV<sub>200</sub>, respectively, compared to the microhardness of the nanocomposite coating with 0.50g ZnO doped C<sub>3</sub>N<sub>4</sub> . However, the microhardness values of these nanocomposite coatings are still higher than that of C<sub>3</sub>N<sub>4</sub>-free coatings. Generally, the increased microhardness values after the incorporation of undoped and doped C<sub>3</sub>N<sub>4</sub> nanocapsules could be attributed to the dispersion hardening effect of the nanocapsules that causes stabilizing the dislocations through restricting the grains growth and plastic deformation of the coating, [10], [121]. Moreover, the highest microhardness obtained for 0.50 g ZnO doped C<sub>3</sub>N<sub>4</sub> nanocomposite coating is mainly related to the uniform dispersion of the nanocapsules in the NiP matrix compared to the other concentrations. As reported [60], the inclusion of ZnO nanoparticles in the NiP coating have increased the microhardness value with increasing its concentration up to a level of 0.50 g/L. Then further increase in the nano ZnO concentration results in decreased microhardness values of NiP composite coating.

A significant increase in the microhardness values of the NiP and the undoped

and doped  $C_3N_4$  nanocomposite coatings is observed after heat treatment of the specimens at  $400^\circ C$  for 1 h. The microhardness of NiP coating increases from 424 to 900  $HV_{200}$ , whereas the microhardness of NiP- $C_3N_4$ , and NiP- $C_3N_4$ / ZnO nanocomposite coatings with different concentrations of ZnO dopant, i.e. 0.50, 1.00, and 2.00 g, increases to 1100, 1330, 1215, and 1080  $HV_{200}$ , respectively. Based on the obtained results, it can be noticed that the trend of the microhardness values of the nanocomposite coatings before and after heat treatment is generally the same. The microhardness after heat treatment gradually increases until a maximum value is obtained at the heat-treated NiP- 0.50g ZnO doped  $C_3N_4$  nanocomposite coating, then it decreases at higher concentrations of ZnO dopant in  $C_3N_4$  nanocapsules, i.e. 1.00, and 2.00 g ZnO. The significant increase in the microhardness of heat-treated coatings is mainly related to the formation of hard  $Ni_3P$  intermetallic phase, which gets harder and more coherent with Ni at elevated temperature, i.e. at  $400^\circ C$ . Other studies [122] reported similar results after heat treatment of different nanoparticle-incorporated NiP composite coatings. Moreover, the presence of undoped and doped  $C_3N_4$  nanocapsules in the NiP coating leads to the transition of its phase from amorphous to semi-crystalline, as illustrated from XRD results, which becomes crystalline after heat treatment. This provides an extra advantage for increasing the microhardness of heat-treated nanocomposite coatings, especially with the well-dispersed 0.50 g ZnO doped  $C_3N_4$  nanocomposite coating. Increased concentrations of ZnO dopant in  $C_3N_4$  nanocapsules (2.00 g) leads to the aggregation of the nanocapsules even after heat treatment, which in turn decreases the microhardness of that nanocomposite coating.

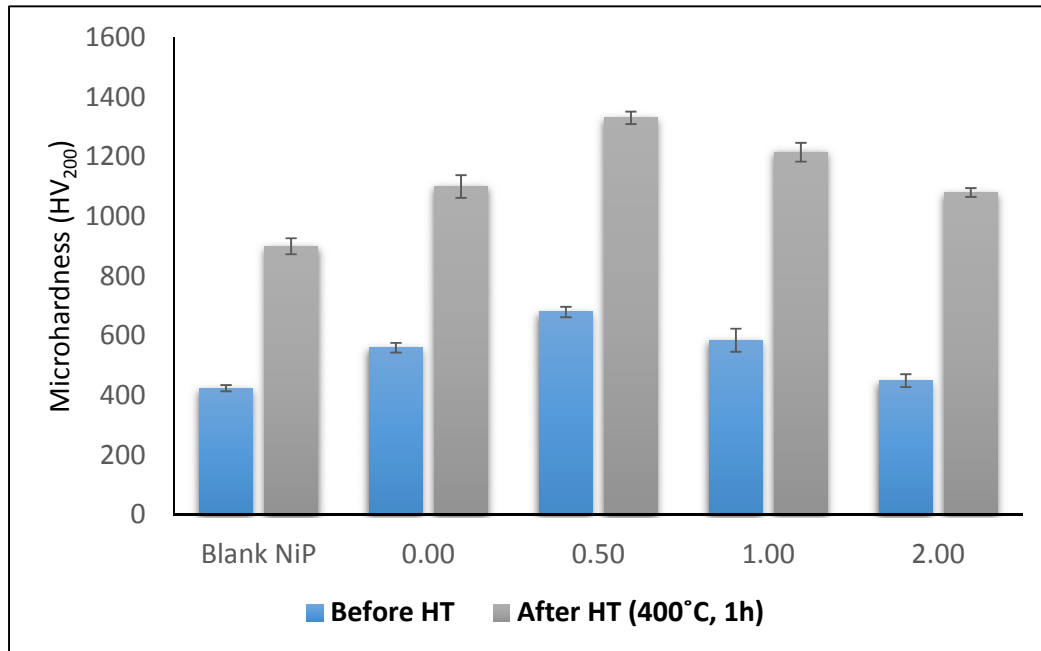


Figure 39. Microharness measurements of the prepared NiP, and NiP- C<sub>3</sub>N<sub>4</sub>/ZnO, with different concentration of ZnO dopant (0.00, 0.50, 1.00 and 2.00 g), nanocomposite coatings before and after HT at 400 °C for 1h.

#### 4.4.2 Nanoindentation Test

The mechanical hardness of the different coatings was also measured using the nanoindentation technique, which operates with nanometer resolution and a depth in the submicron range. Figure (40) presents the loading-unloading curves obtained from the nanoindentation test applied for the NiP, NiP-C<sub>3</sub>N<sub>4</sub> and NiP- C<sub>3</sub>N<sub>4</sub>/ZnO composite coatings with different concentrations of ZnO dopant, i.e. 0.50, 1.00, and 2.00 g, before and after heat treatment at 400 °C for 1h. In this technique, as the indentation depth decreases, the hardness of the coating increases. Accordingly, the variations in the coatings hardness can be clearly seen through the different indentation depths obtained for both as-plated and heat-treated coatings, as shown in Table (8). Generally, the heat-

treated coatings are considered more robust and harder, owing a penetration depths in the range of 48 to 84 nm, whereas the corresponding as-deposited coatings have higher penetration depths in the range of 96 to 190 nm, reflecting their lower hardness values. In addition, it can be noticed that the incorporation of either undoped or doped  $C_3N_4$  nanocapsules decreases the indentation depth of the as-plated nanocomposite coatings in the range of 96 – 183 nm, with hardness ranges from 4.9 to 5.9 GPa, compared to the as-plated NiP coating, which have the highest penetration depth of 190 nm with 4.2 GPa hardness, as shown in Table (8). The smaller displacement in the nanocomposite coatings resulted from the resistance of the NiP matrix to the nanoindenter, showing improved hardness of the coatings upon the addition of  $C_3N_4$  nanocapsules. Among the as-plated coatings, the minimum indentation depth is obtained by the 0.50 g ZnO doped  $C_3N_4$  nanocomposite coating, indicating the highest hardness (5.9 GPa), which is mainly attributed to the well dispersed nanoparticles in the NiP matrix compared to the other nanocomposite coatings. In general, the overall improved mechanical performance of the nanocomposite coatings is mainly attributed to the hindered movement of dislocations in the NiP matrix caused by the presence of undoped or doped  $C_3N_4$  nanocapsules [123]. Upon heat treatment, further increase in the coatings' hardness is observed, as shown in Table (8), possibly due to the precipitation of the hard  $Ni_3P$  (indicated by the XRD pattern after heat treatment, (Fig. 29b). Commonly, various studies [121], [124] have reported the effective increase in the hardness of the NiP and NiP composite coatings after heat treatment, upon the formation of  $Ni_3P$  phase. It is worth mentioning that, as shown in Table (8) and Figure (40), there is agreement between the results of nanoindentation hardness and Vickers microhardness measurements in regards of the pattern and values of microhardness results. For example, the heat-treated 0.50 g ZnO doped  $C_3N_4$  nanocomposite coating has the

highest microhardness value, which was 10.9 GPa, obtained from the nanoindentation technique, and 1330 HV<sub>200</sub>, obtained from the Vickers microhardness, showing both values are related.

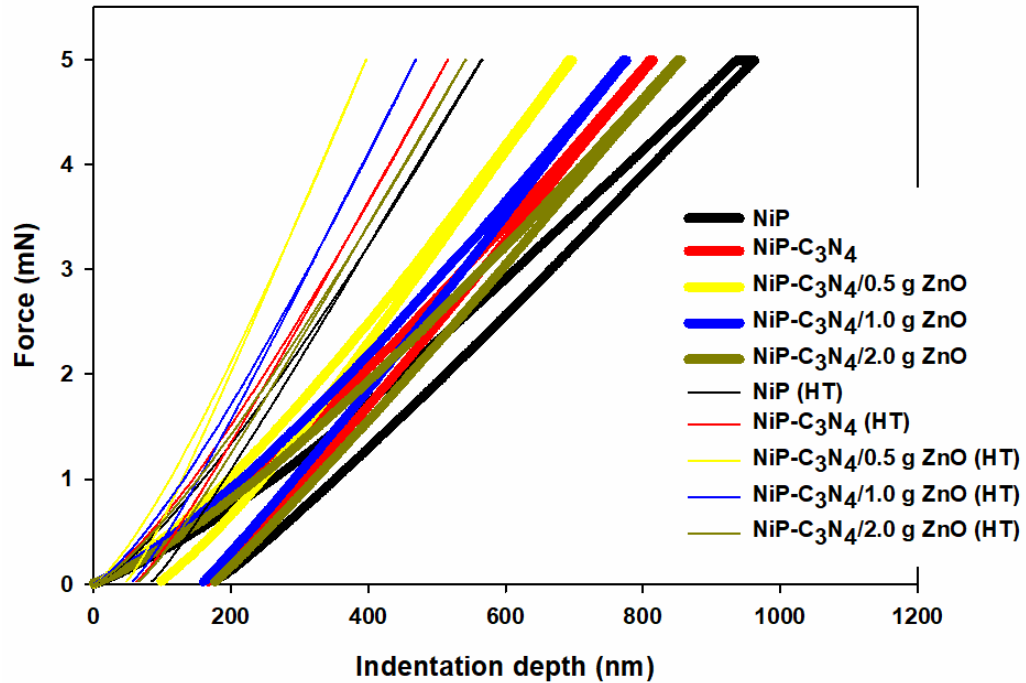


Figure 40. Loading-unloading curves obtained from the nanoindentation test for NiP, NiP/C<sub>3</sub>N<sub>4</sub> and NiP- C<sub>3</sub>N<sub>4</sub>/ZnO nanocomposite coatings, with different concentrations (0.50, 1.00 and 2.00 g) of ZnO dopant, before and after heat treatment at 400 °C for 1h.

Table 8. The penetration depths for the different coatings.

Coating name	Penetration depth (nm)		Nanoindentation hardness (GPa)	
	As-plated	Heat-treated	As-plated	Heat-treated
NiP	190	84	4.2	8.4
NiP-C <sub>3</sub> N <sub>4</sub>	175	61	5.1	9.8
NiP-C <sub>3</sub> N <sub>4</sub> (0.50 g ZnO)	96	48	5.9	12.6
NiP-C <sub>3</sub> N <sub>4</sub> (1.00 g ZnO)	163	58	5.2	10.9
NiP-C <sub>3</sub> N <sub>4</sub> (2.00 g ZnO)	183	67	4.7	9.5

## 4.5 Electrochemical Corrosion Analysis

### 4.5.1 *Electrochemical Impedance Spectroscopy (EIS)*

Figures (41a) and (41b), respectively represents the Bode and phase angle plots obtained from the EIS spectra measured for the substrate C-steel and the as-plated NiP, undoped C<sub>3</sub>N<sub>4</sub> (NiP-C<sub>3</sub>N<sub>4</sub>), and doped C<sub>3</sub>N<sub>4</sub> (NiP-C<sub>3</sub>N<sub>4</sub>/ZnO) nanocomposite coatings with different concentrations (0.5, 1.0, and 2.0 g) of ZnO. The measurements were taken at open circuit potential (OCP) in 3.5% NaCl solution at ambient temperature. It is known that, in Bode plots, the higher the impedance value at low frequency,  $|Z_{0.01} \text{ Hz}|$ , for the examined sample, the higher its corrosion protection that corresponds to lower corrosion rates [125], [126]. As shown in Figure (41a), the  $|Z_{0.01} \text{ Hz}|$  value of the as-plated NiP coating is greater than that of the C-steel metal. Upon the incorporation of C<sub>3</sub>N<sub>4</sub> nanocapsules, either undoped or doped, in the NiP matrix, the  $|Z_{0.01} \text{ Hz}|$  values of the as-plated C<sub>3</sub>N<sub>4</sub> nanocomposite coatings have generally increased compared to that of the C<sub>3</sub>N<sub>4</sub>-free coating. Furthermore, it can be noticed that increasing the concentration of ZnO in the C<sub>3</sub>N<sub>4</sub> nanocapsules, greatly enhanced the  $|Z_{0.01} \text{ Hz}|$  value of the doped C<sub>3</sub>N<sub>4</sub> nanocomposite coating, where the highest  $|Z_{0.01} \text{ Hz}|$  value is obtained for the as-plated 1.0 g ZnO doped C<sub>3</sub>N<sub>4</sub> nanocomposite coating. However, upon further increase in the ZnO dopant concentration (2.0 g), the  $|Z_{0.01} \text{ Hz}|$  value of that doped C<sub>3</sub>N<sub>4</sub> nanocomposite coating is significantly decreased, below that of the undoped C<sub>3</sub>N<sub>4</sub> nanocomposite coating. However, it is still higher than that of the C<sub>3</sub>N<sub>4</sub>-free coating.

The enhancement in the  $|Z_{0.01} \text{ Hz}|$  value of the NiP coating is due to the presence of phosphorous and its reaction with the water forming the hypophosphite layer, which passivates the nickel and protects it from further hydration in the corrosive media [2]. The further enhancement in the  $|Z_{0.01} \text{ Hz}|$  values for the undoped and doped

$C_3N_4$  nanocomposite coatings is mainly attributed to the protective strength of the  $gC_3N_4$  nanocapsules and the ZnO dopants. Moreover, the well distribution of the  $gC_3N_4$  nanocapsules in the NiP matrix had an extra effect in improving the coatings properties, which became denser with less voids and defects, hence reduced the active sites for corrosion attacks. In addition, the increase of ZnO dopant concentration enhanced the compactness of the composite surface, especially at a concentration of 1.0 g as previously demonstrated in the SEM results, which makes it have the highest  $|Z_{0.01} \text{ Hz}|$  value. Furthermore, it is worth mentioning that increasing the concentration of ZnO dopant in the  $C_3N_4$  nanomaterial significantly increases its surface area and porosity, as evident from the literature [114], [116] and our BET results, which is clarified in appendix B. Consequently, when the ZnO was increased to a relatively high amount, the exceedingly increased porosity of the nanocapsules eventually allowed the permeability of the corrosive electrolyte through the coating all the way to the substrate. Additionally, based on TEM measurements for doped  $C_3N_4$  nanocapsules shown in appendix A, the capsule shape of the  $C_3N_4$  is slightly distorted when it is doped with 2 g ZnO becoming oval-shaped, sticky and highly agglomerated. Hence, it is randomly distributed in the NiP matrix, increasing the agglomeration, as clarified in SEM measurements, leading to the reduction of the compactness of the composite coating. Therefore, the aforementioned reasons explained the decreased value of the  $|Z_{0.01} \text{ Hz}|$  for the as-plated 2.0 g ZnO doped  $C_3N_4$  nanocomposite coating compared to that of the undoped  $C_3N_4$  one. On the other hand, it can be concluded that the protective strength of the 1 g ZnO doped  $C_3N_4$  nanocomposite coating overpowered its increasing porosity effect in comparison to the 0.5 g ZnO doped  $C_3N_4$  one.

Commonly known, for the assessment of a coating's protective behavior, the high frequency region is utilized to measure the phase angle, which reflects the capacitive or

resistive characteristic of a coating [127]. In the literature, it was shown that coatings with high corrosion protection usually have high phase angle value ( $\theta$ ) at a frequency of 10 kHz [128]. Obviously, as shown in Figure (41a), the different as-plated coatings have similar shapes and maximal peaks at the high frequencies region, illustrating their protective ability. Nevertheless, there is a considerable variation in their maximal peak values ( $\theta$ ). The 1 g ZnO doped  $C_3N_4$  nanocomposite coatings has the largest  $\theta$  value in the high frequency region compared to the  $\theta$  values of the other coatings, clarifying its superior protection behavior. The  $\theta$  values for the different coatings are increased in the order of NiP [ $65^\circ$ ] < 2 g ZnO doped  $C_3N_4$  [ $70^\circ$ ] < undoped  $C_3N_4$  [ $80^\circ$ ] < 0.5 g ZnO doped  $C_3N_4$  [ $83^\circ$ ] < 1 g ZnO doped  $C_3N_4$  [ $89^\circ$ ]. On the contrary, the phase angle plot of the substrate has a different shape compared to the coatings samples and its maximal  $\theta$  value is at  $60^\circ$ , which appears at the lower frequencies side, and is lower than the  $\theta$  values of the different coatings. This indicates a significant high electrical capacitance behavior that leads to a higher corrosion rate [129], which is due to the high consumed electrons from the steel surface by the electrolyte.

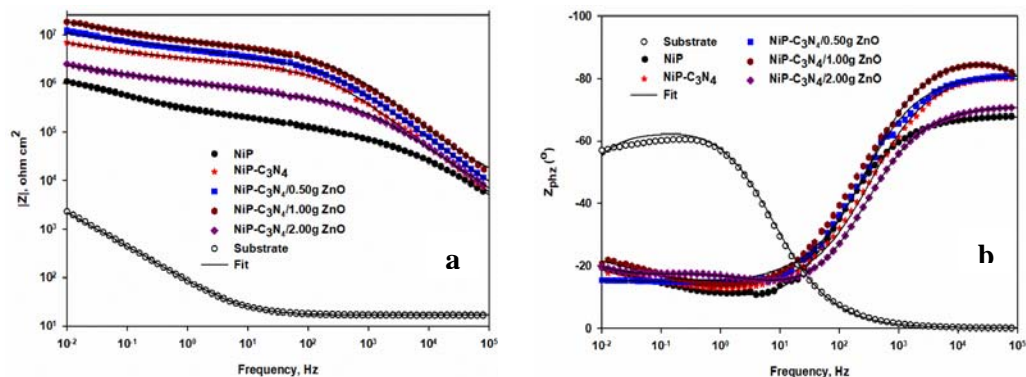


Figure 41. (a) Bode and (b) phase angle plots of the substrate and the as-plated NiP, NiP- $C_3N_4$  and NiP- $C_3N_4$ /ZnO nanocomposite coatings, with different concentrations of ZnO dopant, in 3.5 wt.% NaCl solution at room temperature



Figure (42b) shows the corresponding Nyquist plots for the as-plated NiP, undoped  $C_3N_4$  (NiP- $C_3N_4$ ), and doped  $C_3N_4$  (NiP- $C_3N_4/ZnO$ ) nanocomposite coatings with different concentrations (0.5, 1.0, and 2.0 g) of ZnO in 3.5 wt. % NaCl. The magnifications of the low impedance regions of the Nyquist plots of the different coatings can be seen in the inset in Figure (42b). The corresponding Nyquist plot for the substrate can be seen in Figure (42a) for clearer representation. All Nyquist plots are obtained in the frequency range between 100 kHz - 0.01 Hz. The smaller the diameter of the Nyquist semicircle, the smaller the resistive ability of the coating. It is observed that the Nyquist curves of the different as-plated coatings have the same semi-circular shape, which are different compared to that of the substrate. However, the size and area under the Nyquist curves of the different coatings were considerably different. The similar shape reveals that all of the as-plated coatings undergo the same corrosion mechanism, whereas the different size is indicative of the different corrosion protections. Therefore, according to the area under the curve for each coating, it is noted that they have the same trend and are consistent with their corresponding Bode plots. For example, the 1 g ZnO doped  $C_3N_4$  nanocomposite coating has the largest area under its semi-circle, clarifying that it has the highest corrosion resistance compared to the other coatings.

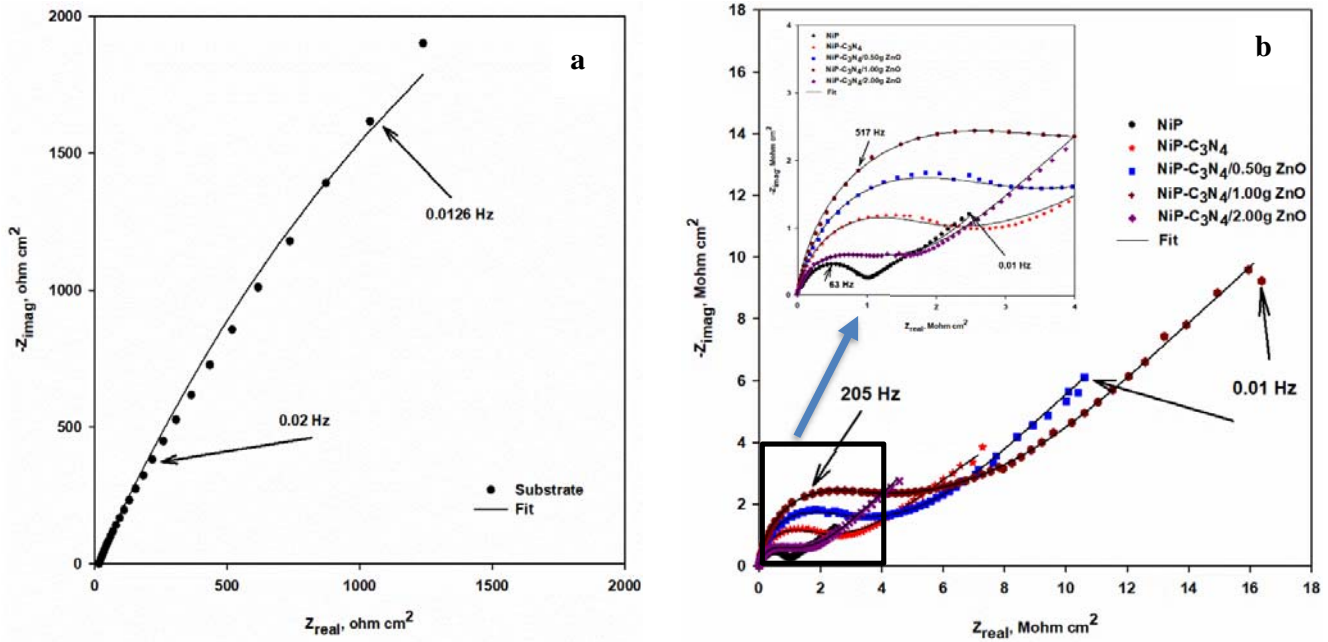


Figure 42. Nyquist plots of (a) the substrate and (b) the as-plated NiP, NiP- C<sub>3</sub>N<sub>4</sub> and NiP- C<sub>3</sub>N<sub>4</sub>/ZnO nanocomposite coatings, with different concentrations of ZnO dopant, in 3.5 wt% NaCl solution at room temperature. Inset is the enlargement of the low frequency region.

To analyze the diversity in the impedance spectra of the substrate and the different composite coatings, the resulted EIS data were fitted using proper fitting program. It is noteworthy that, in Figures (41) and (42), the different colored symbols are the measured EIS data, and the black solid lines represent the fitted data created by using the equivalent two-time constants electrical circuit with Warburg diffusion element ( $W$ ), which is shown in Figure (43). The full fitted parameters are summarized in Table (9). In the equivalent circuit, the  $R_{po}$ ,  $R_{ct}$ , and  $R_s$  refer to the pore, charge transfer, and solution resistance, respectively. At high frequency, i.e.  $|Z_{100 \text{ kHz}}|$ , in the Bode plots, the intercept corresponds to the value of  $R_s$ , whereas, the intercept value at low frequency, i.e.  $|Z_{0.01 \text{ Hz}}|$ , equals the sum of  $R_{po}$ ,  $R_{ct}$ , and  $R_s$ . The  $CPE_{dl}$  and  $CPE_{coat}$  represent the substrate and composite coating constant phase elements, respectively. Finally, the occurrence of electrolyte diffusion is illustrated by the Warburg diffusion

element ( $W$ ) [130]. The CPE, which is pseudo-capacitive element, is utilized to regulate the deviation of the inhomogeneous surfaces, which is obtained due to the roughness or the non-uniform current distribution at the surface [80], from the ideal capacitive behavior. The impedance value of CPE can be calculated using the following Equation [131],

$$Z_{CPE} = \frac{1}{Y_0(j\omega)^n}$$

Where  $Y_0$  refers to the CPE constant,  $j$  represents the imaginary number,  $\omega$  denotes the angular frequency of the AC signal (1/rad), and  $n$  is the CPE exponent and its value is fluctuated from 0 to 1 and referred to the state of the working electrode surface. If  $n$  becomes 1, the CPE displays the ideal capacitor behavior. In addition, the double layer capacitance of the different coatings can be evaluated using the equation below [132],

$$C_x = \sqrt[n]{\frac{Y_{0x}}{R_{0x}^{(n-1)}}}$$

Where  $Y_{0x}$  denotes to the CPE constant for the coating ( $Y_{01}$ ), or the substrate ( $Y_{02}$ ), and  $R_x$  refers the pore coating resistance ( $R_{coat}$ ) or the charge transfer resistance ( $R_{ct}$ ). The substrate/coating interface is demonstrated by the low frequency time-constant, which corresponds to  $CPE_{dl}$  and  $R_{ct}$  as combined together, while the combination of  $CPE_{coat}$  and  $R_{po}$  is related to the high frequency time constant, which demonstrates the coating/solution interface.

As noticed from Table 9, the  $R_{ct}$  value of the NiP coating was about 180 times of the  $R_{ct}$  value of the substrate. This is attributed to the fullness of the NiP coating surface with the phosphorus that results due to the dissolution of the nickel at open

circuit potential. The incorporation of the undoped or doped  $C_3N_4$  nanocapsules, with different ZnO dopant concentrations, in the NiP coating resulted in a significant enhancement in the  $R_{ct}$  values of their composite coatings compared to that of the  $C_3N_4$ -free coating. For example, the  $R_{ct}$  value of the undoped  $C_3N_4$  composite coating is increased by about 11.8 times compared to that of the NiP coating. Furthermore, the doping of the  $C_3N_4$  nanocapsules with 0.5 g ZnO led to an increase in the  $R_{ct}$  value of the composite coating by 1.2 times. Whereas, doubling the concentration of the ZnO dopant in the  $C_3N_4$  nanocapsules, from 0.5 to 1.0 g, resulted in almost doubling the  $R_{ct}$  value of the undoped  $C_3N_4$  composite coating. However, further increase in the ZnO dopant concentration (2.0 g) in the  $C_3N_4$  nanocapsules minimizes the  $R_{ct}$  of the composite coating by 47% compared to the undoped  $C_3N_4$  composite coating; however, it is still 5.5 times higher than that of the  $C_3N_4$ -free coating. This is attributed to the well distribution of the undoped or doped  $C_3N_4$  nanocapsules in the NiP matrix that leads to an increase in the compactness of the composite coatings, by different degrees, improving their protective performance by diminishing any defects and voids present in the composite coatings. Although the porosity of the doped  $C_3N_4$  nanocapsules increases with the increase in the concentration of the ZnO dopant, as proved from the literature and our BET results (appendix B), the doped  $C_3N_4$  composite coatings showed superior barrier performance against the chloride solution, especially with the 1g ZnO dopant, which demonstrates the highest protection efficiency reaching up to 99.97 %. The higher porosity effect of the doped  $C_3N_4$  nanocapsules clearly appear with the highest concentration (2 g) of the ZnO dopant leading to decreases in the protection efficiency of the composite coating in regards to the undoped  $C_3N_4$  composite coating but its efficiency is still higher than that of the  $C_3N_4$ -free coating. Likewise, it is noticed that the pore resistance  $R_{po}$  values of the different as-plated undoped and doped

nanocomposite coatings have the same increasing and decreasing trend as their corresponding  $R_{ct}$ . Furthermore, the embedding of 1 g ZnO dopant in the  $C_3N_4$  nanocapsules in the NiP coating increases the  $R_{po}$  value of the resulting NiP- $C_3N_4$ /ZnO nanocomposite coating, as shown in Table 9, where there is up to 390 % increase in comparison with the corresponding  $R_{po}$  value of the undoped  $C_3N_4$  nanocomposite coating. It is worth mentioning that the different as-plated undoped and doped nanocomposite coatings have lower capacitances ( $C_{dl}$ ) and ( $C_{coat}$ ) than those of the NiP coating and the lowest double layer and coating capacitances values correspond to 1 g ZnO doped  $C_3N_4$  composite coating. This is indicative of the efficient impermeability of that coating for the aggressive corrosive ions. Hence, reflecting its superior protection ability against corrosion [2], [10], [28].

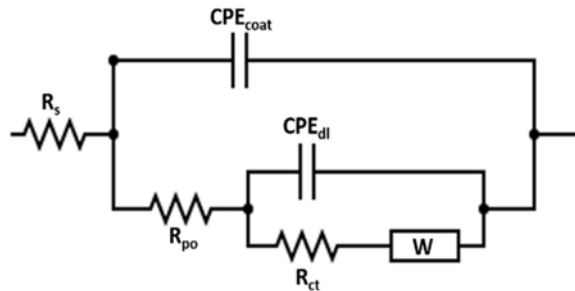


Figure 43. Two-time constants equivalent circuit that fits the experimental impedance results of the different as-plated and heat-treated coatings.

Table 9. EIS-equivalent circuits fitting parameters of the substrate and the as-plated NiP, NiP-C<sub>3</sub>N<sub>4</sub> and NiP-C<sub>3</sub>N<sub>4</sub>/ZnO nanocomposite coatings, with different concentrations of ZnO dopant, in 3.5 wt. % NaCl solution at room temperature.

Coating type	$R_{po}$ (k $\Omega$ .cm <sup>2</sup> )	CPE <sub>coat</sub>		$C_{coat}$ ( $\mu$ F.cm <sup>-2</sup> )	$R_{ct}$ (M $\Omega$ .cm <sup>2</sup> )	CPE <sub>dl</sub>		$C_{dl}$ ( $\mu$ F.cm <sup>-2</sup> )	$W \times 10^{-9}$ (S.s <sup>1/2</sup> )	P.E. (%)
		$Y_{01} \times 10^{-9}$ (s <sup>n</sup> ohm <sup>-1</sup> cm <sup>-2</sup> )	$a_1$			$Y_{02} \times 10^{-9}$ (s <sup>n</sup> ohm <sup>-1</sup> cm <sup>-2</sup> )	$a_2$			
CS	3.50	1323	0.89	0.68083	0.005	3094	0.93	2.26071	---	---
NiP	10.2	555	0.76	0.10831	0.90	675	0.76	0.63154	456	99.44
NiP-C <sub>3</sub> N <sub>4</sub>	247	261	0.90	0.19246	10.6	465	0.88	0.57799	365	99.95
NiP-C <sub>3</sub> N <sub>4</sub> (0.5 g ZnO)	865	157	0.87	0.11650	12.5	339	0.91	0.39104	230	99.96
NiP-C <sub>3</sub> N <sub>4</sub> (1.0 g ZnO)	960	80.7	0.92	0.06460	22.8	296	0.97	0.31400	189	99.97
NiP-C <sub>3</sub> N <sub>4</sub> (2.0 g ZnO)	100	277	0.89	0.17781	4.95	843	0.88	1.02431	367	99.87

Figures (44a), (44b) and (45), respectively, represent the Bode, phase angle and Nyquist plots, which are measured at open-circuit potential, of the heat-treated NiP, NiP-C<sub>3</sub>N<sub>4</sub> (undoped) and NiP-C<sub>3</sub>N<sub>4</sub>/ZnO (doped) nanocomposite coatings, with different concentrations of ZnO dopant, in 3.5 wt% NaCl solution at room temperature. The fitted EIS data for the different heat-treated coatings are represented in Table (10). From Figures (44a), (44b) and (45), it is demonstrated that the Bode, phase angle and Nyquist plots of the different heat-treated coatings have the same increasing and decreasing trend as their corresponding as-plated ones. For example, in Figure (44a), the  $|Z_{0.01} \text{ Hz}|$  of the heat-treated undoped C<sub>3</sub>N<sub>4</sub> coating is higher than that of the heat-treated NiP coating. Furthermore, the different heat-treated doped C<sub>3</sub>N<sub>4</sub> with different concentrations of ZnO dopant have higher  $|Z_{0.01} \text{ Hz}|$  than that of the heat-treated undoped C<sub>3</sub>N<sub>4</sub> one and the highest  $|Z_{0.01} \text{ Hz}|$  was achieved with the 1 g ZnO doped C<sub>3</sub>N<sub>4</sub> nanocomposite coatings. However, the different heat-treated coatings have higher  $|Z_{0.01} \text{ Hz}|$  values than those of their corresponding as-plated ones. Regarding the phase

angle plots of the different heat-treated composite coatings, their maximal peaks ( $\theta$ ) are also in the same order of the corresponding as-plated ones but with a slight increase in their values, as seen in Figures (44b) and (41b). Thus, the order is as follows: NiP [ $60^\circ$ ] < 2 g ZnO doped  $C_3N_4$  [ $74^\circ$ ] < undoped  $C_3N_4$  [ $80^\circ$ ] < 0.5 g ZnO doped  $C_3N_4$  [ $86^\circ$ ] < 1 g ZnO doped  $C_3N_4$  [ $91^\circ$ ]. Similarly, the Nyquist plots of the different heat-treated coatings have higher semi-circle diameters than those of the corresponding as-plated one. On the other hand, all the corresponding Nyquist curves obtained for the different heat-treated coatings, as presented in Figure (45), revealed the same semi-circle shapes, but with different sizes and maximal values. Consequently, the same fundamental electrochemical processes have taken place for all heat-treated coatings. Similar to the as-plated coatings, the fitting of the obtained measurements for heat-treated samples followed the two-time constants equivalent circuit, with a Warburg diffusion element, as demonstrated in Fig. (43). Additionally, The phase angle plots for the different heat-treated coatings, at the analyzed frequency range, show two relaxation process, verifying the two-time constants behavior.

In fact, there was a sharp increase in the corrosion resistance ( $R_{po}$  and  $R_{ct}$ ) of the different coatings after heat treatment, as illustrated in Table (10). This is mainly attributed to the altered morphology and crystallographic structure of the composite coatings upon heat treatment, as previously discussed in the XRD measurements. Furthermore, comparing the fitting parameters for the as-plated and heat treated coatings (Tables 9 and 10), it can be noticed that the capacitance values, i.e.  $C_{coat}$  and  $C_{dl}$ , after heat treatment, are decreased compared to those obtained for as-plated coatings. This implies that the heat-treated coatings are denser and less porous, compared to as-plated ones, which prevented the permeability of the corrosive electrolyte ions through the coatings, hence greatly enhancing its corrosion resistance.

It is evident in the literature that the proper heat treatment of the NiP coating can considerably enhance its corrosion resistance as new phases can be formed, inducing a denser and less porous structure [133].

It is noteworthy that the  $R_{po}$  and  $R_{ct}$  resistances, after HT, of the undoped  $C_3N_4$  nanocomposite coating are increased by about 118 % and 35 %, respectively, as compared to its values before HT. In addition, after HT the  $R_{po}$  and  $R_{ct}$  of the coatings improved upon the increase of the ZnO dopant concentration. Therefore, the heat-treated 1 g ZnO doped  $C_3N_4$  nanocomposite coating offered about 28 % and 31 % increase in its  $R_{po}$  and  $R_{ct}$  values in regards to its corresponding as-plated one, respectively, and about 7 % and 63 % compared to those of the 0.5 g ZnO doped  $C_3N_4$  nanocomposite coating. In addition, as it is previously mentioned with the as-plated coating, the heat-treated 1 g ZnO doped  $C_3N_4$  has the highest  $R_{po}$  and  $R_{ct}$  values compared to the other heat-treated coatings, followed by a significant decrease in the corrosion resistance  $R_{po}$  and  $R_{ct}$  values upon further increase in the concentration of ZnO dopant. This great enhancement can be related to the excellent compactness and homogeneity of the heat-treated 1 g ZnO doped  $C_3N_4$  nanocomposite coating, as previously illustrated in the SEM and EDX results.



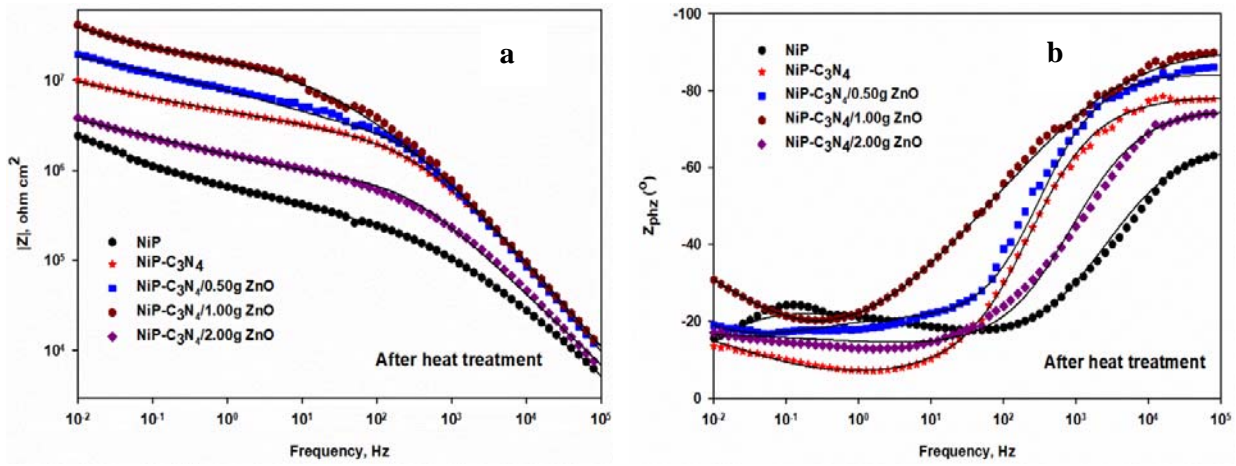


Figure 44. (a) Bode and (b) phase angle plots of the heat-treated NiP, NiP-C<sub>3</sub>N<sub>4</sub> (undoped) and NiP-C<sub>3</sub>N<sub>4</sub>/ZnO (doped) nanocomposite coatings, with different concentrations of ZnO dopant, in 3.5 wt% NaCl solution at room temperature.

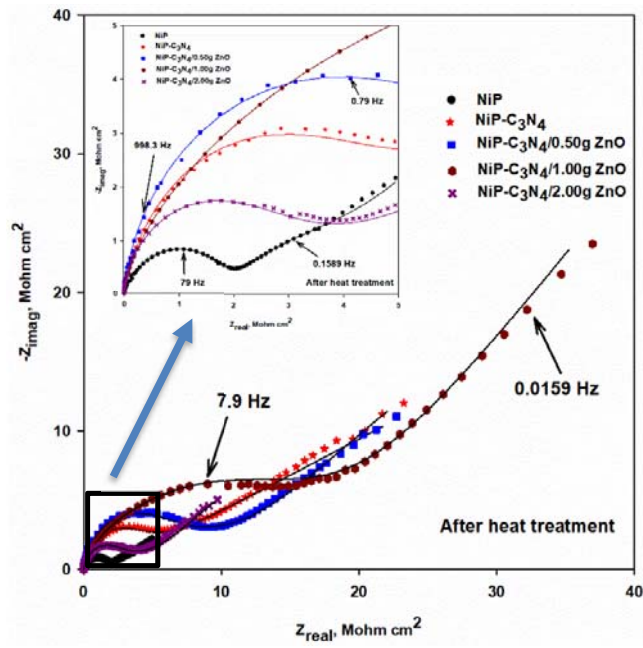


Figure 45. Nyquist plots of the heat-treated NiP, NiP-C<sub>3</sub>N<sub>4</sub> (undoped) and NiP-C<sub>3</sub>N<sub>4</sub>/ZnO (doped) nanocomposite coatings, with different concentrations of ZnO dopant, in 3.5 wt.% NaCl solution at room temperature. The inset is the enlargement of the low frequency regions.

Table 10. EIS-equivalent circuits fitting parameters of the heat-treated NiP, NiP-C<sub>3</sub>N<sub>4</sub> and NiP-C<sub>3</sub>N<sub>4</sub>/ZnO nanocomposite coatings, with different concentrations of ZnO dopant, in 3.5 wt. % NaCl solution at room temperature.

Coating type (HT)	$R_{po}$ (k $\Omega$ .cm <sup>2</sup> )	CPE <sub>coat</sub>		$C_{coat}$ ( $\mu$ F.cm <sup>-2</sup> )	$R_{ct}$ (M $\Omega$ .cm <sup>2</sup> )	CPE <sub>dl</sub>		$C_{dl}$ ( $\mu$ F.cm <sup>-2</sup> )	$W_x$ 10 <sup>-9</sup> (S.s <sup>1/2</sup> )	$P.E.$ (%)
		$Y_{01} \times 10^{-9}$ (s <sup>n</sup> ohm <sup>-1</sup> cm <sup>-2</sup> )	$a_1$			$Y_{02} \times 10^{-9}$ (s <sup>n</sup> ohm <sup>-1</sup> cm <sup>-2</sup> )	$a_2$			
NiP	12.5	3.53	0.88	0.00089	5.20	60	0.94	0.05570	360	99.90
NiP-C <sub>3</sub> N <sub>4</sub>	539	2.61	0.80	0.00050	14.3	25	0.93	0.02313	213	99.96
NiP-C <sub>3</sub> N <sub>4</sub> (0.50g ZnO)	1147	1.59	0.83	0.00044	18.3	24	0.85	0.02075	153	99.97
NiP-C <sub>3</sub> N <sub>4</sub> (1.00g ZnO)	1229	1.51	0.82	0.00037	29.9	9.39	1.00	0.00939	103	99.98
NiP-C <sub>3</sub> N <sub>4</sub> (2.00g ZnO)	178	6.03	0.89	0.00259	7.50	47.4	0.88	0.04116	673	99.93

#### 4.5.2 Potentiodynamic polarization (Tafel curves)

Figure (46a and b, respectively) shows Tafel (potentiodynamic polarization) plots of the substrate and the as-plated as well as the corresponding heat-treated NiP, NiP-C<sub>3</sub>N<sub>4</sub> (undoped) and NiP-C<sub>3</sub>N<sub>4</sub>/ZnO (doped) nanocomposite coatings, with different concentrations of ZnO dopant, in 3.5 wt. % NaCl solution at room temperature. The HT is at 400 °C for 1h. Table (11) summarizes the various electrochemical parameters:  $i_{corr}$  (corrosion current density),  $E_{corr}$  (corrosion potential),  $b_c$  and  $b_a$  (cathodic and anodic Tafel slopes) that acquired using the Tafel extrapolation method, and the corrosion inhibition efficiency ( $I.E\%$ ) for the different as-plated and heat-treated coatings.

The inhibition efficiency ( $I.E\%$ ) was calculated using the equation below:

$$I.E. = \left[ \frac{i_{corr(CS)} - i_{corr(coat)}}{i_{corr(CS)}} \right] \times 100\%$$

Where  $i_{corr(CS)}$  and  $i_{corr(coat)}$  correspond to the corrosion current densities for the C-steel substrate and the coating, respectively.

As demonstrated from the Tafel data,  $E_{corr}$  of the substrate is (-500 mV), whereas  $E_{corr}$  for the NiP coating are considerably shifted to the noble direction. Introducing the C<sub>3</sub>N<sub>4</sub> nanocapsules to the NiP coating resulted in shifting the  $E_{corr}$  of the as-plated NiP-C<sub>3</sub>N<sub>4</sub> nanocomposite coating to even more positive direction (-247 mV) and have a corrosion current of (3.40 nAcm<sup>-2</sup>). However, compared to NiP-C<sub>3</sub>N<sub>4</sub>, the as-plated NiP-C<sub>3</sub>N<sub>4</sub>/ZnO coatings doped with 0.5 and 1.0 g ZnO are further shifted in the positive direction to  $E_{corr}$  of (-235 mV) and (-211 mV) and corresponding to  $i_{corr}$  of (2.30 nAcm<sup>-2</sup>) and (1.20 nAcm<sup>-2</sup>), respectively. Therefore, it is said that all potentiodynamic curves of the as-plated undoped or doped C<sub>3</sub>N<sub>4</sub> coatings compared to the as-plated C<sub>3</sub>N<sub>4</sub>-free coating' curve have shown a successful increase in their

corrosion potential associated by a decrease in their corrosion current densities, signifying an increase in the corrosion resistance of the NiP coating in the presence of undoped and doped C<sub>3</sub>N<sub>4</sub> nanocapsules. Furthermore, the corrosion current density of the doped C<sub>3</sub>N<sub>4</sub> nanocomposite coating decreased as the concentration of the ZnO dopant increased up to 1.0 g. A further increase in the ZnO dopant concentration in the C<sub>3</sub>N<sub>4</sub> nanocapsules led to increase the corrosion current density of the nanocomposite coating by about 7.7 times compared to that doped with 1 g ZnO dopant, as shown in Figure (46) and Table (11). Notably, the 1 g ZnO doped C<sub>3</sub>N<sub>4</sub> nanocomposite coatings had the highest corrosion protection efficiency, reaching 99.98%, as shown in Table (11).

The heat-treated NiP, undoped C<sub>3</sub>N<sub>4</sub> and doped C<sub>3</sub>N<sub>4</sub> nanocomposite coatings, with different concentrations of the ZnO dopant, showed the same trend as the corresponding as-plated ones, as shown in Figure (46b). However, their  $E_{\text{corr}}$  are further shifted to the positive direction and their corrosion current densities were smaller, as shown in Table (11). This indicates that the corrosion resistance of all coatings have significantly enhanced after heat treatment. Furthermore, the decrease in the corrosion rate values of the heat-treated composite coatings confirmed their superior protective ability. This is because of the more compactness of the heat-treated nanocomposite coatings with respect to the corresponding as-plated ones. The corrosion current density of the heat-treated NiP was about 77.3% lower than that of the corresponding as-plated one. Noticeably, the doped C<sub>3</sub>N<sub>4</sub> nanocomposite coating with 1 g ZnO dopant had the smallest corrosion current density (0.17 nAcm<sup>-2</sup>), displaying a protection efficiency of 99.99%.

Finally, it is worth mentioning that the results obtained from potentiodynamic polarization (Tafel analysis) are consistent with EIS outcomes.

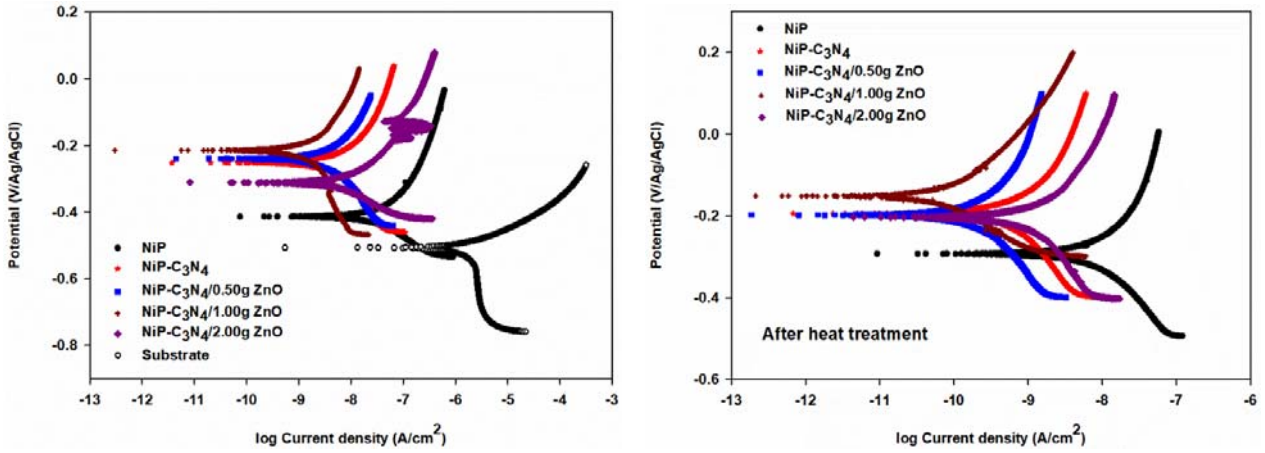


Figure 46. Tafel curves for a) the as-plated and b) the heat-treated NiP, NiP-C<sub>3</sub>N<sub>4</sub> (undoped) and NiP-C<sub>3</sub>N<sub>4</sub>/ZnO (doped) nanocomposite coatings, with different concentrations of ZnO dopant, in 3.5 wt% NaCl solution at room temperature. The heat treatment at 400 °C for 1h. The scan rate was 0.167 mV s<sup>-1</sup>. Tafel plot of the substrate is in a.

Table 11. Tafel fitting results of the different coatings before and after heat treatment.

Coating	$-E_{corr}$ (mV)	$i_{corr}$ (nAcm <sup>-2</sup> )	$b_a$ (V/decade)	$b_c$ (V/decade)	Corro. rate (mpy)	P.E. (%)
CS	500	6890	0.27	0.17	1.5500	----
NiP	411	56.0	0.67	0.21	0.0948	99.18
NiP-C <sub>3</sub> N <sub>4</sub>	247	3.40	0.59	0.34	0.0129	99.95
NiP-C <sub>3</sub> N <sub>4</sub> /0.5 g ZnO	235	2.30	0.32	0.45	0.0028	99.96
NiP-C <sub>3</sub> N <sub>4</sub> /1.0 g ZnO	211	1.20	0.45	0.18	0.0013	99.98
NiP-C <sub>3</sub> N <sub>4</sub> /2.0 g ZnO	309	9.20	0.29	0.14	0.0410	99.86
NiP (HT)	289	12.7	0.39	0.49	0.0232	99.81
NiP-C <sub>3</sub> N <sub>4</sub> (HT)	190	1.02	0.34	0.34	0.0033	99.98
NiP-C <sub>3</sub> N <sub>4</sub> /0.5 g ZnO (HT)	192	0.32	0.43	0.11	0.0023	99.99
NiP-C <sub>3</sub> N <sub>4</sub> /1.0 g ZnO (HT)	150	0.17	0.19	0.16	0.0001	99.99
NiP-C <sub>3</sub> N <sub>4</sub> /2.0 g ZnO (HT)	198	1.30	0.18	0.43	0.0201	99.98

## 4.6 Antibacterial Analysis

Bacterial growth and adhesion on the different surfaces stimulate the biocorrosion of the material, microbiological contamination, economic loss and healthcare problems. The material surface properties, the type of the bacteria, and the surrounding environment, governs the bacterial adhesion. Therefore, the *staphylococcus* (*S.aureus*) bacterial cell is utilized to evaluate the adhesion and antibacterial activity of the different composite coatings, which are NiP, NiP-C<sub>3</sub>N<sub>4</sub> (undoped) and NiP-C<sub>3</sub>N<sub>4</sub>/ZnO doped with different concentrations of ZnO (0.5, 1.0 and 2.0 g), before and after heat treatment at 400 °C for 1h, using the colony counting method. For comparison, the substrate (API X-120 carbon steel) is used as a control.

Figure (47a) depicts the plate' photographs of *S.aureus* colony forming units separated from the different coatings' surfaces. It is noticed that the as-plated NiP coating has lower number of *S.aureus* colonies compared to the substrate. The addition of undoped (C<sub>3</sub>N<sub>4</sub>) and doped C<sub>3</sub>N<sub>4</sub> nanocapsules (C<sub>3</sub>N<sub>4</sub>/ZnO) with different concentration of ZnO into the NiP matrix leads to a further decrease in the number of colonies for the NiP-C<sub>3</sub>N<sub>4</sub> and NiP-C<sub>3</sub>N<sub>4</sub>/ZnO, respectively, nanocomposite coatings compared to the C<sub>3</sub>N<sub>4</sub>-free coating. Moreover, it is investigated that the increase in the concentration of ZnO maximizes the number of the colonies, showing concentration dependence activity. Furthermore, upon heat treatment, the number of *S.aureus* colonies is minimized with all the different coatings.

Figure (47b) illustrates the colony forming units (CFU/ml) of *S.aureus* bacterial cells for the different coatings in addition to the substrate. It is observed that the CFU of the NiP coating is 30% lower than that of the substrate. Additionally, the NiP-C<sub>3</sub>N<sub>4</sub> and NiP-C<sub>3</sub>N<sub>4</sub>/0.5 g ZnO nanocomposites coatings offered an extra 38 % and 48.5 %, respectively, compared to the NiP coating.

respectively, decrease in the CFU compared to the NiP coating. The rising in the CFU of *S.aureus* bacterial cells is noticed with the increasing concentration of ZnO, where the NiP–C<sub>3</sub>N<sub>4</sub>/2.0g ZnO coating shows the highest CFU compared to the undoped and doped C<sub>3</sub>N<sub>4</sub> nanocomposite coating with 0.5 and 1.0 g ZnO. However, its CFU is still lower than that of C<sub>3</sub>N<sub>4</sub>-free coating by 25.7 %.

The CFU of the *S.aureus* bacterial cells of the different heat-treated coatings have the same increasing and decreasing trend with respect to their corresponding as-plated coatings. However, they show a remarkable reduction in their CFU values, reaching to 95.3% with the heat-treated NiP–C<sub>3</sub>N<sub>4</sub>/0.5g ZnO coating compared to its corresponding as-plated one. In addition, it is worth mentioning that there is a miniscule change in the CFU between the heat-treated NiP–C<sub>3</sub>N<sub>4</sub>/0.5g ZnO and NiP–C<sub>3</sub>N<sub>4</sub>/1.0g ZnO coatings, as shown in Figure (47b).

The NiP coating, in particular, plays a significant role in reducing bacterial growth as compared to the substrate. The antibacterial activity and/or strong NiP coating adsorption properties can be due to the reduction in the *S.aureus* bacterial cell attached to NiP coating. In general, the NiP coating's bactericidal efficiency is reported in many studies [29], [134], [135]. Furthermore, the NiP coating antibacterial activity can be due to the Ni<sup>2+</sup> dissolution from the NiP coating that enters the bacterial cell and inhibits its growth [136]. A similar mechanism is described for some metals' antibacterial activity, such as Ag and Zn [137], in which metal ions dissolution is essential for antibacterial activity. Dissolved metal ions that are physically or chemically bound to the cell wall can cross the cell membrane and aggregate intracellularly. Metal ions can bind cumulatively to bacterial proteins, making them non-functional leading to the death of the bacterial cell. Furthermore, emerged metal ions could constitute active radicals, resulting in the death of the cell due to its wall

breakup [138].

The substantial reduction in the CFU of the *S.aureus* bacterial cell in the case of as-plated NiP-C<sub>3</sub>N<sub>4</sub> and NiP-C<sub>3</sub>N<sub>4</sub>/ZnO nanocomposite coatings with different concentrations of ZnO, compared to the NiP coating, confirms the outstanding antibacterial activity of these coatings. This may be attributed to several reasons: a) When NiP composite coating is corroded, the C<sub>3</sub>N<sub>4</sub> nanoparticles become loose. The loose nanoparticles, due to their small size, larger surface area and more active catalytic sites, have a higher likelihood of passing through the bacterial cell wall. This penetration leads to changes in the cellular units of the bacteria, leading to its death [139], b) The antibacterial properties of the g-C<sub>3</sub>N<sub>4</sub> and ZnO, which are assessed and well documented as in refs [140]–[143], c) The semi-crystalline structure that characterized them, based on XRD results, which boosts the bacterial death, as in the literature [144], and d) The hydrophobicity properties of these composite coatings, as mentioned in the WCA section. Generally, it is known that the hydrophobic surfaces are desired for antibacterial applications [145]. Therefore, the as-plated NiP-C<sub>3</sub>N<sub>4</sub>/0.5g ZnO and NiP-C<sub>3</sub>N<sub>4</sub>/1.0g ZnO nanocomposite coatings have superior antibacterial properties. On the contrary, the *S.aureus* growth is enhanced on the as-plated NiP-C<sub>3</sub>N<sub>4</sub>/2.0g ZnO coating because of its less hydrophobicity, higher roughness, based on AFM measurements, and less compactness, based on SEM measurements. Furthermore, the less compactness of the NiP-C<sub>3</sub>N<sub>4</sub>/2.0g ZnO coating was also proven by the BET measurements, which show that the increasing concentration of ZnO dopant in the C<sub>3</sub>N<sub>4</sub> nanocapsules considerably increases its porosity and surface area, as previously mentioned in WCA section. Moreover, although the different heat-treated coatings show less hydrophobicity behavior and higher roughness, they display outstanding antibacterial behavior because of their smooth and high compactness



compared to their corresponding as-plated ones, in addition to their crystalline structures, which were obtained upon heat treatment at 400 °C.

Finally, it is clear that the superior antibacterial properties of the NiP-C<sub>3</sub>N<sub>4</sub>/ZnO nanocomposite coating make it ready to apply in many industries to enhance the anticorrosion performance of several coated materials. In addition, because of the excellent bacterial activity of the NiP coating toward *S.aureus* and other types of bacteria, it is of great importance to conduct more experiments and investigations on this coating. For example, some aspects to be further studied include the relationship of the surface chemistry, roughness, grain size and microstructure of this antibacterial coating and its composites.

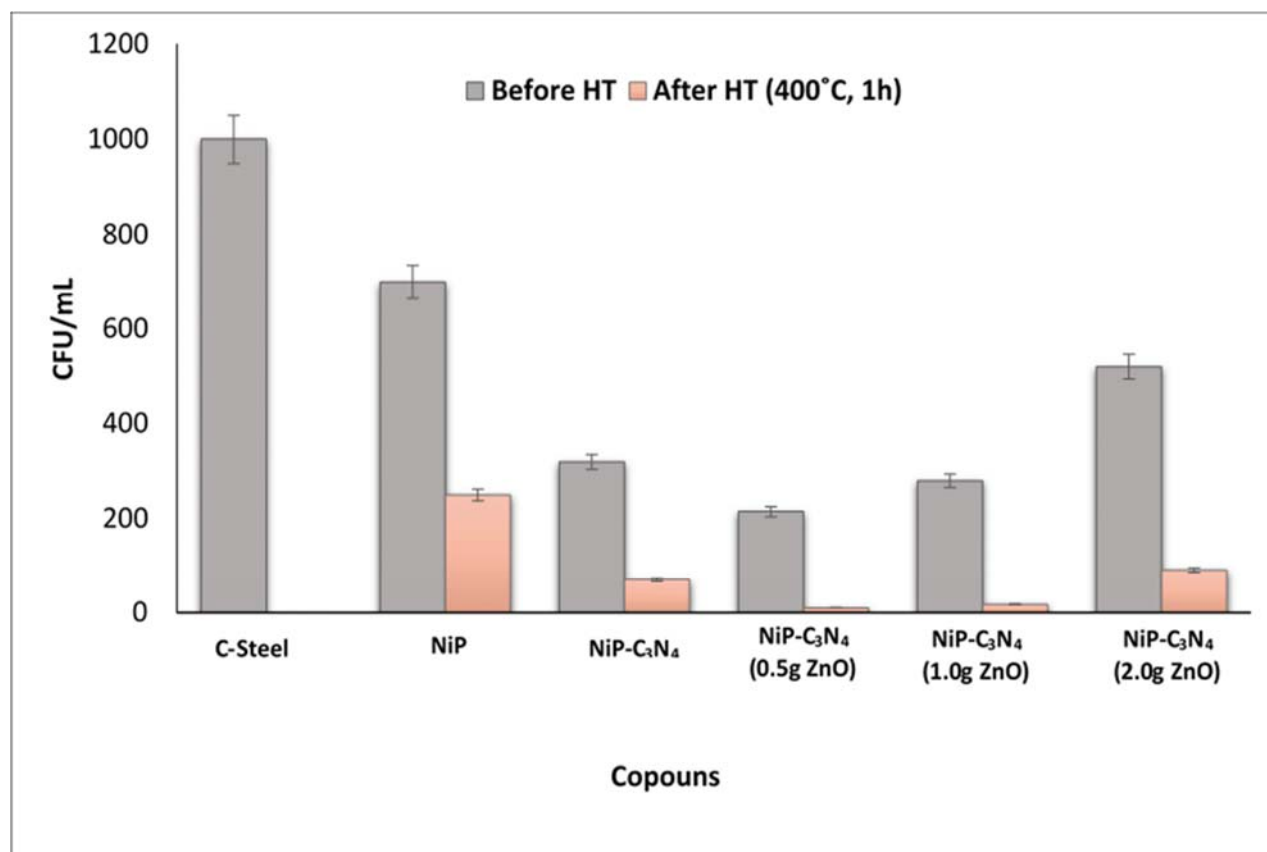
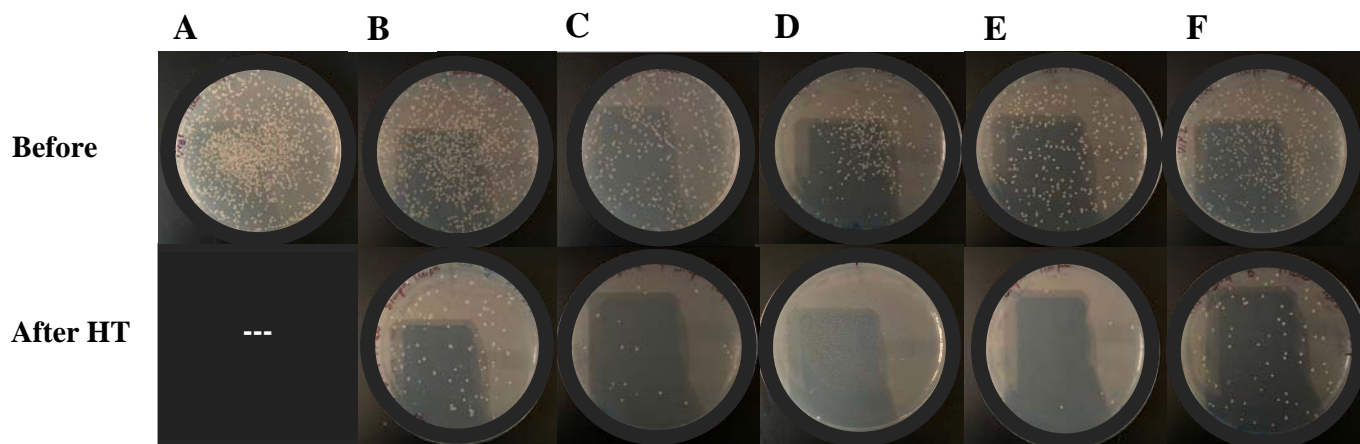


Figure 47. Antibacterial activity of the different coupons, (a) Photographs of *S.aureus* exposed to substrate (A), NiP (B) and NiP-C<sub>3</sub>N<sub>4</sub> undoped (C), NiP-C<sub>3</sub>N<sub>4</sub> doped with 0.5 (D), 1.0 (E) and 2.0 g (F) ZnO nanocomposite coatings. (b) CFU of *S.aureus* bacterial cells

## CHAPTER 5: CONCLUSIONS AND FUTURE WORK

### Conclusions

It can be concluded that  $C_3N_4/ZnO$  nanocapsules with different concentrations (0.50, 1.00 and 2.00 g) of doped ZnO were successfully synthesized and incorporated in the NiP metallic coating using electroless deposition technique. The prepared coatings were heat treated (HT) at 400°C for 1h, and the influence of undoped and doped  $C_3N_4$  with ZnO on the NiP coating, before and after HT was investigated using various characterization techniques that assessed their structure, elemental composition, morphology, thickness, roughness, wettability, hardness, and antibacterial and corrosion protection properties.

XRD results verified that the incorporation of undoped or ZnO doped  $C_3N_4/ZnO$  nanocapsules in the NiP coating changes its structure from amorphous to crystalline-amorphous or semi-amorphous state, which confirmed the high and medium P content in those coatings, in line with the EDX results. Furthermore, the full width at half-maximum (FWHM) values for the different nanocomposite coatings, showed that the refinement of the NiP nodules and the boosting of the crystalline phase formation is achieved in the occurrence of undoped and doped  $C_3N_4$  in the NiP matrix. After HT, NiP was crystallized and  $Ni_3P$  particles, as well as, crystalline Ni phase were formed. Additionally, the peaks of HT - undoped and doped NiP- $C_3N_4$  nanocomposite coatings matched with those obtained for the HT- NiP coating with a minor change in the intensity of the resulted peaks, revealing the effect of the incorporation of undoped or doped  $C_3N_4$  nanocapsules, which are well dispersed in the NiP matrix.

A cauliflower-like structure characterized by a feature of spherical nodules was observed in the SEM image of NiP coating. The incorporation of  $C_3N_4$  nanocapsules into the NiP matrix did not change the cauliflower shape of the NiP coating, yet, it had

considerable effect on the nodules' size and arrangement as the surface became less smooth, and the size of the nodules significantly decreased, while their numbers increased. The surface morphology of the nanocomposite coatings was remarkably affected by doping the  $C_3N_4$  nanocapsules with ZnO at different concentrations. The spherical nodules became more homogeneous and compact, namely in NiP-  $C_3N_4/1.0$  g ZnO. However, increasing the concentration of doped ZnO in the  $C_3N_4$  nanocapsules up to 2g caused the agglomeration of the nanocapsules that was induced by the increased porosity and distorted morphology of the nanocapsules by doping with 2g ZnO, hence the uniformity and compactness of the coating was greatly reduced. After heat treatment, the surface homogeneity and compactness was generally enhanced for all of the coatings, namely for that of the HT-  $C_3N_4/1.00$ g ZnO, which was mostly related to the formation of new phases, as illustrated in XRD analysis.

The EDX spectra confirmed the presence of  $C_3N_4$  in the NiP coating, as peaks of Ni, P, C, and N have appeared. The P content decreased by about 50% upon the incorporation of  $C_3N_4$  nanocapsules, revealing that the structure of as-plated coatings changed from amorphous to semi-crystalline, which is consistent with the XRD results. Doping the nanocapsules with ZnO mainly revealed an increase in the O content in the composite coatings, which might be related to the increased porosity and surface area of  $C_3N_4$  nanocapsules that were incorporated in the coating. Zinc (Zn) element, which is related to the doped ZnO in the nanocapsules, was hardly detected by EDX, which emerged only at high concentrations, i.e. 1.00 and 2.00g, as the ZnO nanoparticles are embedded within the carbon nitride nanostructures. After HT, the P content slightly decreased in all the EDX spectra of the HT coatings, due to the formation of new phases, such as  $Ni_3P$ , as well as, the improved crystallinity of the prepared coatings, confirming the XRD results.

The cross-section SEM analysis and EDX mapping confirmed the uniformity of all the coatings, with no cracks or defects at the substrate/coating interface, revealing good coatings adhesion. Furthermore, the TEM analysis confirmed the uniform distribution of undoped and ZnO-doped C<sub>3</sub>N<sub>4</sub> nanocapsules in all the different coatings.

The Vicker's microhardness of as-plated and heat treated nanocomposite coatings was significantly improved after the incorporation of undoped C<sub>3</sub>N<sub>4</sub> nanocapsules. After doping the C<sub>3</sub>N<sub>4</sub> nanocapsules with ZnO further improvement was done, namely with 0.5g ZnO doped C<sub>3</sub>N<sub>4</sub> nanocapsules, where the NiP-C<sub>3</sub>N<sub>4</sub>/0.5g ZnO composite coating showed the maximum microhardness of 680 and 1,330 HV<sub>200</sub>, before and after heat treatment, respectively. Generally, all the coatings showed improved microhardness upon HT, following the same trend before HT.

Electrochemical impedance spectroscopy (EIS) and potentiodynamic polarization (PP) outcomes showed enhanced corrosion resistance after heat treatment of undoped and doped NiP- C<sub>3</sub>N<sub>4</sub> coatings, which indicated higher corrosion resistance than the corresponding as-plated ones. The highest corrosion resistance was achieved on the as-plated and heat treated NiP- C<sub>3</sub>N<sub>4</sub> coatings incorporated with 1.00 g ZnO doped C<sub>3</sub>N<sub>4</sub> nanocapsules. Generally, the C<sub>3</sub>N<sub>4</sub>/ZnO nanocapsules prevented the localized corrosion and enhanced the corrosion resistance of the nanocomposite coatings by filling the micro defects and pores of the NiP matrix.

Finally, the antibacterial analysis showed an improved antibacterial behavior of the as-plated and heat-treated coatings, with superior antibacterial properties after heat treatment, namely for NiP-C<sub>3</sub>N<sub>4</sub>/0.5g ZnO nanocomposite coating.

The overall results revealed that the newly synthesized C<sub>3</sub>N<sub>4</sub>/ZnO nanocapsules successfully improved the mechanical, corrosion resistance, and antibacterial behavior of the electroless NiP coating. The greatest mechanical and corrosion resistance

enhancements were achieved for the NiP-C<sub>3</sub>N<sub>4</sub>/0.5g ZnO and NiP-C<sub>3</sub>N<sub>4</sub>/1.0g ZnO, respectively. Whereas, the best antibacterial behavior was attained by the NiP-C<sub>3</sub>N<sub>4</sub>/0.5g ZnO nanocomposite coating. Therefore, it is suggested that NiP-C<sub>3</sub>N<sub>4</sub>/0.5g ZnO can be the best nanocomposite coating, which can be potentially utilized as a reinforcement nanomaterial in improving the mechanical and anticorrosion performance of NiP metallic coatings in chloride media, together with providing superior antibacterial properties.

### Future Work

The superior properties of carbon nitride (C<sub>3</sub>N<sub>4</sub>) nanomaterials, open the door for many future applications, namely in anticorrosive coatings. Despite the fast growing research area in electroless NiP coatings, the use of different shapes of C<sub>3</sub>N<sub>4</sub> nanomaterials, such as, nanofibers, nanorods, nanoflowers, etc., as a reinforcing material in the electroless NiP coating has not been investigated yet. Any further studies on such coating systems will be promising and can result in novel outcomes.

Further investigations on the wear resistance of the newly synthesized C<sub>3</sub>N<sub>4</sub>/ZnO nanocapsules can be a great area of future research. Additionally, it is recommended to evaluate the corrosion resistance in different aggressive media, such as acidic environments, which will open the door for further applications.

Additionally, seeking to produce environmentally friendly coatings, assessment of the environmental impact of the newly synthesized NiP-C<sub>3</sub>N<sub>4</sub> nanocomposite coatings can be a new area of future research.

## REFERENCES

- [1] M. G. Hosseini, M. Abdolmaleki, S. Ashrafpoor, and R. Najjar, "Deposition and corrosion resistance of electroless Ni-PCTFE-P nanocomposite coatings," *Surf. Coatings Technol.*, vol. 206, no. 22, pp. 4546–4552, 2012, doi: 10.1016/j.surfcoat.2012.04.083.
- [2] K. Shahzad *et al.*, "Corrosion and heat treatment study of electroless nip-ti nanocomposite coatings deposited on hsla steel," *Nanomaterials*, vol. 10, no. 10, pp. 1–19, 2020, doi: 10.3390/nano10101932.
- [3] R. Agarwala, V. Agarwala, and R. Sharma, "Electroless Ni-P based nanocoating technology - A review," *Synth. React. Inorganic, Met. Nano-Metal Chem.*, vol. 36, no. 6, pp. 493–515, 2006, doi: 10.1080/15533170600596030.
- [4] D. Dong, X. H. Chen, W. T. Xiao, G. B. Yang, and P. Y. Zhang, "Preparation and properties of electroless Ni-P-SiO<sub>2</sub> composite coatings," *Appl. Surf. Sci.*, vol. 255, no. 15, pp. 7051–7055, 2009, doi: 10.1016/j.apsusc.2009.03.039.
- [5] C. Y. Huang, W. W. Mo, and M. L. Roan, "Studies on the influence of double-layer electroless metal deposition on the electromagnetic interference shielding effectiveness of carbon fiber/ABS composites," *Surf. Coatings Technol.*, vol. 184, no. 2–3, pp. 163–169, 2004, doi: 10.1016/j.surfcoat.2003.11.010.
- [6] H. Luo, M. Leitch, Y. Behnamian, Y. Ma, H. Zeng, and J. L. Luo, "Development of electroless Ni-P/nano-WC composite coatings and investigation on its properties," *Surf. Coatings Technol.*, vol. 277, pp. 99–106, 2015, doi: 10.1016/j.surfcoat.2015.07.011.
- [7] A. S. Hamdy, M. A. Shoeib, H. Hady, and O. F. Abdel Salam, "Corrosion behavior of electroless Ni-P alloy coatings containing tungsten or nano-scattered alumina composite in 3.5% NaCl solution," *Surf. Coatings Technol.*, vol. 202,

- no. 1, pp. 162–171, 2007, doi: 10.1016/j.surfcoat.2007.05.030.
- [8] M. C. Raval and C. S. Solanki, “Review of Ni-Cu Based Front Side Metallization for c-Si Solar Cells,” *J. Sol. Energy*, vol. 2013, no. September, pp. 1–20, 2013, doi: 10.1155/2013/183812.
- [9] A. A. Setiamy and E. Deliani,” vol. 2, pp. 5–10, 2019.
- [10] E. M. Fayyad *et al.*, “Synthesis, characterization, and application of novel Ni-P-carbon nitride nanocomposites,” *Coatings*, vol. 8, no. 1, pp. 1–13, 2018, doi: 10.3390/coatings8010037.
- [11] T. S. Miller, A. B. Jorge, T. M. Suter, A. Sella, F. Corà, and P. F. McMillan, “Carbon nitrides: Synthesis and characterization of a new class of functional materials,” *Phys. Chem. Chem. Phys.*, vol. 19, no. 24, pp. 15613–15638, 2017, doi: 10.1039/c7cp02711g.
- [12] Y. Zhu, T. Ren, and Z. Yuan, “Mesoporous phosphorus-doped g-C<sub>3</sub>N<sub>4</sub> nanostructured flowers with superior photocatalytic hydrogen evolution performance,” pp. 1–26.
- [13] Y. Zheng, L. Lin, X. Ye, F. Guo, and X. Wang, “Angewandte Helical Graphitic Carbon Nitrides with Photocatalytic and Optical Activities \*\*,” vol. 201407319, no. 20133514110003, pp. 11926–11930, 2014, doi: 10.1002/anie.201407319.
- [14] J. Liu, J. Huang, H. Zhou, and M. Antonietti, “Uniform Graphitic Carbon Nitride Nanorod for Efficient Photocatalytic Hydrogen Evolution and Sustained Photoenzymatic Catalysis,” 2014.
- [15] X. Bai, L. Wang, R. Zong, and Y. Zhu, “Photocatalytic Activity Enhanced via g-C<sub>3</sub>N<sub>4</sub> Nanoplates to Nanorods,” 2013.
- [16] J. Zhang, M. Zhang, C. Yang, and X. Wang, “Nanospherical Carbon Nitride Frameworks with Sharp Edges Accelerating Charge Collection and Separation



- at a Soft Photocatalytic Interface,” pp. 4121–4126, 2014, doi: 10.1002/adma.201400573.
- [17] E. M. Fayyad, A. M. Abdullah, A. M. A. Mohamed, G. Jarjoura, Z. Farhat, and M. K. Hassan, “Effect of electroless bath composition on the mechanical, chemical, and electrochemical properties of new NiP–C 3 N 4 nanocomposite coatings,” *Surf. Coatings Technol.*, vol. 362, no. November 2018, pp. 239–251, 2019, doi: 10.1016/j.surfcoat.2019.01.087.
- [18] A. M. Kumar, A. Khan, M. Yusuf, R. K. Suleiman, and J. Jose, “Hierarchical graphitic carbon nitride-ZnO nanocomposite: Viable reinforcement for the improved corrosion resistant behavior of organic coatings,” vol. 251, no. April, 2020.
- [19] Badea G E, Caraban A, Sebesan M, Cret P, and Setel A, “Polarisation Measurements Used for Corrosion Rates Determination,” *J. Sustainable Energy*, vol. 1, no. 1, pp. 1–4, 2010.
- [20] J. I. I. Laco, F. C. Villota, and F. L. Mestres, “Corrosion protection of carbon steel with thermoplastic coatings and alkyd resins containing polyaniline as conductive polymer,” *Prog. Org. Coatings*, vol. 52, no. 2, pp. 151–160, Feb. 2005, doi: 10.1016/J.PORGCOAT.2004.10.005.
- [21] A. B. Radwan, A. M. A. Mohamed, A. M. Abdullah, and M. A. Al-Maadeed, “Corrosion protection of electrospun PVDF-ZnO superhydrophobic coating,” *Surf. Coatings Technol.*, vol. 289, pp. 136–143, 2016, doi: 10.1016/j.surfcoat.2015.12.087.
- [22] Y. Wang *et al.*, “Duplex Ni-P-ZrO<sub>2</sub>/Ni-P electroless coating on stainless steel,” *J. Alloys Compd.*, vol. 630, pp. 189–194, 2015, doi: 10.1016/j.jallcom.2015.01.064.

- [23] B. Fotovvati, N. Namdari, and A. Dehghanhadikolaei, "On Coating Techniques for Surface Protection: A Review," *J. Manuf. Mater. Process.*, vol. 3, no. 1, p. 28, 2019, doi: 10.3390/jmmp3010028.
- [24] C. Wang, Z. Farhat, G. Jarjoura, M. K. Hassan, and A. M. Abdullah, "Indentation and bending behavior of electroless Ni-P-Ti composite coatings on pipeline steel," *Surf. Coatings Technol.*, vol. 334, no. October 2017, pp. 243–252, 2018, doi: 10.1016/j.surfcoat.2017.10.074.
- [25] X.-H. Yang, W.-L. Zhu, Z. Lin, and J.-J. Huo, "Aerodynamic evaluation of an internal epoxy coating in nature gas pipeline," *Prog. Org. Coatings*, vol. 54, no. 1, pp. 73–77, Sep. 2005, doi: 10.1016/J.PORGCOAT.2005.04.001.
- [26] G. R. Howell and Y. F. Cheng, "Characterization of high performance composite coating for the northern pipeline application," *Prog. Org. Coatings*, vol. 60, no. 2, pp. 148–152, Sep. 2007, doi: 10.1016/J.PORGCOAT.2007.07.013.
- [27] Y. Y. Liu *et al.*, "Synthesis and tribological behavior of electroless Ni – P – WC nanocomposite coatings," vol. 201, pp. 7246–7251, 2007, doi: 10.1016/j.surfcoat.2007.01.035.
- [28] Fayyad, Eman M., Hassan K. Mohammad, Rasool Kashif, Mahmoud Khaled A., Mohamed Adel M.A., Jajoura George, Farhat Zoheir, Abdullah Aboubakr M., "Novel electroless deposited corrosion-resistant and anti-bacterial NiP-TiNi nanocomposite coatings," *Surf. Coatings Technol. - SURF COAT TECH*, vol. 4, no. 1, pp. 75–84, 2019, doi: .1037//0033-2909.I26.1.78.
- [29] S. Chenghuo and H. Hong, "Effect of diamond nanoparticles in electroless Ni-P-ND coatings on bacterial anti-adhesive behavior," *Proc. - 2017 Int. Conf. Smart Grid Electr. Autom. ICSGEA 2017*, vol. 2017-January, pp. 68–72, 2017, doi: 10.1109/ICSGEA.2017.130.

- [30] S. A. Fadl-allah, A. A. Montaser, and S. M. F. Gad El-Rab, "Biocorrosion control of electroless Ni-Zn-P coating based on carbon steel by the *Pseudomonas aeruginosa* Biofilm," *Int. J. Electrochem. Sci.*, vol. 11, no. 7, pp. 5490–5506, 2016, doi: 10.20964/2016.07.96.
- [31] A. Manuscript, "Catalysis Science & Technology," 2016, doi: 10.1039/C6CY01195K.
- [32] J. D. Bray, A. Rodriguez-Marek, and J. L. Gillie, "Design ground motions near active faults," *Bull. New Zeal. Soc. Earthq. Eng.*, vol. 42, no. 1, pp. 1–8, 2009, doi: 10.5459/bnzsee.42.1.1-8.
- [33] C. I. Ossai, "Advances in Asset Management Techniques: An Overview of Corrosion Mechanisms and Mitigation Strategies for Oil and Gas Pipelines," *ISRN Corros.*, vol. 2012, pp. 1–10, 2012, doi: 10.5402/2012/570143.
- [34] P. A. Sørensen, S. Kiil, K. Dam-Johansen, and C. E. Weinell, "Anticorrosive coatings: A review," *J. Coatings Technol. Res.*, vol. 6, no. 2, pp. 135–176, 2009, doi: 10.1007/s11998-008-9144-2.
- [35] A. Husain, O. Al-Shamah, and A. Abduljaleel, "Investigation of marine environmental related deterioration of coal tar epoxy paint on tubular steel pilings," *Desalination*, vol. 166, pp. 295–304, Aug. 2004, doi: 10.1016/J.DESAL.2004.06.084.
- [36] P. C. Okonkwo *et al.*, "Erosion behavior of API X120 steel: Effect of particle speed and impact angle," *Coatings*, vol. 8, no. 10, 2018, doi: 10.3390/COATINGS8100343.
- [37] K. Hari Krishnan, S. John, K. N. Srinivasan, J. Praveen, M. Ganesan, and P. M. Kavimani, "An overall aspect of electroless Ni-P depositions - A review article," *Metall. Mater. Trans. A Phys. Metall. Mater. Sci.*, vol. 37, no. 6, pp. 1917–1926,

- 2006, doi: 10.1007/s11661-006-0134-7.
- [38] G. Mallory, “The fundamental aspects of electroless nickel plating,” *Fundam. Asp. electroless nickel Plat.*, pp. 1–56, 1990, doi: 10.1007/s004420050568.
- [39] A. B. and G. E. Riddell, *Proc. Am. Electropl.* 1946.
- [40] A. Wurtz, *Comp. Rendus Acad. Sci.* 1844.
- [41] R. Weil and K. Parker, “Electroless Plating - Fundamentals and Applications (Chapter 4 The Properties of Electroless Nickel),” pp. 111–137, 1990.
- [42] E. M. Fayyad, A. M. Abdullah, M. K. Hassan, A. M. Mohamed, G. Jarjoura, and Z. Farhat, “Recent advances in electroless-plated Ni-P and its composites for erosion and corrosion applications: a review,” *Emergent Mater.*, vol. 1, no. 1–2, pp. 3–24, 2018, doi: 10.1007/s42247-018-0010-4.
- [43] F. B. Mainier, M. P. C. Fonseca, S. S. M. Tavares, and J. M. Pardal, “Quality of Electroless Ni-P (Nickel-Phosphorus) Coatings Applied in Oil Production Equipment with Salinity,” *J. Mater. Sci. Chem. Eng.*, vol. 01, no. 06, pp. 1–8, 2013, doi: 10.4236/msce.2013.16001.
- [44] M. Hajizamani, A. Alizadeh, N. Ehsani, and M. Mirjani, “A study on the effect of reducing agent content on the thickness of electroless Ni<sub>3</sub>P deposits on B<sub>4</sub>C nanoparticles,” *Rev. Met.*, vol. 110, no. 2, pp. 147–152, 2013.
- [45] R. Severens, J. Bastiaanssen, and D. Schram, “High-quality a-Si:H grown at high rate using an expanding thermal plasma,” *Surf. Coatings Technol.*, vol. 97, no. 1, pp. 719–722, 1997, doi: 10.1016/S0257-8972.
- [46] M. Yan, H. G. Ying, and T. Y. Ma, “Improved microhardness and wear resistance of the as-deposited electroless Ni–P coating,” *Surf. Coatings Technol.*, vol. 202, no. 24, pp. 5909–5913, 2008, doi: <https://doi.org/10.1016/j.surfcoat.2008.06.180>.

- [47] K. G. Keong and W. Sha, “Crystallisation and Phase Transformation Behaviour of Electroless Nickel-Phosphorus Deposits and Their Engineering Properties,” *Surf. Eng.*, vol. 18, no. 5, pp. 329–343, Oct. 2002, doi: 10.1179/026708402225010010.
- [48] G. Zhao, Y. Zou, H. Zhang, and Z. Zou, “Effect of low-temperature annealing on the properties of Ni-P amorphous alloys deposited via electroless plating,” *Arch. Metall. Mater.*, vol. 60, no. 2A, pp. 865–869, 2015, doi: 10.1515/amm-2015-0220.
- [49] E. Broszeit, “Mechanical, thermal and tribological properties of electro- and chemodeposited composite coatings,” *Thin Solid Films*, vol. 95, no. 2, pp. 133–142, Sep. 1982, doi: 10.1016/0040-6090(82)90235-8.
- [50] I. J. D. Nava, C.E. Dávalos, A. Martínez-Hernández, F. Manríquez, Y. Meas, R. Ortega-Borges, J. Pérez-Bueno, G. Trejo, *Electrodeposition of composite materials*. 2013.
- [51] W. Zhang, Z. hong Zhang, H. xi Guo, Y. Xu, and X. jun Fan, “Corrosion resistance properties and preparation of  $\alpha$ -C<sub>3</sub>N<sub>4</sub> thin films,” *Wuhan Univ. J. Nat. Sci.*, 1999.
- [52] R. Taheri, “Electroless depostion of nickel,” *Mod. Electroplat.*, vol. 1, no. 1, p. 262, 2003, doi: 10.1149/1.2425993.
- [53] M. Czagany and P. Baumli, “EFFECT of ph on the characteristics of electroless Ni-P coatings,” *J. Min. Metall. Sect. B Metall.*, vol. 53, no. 3, pp. 327–332, 2017, doi: 10.2298/JMMB170530020C.
- [54] Z. Abdel Hamid and M. T. Elkhair, “Development of electroless nickel–phosphorous composite deposits for wear resistance of 6061 Aluminum alloy,” *Mater. Lett.*, vol. 57, pp. 720–726, Dec. 2002, doi: 10.1016/S0167-

577X(02)00860-1.

- [55] Y. Huang, X. T. Zeng, I. Annergren, and F. M. Liu, "Development of electroless NiP–PTFE–SiC composite coating," *Surf. Coatings Technol.*, vol. 167, pp. 207–211, Apr. 2003, doi: 10.1016/S0257-8972(02)00899-X.
- [56] M. Buchtík, P. Kosár, J. Wasserbauer, and M. Zmrzlý, "Electroless deposition of Ni-P/SiO<sub>2</sub> composite coating," *Acta Univ. Agric. Silvic. Mendelianae Brun.*, vol. 64, no. 5, pp. 1459–1464, 2016, doi: 10.11118/actaun201664051459.
- [57] B. Abbasipour, S. M. Monirvaghefi, and B. Niroumand, "Electroless Ni-P-CNT composite coating on aluminum powder," *Met. Mater. Int.*, vol. 18, no. 6, pp. 1015–1021, 2012, doi: 10.1007/s12540-012-6014-3.
- [58] R. C. Agarwala, "Electroless Ni-P-ferrite composite coatings for microwave applications," *Pramana - J. Phys.*, vol. 65, no. 5, pp. 959–965, 2005, doi: 10.1007/BF02704097.
- [59] J. Sudagar, J. Lian, and W. Sha, "Electroless nickel, alloy, composite and nano coatings – A critical review," *J. Alloys Compd.*, vol. 571, pp. 183–204, 2013, doi: <https://doi.org/10.1016/j.jallcom.2013.03.107>.
- [60] S. M. A. Shibli, B. Jabeera, and R. I. Anupama, "Incorporation of nano zinc oxide for improvement of electroless nickel plating," *Appl. Surf. Sci.*, vol. 253, no. 3, pp. 1644–1648, 2006, doi: 10.1016/j.apsusc.2006.02.063.
- [61] V. Krishnakumar and R. Elansezhian, "Wear and corrosion behavior of electroless Ni-P-TiO<sub>2</sub>-Al<sub>2</sub>O<sub>3</sub>nanocomposite coatings on magnesium AZ91D alloy," *IOP Conf. Ser. Mater. Sci. Eng.*, vol. 912, no. 5, 2020, doi: 10.1088/1757-899X/912/5/052020.
- [62] Y. Z. Zhang and M. Yao, "Studies of Electroless Nickel Deposits with Low Phosphorus Content," *Trans. IMF*, vol. 77, no. 2, pp. 78–83, Jan. 1999, doi:

10.1080/00202967.1999.11871252.

- [63] Y. H. Cheng, Y. Zou, L. Cheng, and W. Liu, "Effect of the microstructure on the properties of Ni–P deposits on heat transfer surface," *Surf. Coatings Technol.*, vol. 203, pp. 1559–1564, Mar. 2009, doi: 10.1016/j.surfcoat.2008.10.039.
- [64] A. Zarebidaki and S.-R. Allahkaram, "Porosity measurement of electroless Ni–P coatings reinforced by CNT or SiC particles," *Surf. Eng.*, vol. 28, no. 6, pp. 400–405, Jul. 2012, doi: 10.1179/1743294411Y.0000000087.
- [65] A. Mukhopadhyay, T. K. Barman, and P. Sahoo, "Effect of Heat Treatment on the Characteristics of Electroless Ni-B, Ni-B-W and Ni-B-Mo Coatings," *Mater. Today Proc.*, vol. 5, no. 2, pp. 3306–3315, Jan. 2018, doi: 10.1016/J.MATPR.2017.11.573.
- [66] K. G. Keong, W. Sha, and S. Malinov, "Hardness evolution of electroless nickel–phosphorus deposits with thermal processing," *Surf. Coatings Technol. - SURF COAT TECH*, vol. 168, pp. 263–274, May 2003, doi: 10.1016/S0257-8972(03)00209-3.
- [67] C. A. Loto, "Electroless Nickel Plating – A Review," *Silicon*, vol. 8, no. 2, pp. 177–186, 2016, doi: 10.1007/s12633-015-9367-7.
- [68] A. Pertuz, J. A. Chitty, H. Hintermann, and E. S. Puchi, "Corrosion-fatigue behavior of an annealed AISI 1045 carbon steel coated with electroless nickel–phosphorus," *J. Mater. Eng. Perform.*, vol. 8, no. 4, pp. 424–428, 1999, doi: 10.1361/105994999770346710.
- [69] J. LIEBIG, "Über einige Stickstoff - Verbindungen," *Ann. der Pharm.*, vol. 10, no. 1, pp. 1–47, Jan. 1834, doi: <https://doi.org/10.1002/jlac.18340100102>.
- [70] B. V. Lotsch and W. Schnick, "From triazines to heptazines: Novel nonmetal tricyanomelaminates as precursors for graphitic carbon nitride materials," *Chem.*

- Mater.*, vol. 18, no. 7, pp. 1891–1900, 2006, doi: 10.1021/cm052342f.
- [71] A. M. Y. Y. LIU and M. L. COHEN, “Prediction of New Low Compressibility Solids,” *Science (80-. )*, vol. 245, no. 4920, pp. 841 LP – 842, Aug. 1989, doi: 10.1126/science.245.4920.841.
- [72] J. Liu, H. Wang, and M. Antonietti, “Graphitic carbon nitride ‘reloaded’: Emerging applications beyond (photo)catalysis,” *Chem. Soc. Rev.*, vol. 45, no. 8, pp. 2308–2326, 2016, doi: 10.1039/c5cs00767d.
- [73] S. A. Ladva *et al.*, “Nanoscale, conformal films of graphitic carbon nitride deposited at room temperature: A method for construction of heterojunction devices,” *Nanoscale*, vol. 9, no. 43, pp. 16586–16590, 2017, doi: 10.1039/c7nr06489f.
- [74] Y. Wang, X. Wang, and M. Antonietti, “Polymeric graphitic carbon nitride as a heterogeneous organocatalyst: From photochemistry to multipurpose catalysis to sustainable chemistry,” *Angew. Chemie - Int. Ed.*, vol. 51, no. 1, pp. 68–89, 2012, doi: 10.1002/anie.201101182.
- [75] G. Mamba and A. K. Mishra, “Graphitic carbon nitride (g-C<sub>3</sub>N<sub>4</sub>) nanocomposites: A new and exciting generation of visible light driven photocatalysts for environmental pollution remediation,” *Appl. Catal. B Environ.*, vol. 198, pp. 347–377, 2016, doi: 10.1016/j.apcatb.2016.05.052.
- [76] G. Dong, Y. Zhang, Q. Pan, and J. Qiu, “A fantastic graphitic carbon nitride (g-C<sub>3</sub>N<sub>4</sub>) material: Electronic structure, photocatalytic and photoelectronic properties,” *J. Photochem. Photobiol. C Photochem. Rev.*, vol. 20, no. 1, pp. 33–50, 2014, doi: 10.1016/j.jphotochemrev.2014.04.002.
- [77] I. Papailias *et al.*, “Chemical vs thermal exfoliation of g-C<sub>3</sub>N<sub>4</sub> for NO<sub>x</sub> removal under visible light irradiation,” *Appl. Catal. B Environ.*, vol. 239, no. May, pp.



- 16–26, 2018, doi: 10.1016/j.apcatb.2018.07.078.
- [78] G. Lei *et al.*, “Exfoliation of Graphitic Carbon Nitride for Enhanced Oxidative Desulfurization: A Facile and General Strategy,” *ACS Sustain. Chem. Eng.*, vol. 7, no. 5, pp. 4941–4950, 2019, doi: 10.1021/acssuschemeng.8b05553.
- [79] S. Zuo *et al.*, “Polyaniline/g-C<sub>3</sub>N<sub>4</sub> composites as novel media for anticorrosion coatings,” *J. Coatings Technol. Res.*, vol. 14, no. 6, pp. 1307–1314, 2017, doi: 10.1007/s11998-017-9916-7.
- [80] J. Xu, L. Zhang, R. Shi, and Y. Zhu, “Chemical exfoliation of graphitic carbon nitride for efficient heterogeneous photocatalysis,” *J. Mater. Chem. A*, vol. 1, no. 46, pp. 14766–14772, 2013, doi: 10.1039/c3ta13188b.
- [81] H. Zheng, Y. Shao, Y. Wang, G. Meng, and B. Liu, “Reinforcing the corrosion protection property of epoxy coating by using graphene oxide–poly(urea–formaldehyde) composites,” *Corros. Sci.*, vol. 123, pp. 267–277, 2017, doi: <https://doi.org/10.1016/j.corsci.2017.04.019>.
- [82] N. Wang, H. Gao, J. Zhang, L. Li, X. Fan, and X. Diao, “Anticorrosive waterborne epoxy (EP) coatings based on sodium tripolyphosphate-pillared layered double hydroxides (STPP-LDHs),” *Prog. Org. Coatings*, vol. 135, pp. 74–81, 2019, doi: <https://doi.org/10.1016/j.porgcoat.2019.04.055>.
- [83] N. Wang, W. Fu, J. Zhang, X. Li, and Q. Fang, “Corrosion performance of waterborne epoxy coatings containing polyethylenimine treated mesoporous-TiO<sub>2</sub> nanoparticles on mild steel,” *Prog. Org. Coatings*, vol. 89, pp. 114–122, 2015, doi: <https://doi.org/10.1016/j.porgcoat.2015.07.009>.
- [84] H. Yan, J. Li, M. Zhang, Y. Zhao, Y. Feng, and Y. Zhang, “Enhanced corrosion resistance and adhesion of epoxy coating by two-dimensional graphite-like g-C<sub>3</sub>N<sub>4</sub> nanosheets,” *J. Colloid Interface Sci.*, vol. 579, pp. 152–161, 2020, doi:

10.1016/j.jcis.2020.06.027.

- [85] A. M. Kumar, M. Y. Khan, R. K. Suleiman, A. Khan, and H. Dafalla, “Promising graphitic carbon nitride/MoO<sub>x</sub> nanocomposites: For surface protective performance of AA2024 alloys in marine environment,” *Surf. Coatings Technol.*, vol. 374, no. February, pp. 579–590, 2019, doi: 10.1016/j.surfcoat.2019.06.004.
- [86] J. H. Xu, S. Ye, C. Di Ding, L. H. Tan, and J. J. Fu, “Autonomous self-healing supramolecular elastomer reinforced and toughened by graphitic carbon nitride nanosheets tailored for smart anticorrosion coating applications,” *J. Mater. Chem. A*, vol. 6, no. 14, pp. 5887–5898, 2018, doi: 10.1039/c7ta09841c.
- [87] Y. Xia, Y. He, C. Chen, Y. Wu, F. Zhong, and J. Chen, “Co-modification of polydopamine and KH560 on g-C<sub>3</sub>N<sub>4</sub> nanosheets for enhancing the corrosion protection property of waterborne epoxy coating,” *React. Funct. Polym.*, vol. 146, p. 104405, 2020, doi: <https://doi.org/10.1016/j.reactfunctpolym.2019.104405>.
- [88] H. W. Choi, K. R. Lee, S. J. Park, R. Wang, J. G. Kim, and K. H. Oh, “Effects of plastic strain of diamond-like carbon coated stainless steel on the corrosion behavior in simulated body fluid environment,” *Surf. Coatings Technol.*, vol. 202, no. 12, pp. 2632–2637, 2008, doi: 10.1016/j.surfcoat.2007.09.046.
- [89] M. Marton *et al.*, “Electrochemical corrosion behavior of amorphous carbon nitride thin films,” *Vacuum*, vol. 86, no. 6, pp. 696–698, 2012, doi: 10.1016/j.vacuum.2011.07.053.
- [90] J. C. Caicedo *et al.*, “TiCN/TiNbCN multilayer coatings with enhanced mechanical properties,” *Appl. Surf. Sci.*, vol. 256, no. 20, pp. 5898–5904, 2010, doi: 10.1016/j.apsusc.2010.03.071.

- [91] J. Romero, J. Esteve, and A. Lousa, "Period dependence of hardness and microstructure on nanometric Cr/CrN multilayers," *Surf. Coatings Technol.*, vol. 188–189, no. 1-3 SPEC.ISS., pp. 338–343, 2004, doi: 10.1016/j.surfcoat.2004.08.058.
- [92] J. C. Caicedo *et al.*, "Corrosion surface protection by using titanium carbon nitride/titanium- niobium carbon nitride multilayered system," *Thin Solid Films*, vol. 519, no. 19, pp. 6362–6368, 2011, doi: 10.1016/j.tsf.2011.04.035.
- [93] P. B. Mirkarimi *et al.*, "The synthesis, characterization, and mechanical properties of thick, ultrahard cubic boron nitride films deposited by ion-assisted sputtering," *J. Appl. Phys.*, vol. 82, no. 4, pp. 1617–1625, 1997, doi: 10.1063/1.365961.
- [94] S. Ranganatha, T. V. Venkatesha, and K. Vathsala, "Electroless Ni-W-P coating and its nano-WS<sub>2</sub> composite: Preparation and properties," *Ind. Eng. Chem. Res.*, vol. 51, no. 23, pp. 7932–7940, 2012, doi: 10.1021/ie300104w.
- [95] P. Sahoo and S. K. Das, "Tribology of electroless nickel coatings – A review," *Mater. Des.*, vol. 32, no. 4, pp. 1760–1775, 2011, doi: <https://doi.org/10.1016/j.matdes.2010.11.013>.
- [96] S. Ranganatha and T. V. Venkatesha, "Fabrication and anticorrosion performance of Ni–P–BN nanocomposite coatings on mild steel," *Surf. Eng. Appl. Electrochem.*, vol. 53, no. 5, pp. 449–455, 2017, doi: 10.3103/S106837551705009X.
- [97] S. B. Sharma, R. C. Agarwala, V. Agarwala, and S. Ray, "DRY SLIDING WEAR AND FRICTION BEHAVIOR OF Ni–P–ZrO<sub>2</sub>–Al<sub>2</sub>O<sub>3</sub> COMPOSITE ELECTROLESS COATINGS ON ALUMINUM," *Mater. Manuf. Process.*, vol. 17, no. 5, pp. 637–649, Jan. 2002, doi: 10.1081/AMP-120016088.

- [98] K. N. Srinivasan and P. R. Thangavelu, "Electroless deposition of Ni-P composite coatings containing kaolin nanoparticles," *Trans. IMF*, vol. 90, no. 2, pp. 105–112, Mar. 2012, doi: 10.1179/0020296712Z.0000000009.
- [99] J. Hu, L. Fang, and P.-W. Zhong, "Effect of Reinforcement Particle Size on Fabrication and Properties of Composite Coatings," *Mater. Manuf. Process.*, vol. 28, no. 12, pp. 1294–1300, Dec. 2013, doi: 10.1080/10426914.2013.832298.
- [100] J. Roller, "X-ray diffraction," in *PEM Fuel Cell Diagnostic Tools*, 2011, pp. 289–313.
- [101] A. Mohammed and A. Abdullah, "Scanning Electron Microscopy (Sem): a Review," *Proc. 2018 Int. Conf. Hydraul. Pneum. - HERVEX*, no. January, p. 85, 2018.
- [102] M. Azad and A. Avin, "Scanning Electron Microscopy (SEM): A Review," *Proc. 2018 Int. Conf. Hydraul. Pneum. - HERVEX*, no. December, pp. 1–9, 2019.
- [103] R. T. G and A. B. R, "Review Article TRANSMISSION ELECTRON MICROSCOPY-AN OVERVIEW ISSN Online : - 2321-7855 International Research Journal for Inventions in TRANSMISSION ELECTRON MICROSCOPY- AN OVERVIEW," *Transm. Electron Microsc. Overv.*, no. March, 2019.
- [104] P. Nguyen-Tri, P. Ghassemi, P. Carriere, S. Nanda, A. A. Assadi, and D. D. Nguyen, "Recent applications of advanced atomic force microscopy in polymer science: A review," *Polymers (Basel)*, vol. 12, no. 5, pp. 1–28, 2020, doi: 10.3390/POLYM12051142.
- [105] A. W. Neumann and R. J. Good, "Techniques of Measuring Contact Angles," in *Surface and Colloid Science*, 1979, pp. 31–91.
- [106] G. K. Glass, C. L. Page, and N. R. Short, "Factors affecting the corrosion rate of

- steel in carbonated mortars,” *Corros. Sci.*, vol. 32, no. 12, pp. 1283–1294, 1991, doi: [https://doi.org/10.1016/0010-938X\(91\)90048-T](https://doi.org/10.1016/0010-938X(91)90048-T).
- [107] B. A. Shaw and R. G. Kelly, “What is corrosion?,” *Electrochem. Soc. Interface*, vol. 15, no. 1, pp. 24–26, 2006.
- [108] G. S. Frankel, “Fundamentals of corrosion kinetics,” in *Springer Series in Materials Science*, vol. 233, 2016, p. 17.
- [109] C. Li, Y. Wang, and Z. Pan, “Wear resistance enhancement of electroless nanocomposite coatings via incorporation of alumina nanoparticles prepared by milling,” *Mater. Des.*, vol. 47, pp. 443–448, 2013, doi: [10.1016/j.matdes.2012.12.021](https://doi.org/10.1016/j.matdes.2012.12.021).
- [110] G. S. Song, S. Sun, Z. C. Wang, C. Z. Luo, and C. X. Pan, “Synthesis and characterization of electroless Ni-P/Ni-Mo-P duplex coating with different thickness combinations,” *Acta Metall. Sin. (English Lett.)*, vol. 30, no. 10, pp. 1008–1016, 2017, doi: [10.1007/s40195-017-0603-6](https://doi.org/10.1007/s40195-017-0603-6).
- [111] M. Buchtík, M. Krystýnová, J. Másilko, and J. Wasserbauer, “The effect of heat treatment on properties of Ni-P coatings deposited on a AZ91 magnesium alloy,” *Coatings*, vol. 9, no. 7, 2019, doi: [10.3390/coatings9070461](https://doi.org/10.3390/coatings9070461).
- [112] W. Chen, W. Gao, and Y. He, “A novel electroless plating of Ni-P-TiO<sub>2</sub> nanocomposite coatings,” *Surf. Coatings Technol.*, vol. 204, no. 15, pp. 2493–2498, 2010, doi: [10.1016/j.surfcoat.2010.01.032](https://doi.org/10.1016/j.surfcoat.2010.01.032).
- [113] S. R. Allahkaram, A. Zarebidaki, and T. Rabizadeh, “Evaluation of Electroless Ni - P and Ni - P Nano-Composite Coatings’ Properties ,” *Int. J. Mod. Phys. Conf. Ser.*, vol. 05, pp. 817–824, 2012, doi: [10.1142/s2010194512002796](https://doi.org/10.1142/s2010194512002796).
- [114] D. R. Paul, S. Gautam, P. Panchal, S. P. Nehra, P. Choudhary, and A. Sharma, “ZnO-Modified g-C<sub>3</sub>N<sub>4</sub>: A Potential Photocatalyst for Environmental

- Application,” *ACS Omega*, vol. 5, no. 8, pp. 3828–3838, 2020, doi: 10.1021/acsomega.9b02688.
- [115] Chidhambaram N., Ravichandran K., “Fabrication of ZnO/g-C<sub>3</sub>N<sub>4</sub> nanocomposites for enhanced visible light driven photocatalytic activity,” 2017.
- [116] Y. P. Zhu, M. Li, Y. L. Liu, T. Z. Ren, and Z. Y. Yuan, “Carbon-Doped ZnO hybridized homogeneously with graphitic carbon nitride nanocomposites for photocatalysis,” *J. Phys. Chem. C*, vol. 118, no. 20, pp. 10963–10971, 2014, doi: 10.1021/jp502677h.
- [117] Z. Rajabalizadeh and D. Seifzadeh, “The effect of copper ion on microstructure, plating rate and anticorrosive performance of electroless Ni-P coating on AZ61 magnesium alloy,” *Prot. Met. Phys. Chem. Surfaces*, vol. 50, no. 4, pp. 516–523, 2014, doi: 10.1134/S2070205114040157.
- [118] Y. He, W. T. Sun, S. C. Wang, P. A. S. Reed, and F. C. Walsh, “An electrodeposited Ni-P-WS<sub>2</sub> coating with combined super-hydrophobicity and self-lubricating properties,” *Electrochim. Acta*, vol. 245, pp. 872–882, 2017, doi: 10.1016/j.electacta.2017.05.166.
- [119] S. Karthikeyan and L. Vijayaraghavan, “Investigation of the surface properties of heat treated electroless Ni–P coating,” *Trans. Inst. Met. Finish.*, vol. 94, no. 5, pp. 265–273, 2016, doi: 10.1080/00202967.2016.1208861.
- [120] W. Zhang, X. Feng, H. Cao, A. Hu, and M. Li, “Influence of PEG molecular weight on morphology, structure and wettability of electroless deposited Cu-Ni-P films,” *Appl. Surf. Sci.*, vol. 258, no. 22, pp. 8814–8818, 2012, doi: 10.1016/j.apsusc.2012.05.096.
- [121] J. N. Balaraju and K. S. Rajam, “Influence of particle size on the microstructure, hardness and corrosion resistance of electroless Ni – P – Al<sub>2</sub>O<sub>3</sub> composite

- coatings,” vol. 200, pp. 3933–3941, 2006, doi: 10.1016/j.surfcoat.2005.03.007.
- [122] B. Liu, L. R. Liu, and X. J. Liu, “Effects of carbon nanotubes on hardness and internal stress in Ni-P coatings,” *Surf. Eng.*, vol. 29, no. 7, pp. 507–510, 2013, doi: 10.1179/1743294413Y.0000000152.
- [123] Radwan A. Bahgat, Ali Kamran, Shakoor R.A., Mohammed Himyan, Alsalama Taif, M. Yusuf Moinuddin, M. Abdullah Aboubakr, Montemor M. Fatima, Helal Mohamed, “Properties enhancement of Ni-P electrodeposited coatings by the incorporation of nanoscale Y2O3 particles,” *Appl. Surf. Sci.*, vol. 457, pp. 956–967, 2018.
- [124] A. Salicio-Paz *et al.*, “Monolayered versus multilayered electroless NiP coatings: Impact of the plating approach on the microstructure, mechanical and corrosion properties of the coatings,” *Surf. Coatings Technol.*, vol. 368, no. December 2018, pp. 138–146, 2019, doi: 10.1016/j.surfcoat.2019.04.013.
- [125] C. Su, W. Wu, Z. Li, and Y. Guo, “Prediction of film performance by electrochemical impedance spectroscopy,” *Corros. Sci.*, vol. 99, pp. 42–52, 2015, doi: 10.1016/j.corsci.2015.05.029.
- [126] E. M. Fayyad, M. A. Almaadeed, A. Jones, and A. M. Abdullah, “Evaluation techniques for the corrosion resistance of self-healing coatings,” *Int. J. Electrochem. Sci.*, vol. 9, no. 9, pp. 4989–5011, 2014.
- [127] L. K. Xu and J. D. Scantlebury, “A study on the deactivation of an IrO<sub>2</sub>–Ta<sub>2</sub>O<sub>5</sub> coated titanium anode,” *Corros. Sci.*, vol. 45, no. 12, pp. 2729–2740, 2003, doi: [https://doi.org/10.1016/S0010-938X\(03\)00108-2](https://doi.org/10.1016/S0010-938X(03)00108-2).
- [128] F. M. AlAbbas *et al.*, “Influence of sulfate reducing bacterial biofilm on corrosion behavior of low-alloy, high-strength steel (API-5L X80),” *Int. Biodeterior. Biodegradation*, vol. 78, pp. 34–42, 2013, doi:

<https://doi.org/10.1016/j.ibiod.2012.10.014>.

- [129] B. W. A. Sherar, I. M. Power, P. G. Keech, S. Mitlin, G. Southam, and D. W. Shoesmith, “Characterizing the effect of carbon steel exposure in sulfide containing solutions to microbially induced corrosion,” *Corros. Sci.*, vol. 53, no. 3, pp. 955–960, 2011, doi: <https://doi.org/10.1016/j.corsci.2010.11.027>.
- [130] A. S. Nguyen, M. Musiani, M. E. Orazem, N. Pébère, B. Tribollet, and V. Vivier, “Impedance study of the influence of chromates on the properties of waterborne coatings deposited on 2024 aluminium alloy,” *Corros. Sci.*, vol. 109, pp. 174–181, 2016, doi: [10.1016/j.corsci.2016.03.030](https://doi.org/10.1016/j.corsci.2016.03.030).
- [131] S. M. F. Gad El-Rab, S. A. Fadl-allah, and A. A. Montser, “Improvement in antibacterial properties of Ti by electrodeposition of biomimetic Ca–P apatite coat on anodized titania,” *Appl. Surf. Sci.*, vol. 261, pp. 1–7, 2012, doi: <https://doi.org/10.1016/j.apsusc.2012.05.139>.
- [132] M. Benoit *et al.*, “Comparison of different methods for measuring the passive film thickness on metals,” *Electrochim. Acta*, vol. 201, pp. 340–347, 2016, doi: <https://doi.org/10.1016/j.electacta.2015.12.173>.
- [133] T. Rabizadeh, S. R. Allahkaram, and A. Zarebidaki, “An investigation on effects of heat treatment on corrosion properties of Ni-P electroless nano-coatings,” *Mater. Des.*, vol. 31, no. 7, pp. 3174–3179, 2010, doi: [10.1016/j.matdes.2010.02.027](https://doi.org/10.1016/j.matdes.2010.02.027).
- [134] C. Liu and Q. Zhao, “Influence of surface-energy components of Ni-P-TiO<sub>2</sub>-PTFE nanocomposite coatings on bacterial adhesion,” *Langmuir*, vol. 27, no. 15, pp. 9512–9519, 2011, doi: [10.1021/la200910f](https://doi.org/10.1021/la200910f).
- [135] Q. Zhao and Y. Liu, “Modification of stainless steel surfaces by electroless Ni-P and small amount of PTFE to minimize bacterial adhesion,” *J. Food Eng.*, vol.



72, no. 3, pp. 266–272, 2006, doi: 10.1016/j.jfoodeng.2004.12.006.

- [136] Z. Sharifalhosseini, M. H. Entezari, and R. Jalal, “Evaluation of antibacterial activity of anticorrosive electroless Ni-P coating against *Escherichia coli* and its enhancement by deposition of sono-synthesized ZnO nanoparticles,” *Surf. Coatings Technol.*, vol. 266, pp. 160–166, 2015, doi: 10.1016/j.surfcoat.2015.02.035.
- [137] K. Rasool and D. S. Lee, “Inhibitory effects of silver nanoparticles on removal of organic pollutants and sulfate in an anaerobic biological wastewater treatment process,” *J. Nanosci. Nanotechnol.*, vol. 16, no. 5, pp. 4456–4463, 2016, doi: 10.1166/jnn.2016.10984.
- [138] J. A. Lemire, J. J. Harrison, and R. J. Turner, “Antimicrobial activity of metals: Mechanisms, molecular targets and applications,” *Nat. Rev. Microbiol.*, vol. 11, no. 6, pp. 371–384, 2013, doi: 10.1038/nrmicro3028.
- [139] M. Honarkar Ashna, M. Behzad, and M. Salehi, “Nickel versus copper: Enhanced antibacterial activity in a series of new nickel(II) Schiff base complexes,” *J. Coord. Chem.*, vol. 69, no. 2, pp. 190–198, 2016, doi: 10.1080/00958972.2015.1117073.
- [140] D. Rattan Paul and S. P. Nehra, “Graphitic carbon nitride: a sustainable photocatalyst for organic pollutant degradation and antibacterial applications,” *Environ. Sci. Pollut. Res.*, vol. 28, no. 4, pp. 3888–3896, 2021, doi: 10.1007/s11356-020-09432-6.
- [141] J. Chen, W. Lin, L. Xie, J. Huang, and W. Wang, “Templated fabrication of graphitic carbon nitride with ordered mesoporous nanostructures for high-efficient photocatalytic bacterial inactivation under visible light irradiation,” *J. Nanomater.*, vol. 2019, 2019, doi: 10.1155/2019/3242136.

- [142] M. Oves, M. O. Ansari, R. Darwesh, A. Hussian, M. F. Alajmi, and H. A. Qari, “Synthesis and antibacterial aspects of graphitic c3n4@polyaniline composites,” *Coatings*, vol. 10, no. 10, pp. 1–12, 2020, doi: 10.3390/coatings10100950.
- [143] B. Abebe, E. A. Zereffa, A. Tadesse, and H. C. A. Murthy, “A Review on Enhancing the Antibacterial Activity of ZnO: Mechanisms and Microscopic Investigation,” *Nanoscale Res. Lett.*, vol. 15, no. 1, 2020, doi: 10.1186/s11671-020-03418-6.
- [144] M. Lorenzetti *et al.*, “The influence of surface modification on bacterial adhesion to titanium-based substrates,” *ACS Appl. Mater. Interfaces*, vol. 7, no. 3, pp. 1644–1651, 2015, doi: 10.1021/am507148n.
- [145] K. Yamauchi, Y. Yao, T. Ochiai, M. Sakai, Y. Kubota, and G. Yamauchi, “Antibacterial activity of hydrophobic composite materials containing a visible-light-sensitive photocatalyst,” *J. Nanotechnol.*, vol. 2011, 2011, doi: 10.1155/2011/380979.

## APPENDICES

### Appendix A: TEM Analysis for $C_3N_4/ZnO$ Nanocapsules

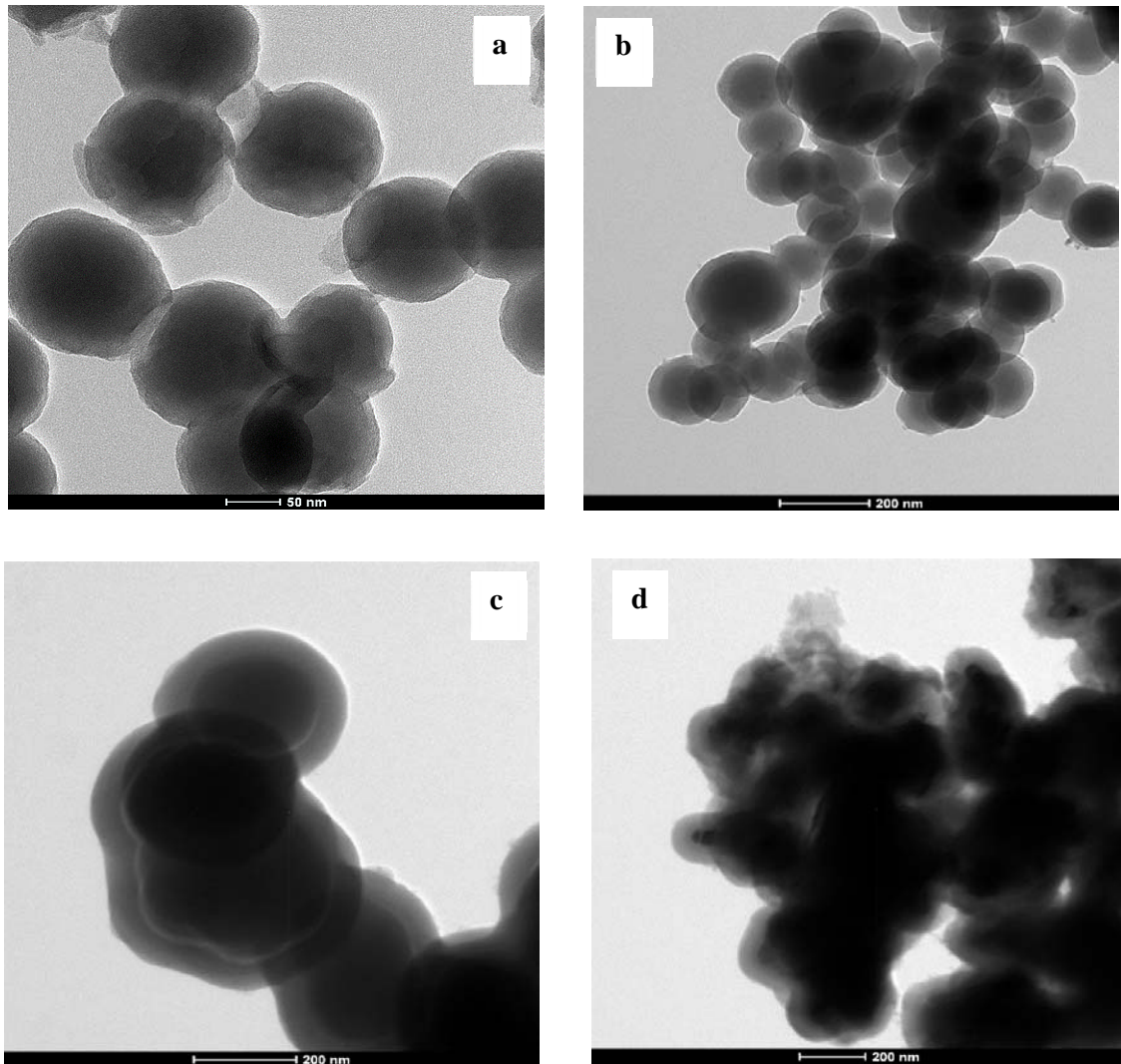


Figure 48. TEM measurements for  $C_3N_4$  nanocapsules (undoped) (a), and doped  $C_3N_4$  with (b) 0.5, (c) 1.0 and (d) 2.0 g ZnO

## Appendix B: BET Measurements

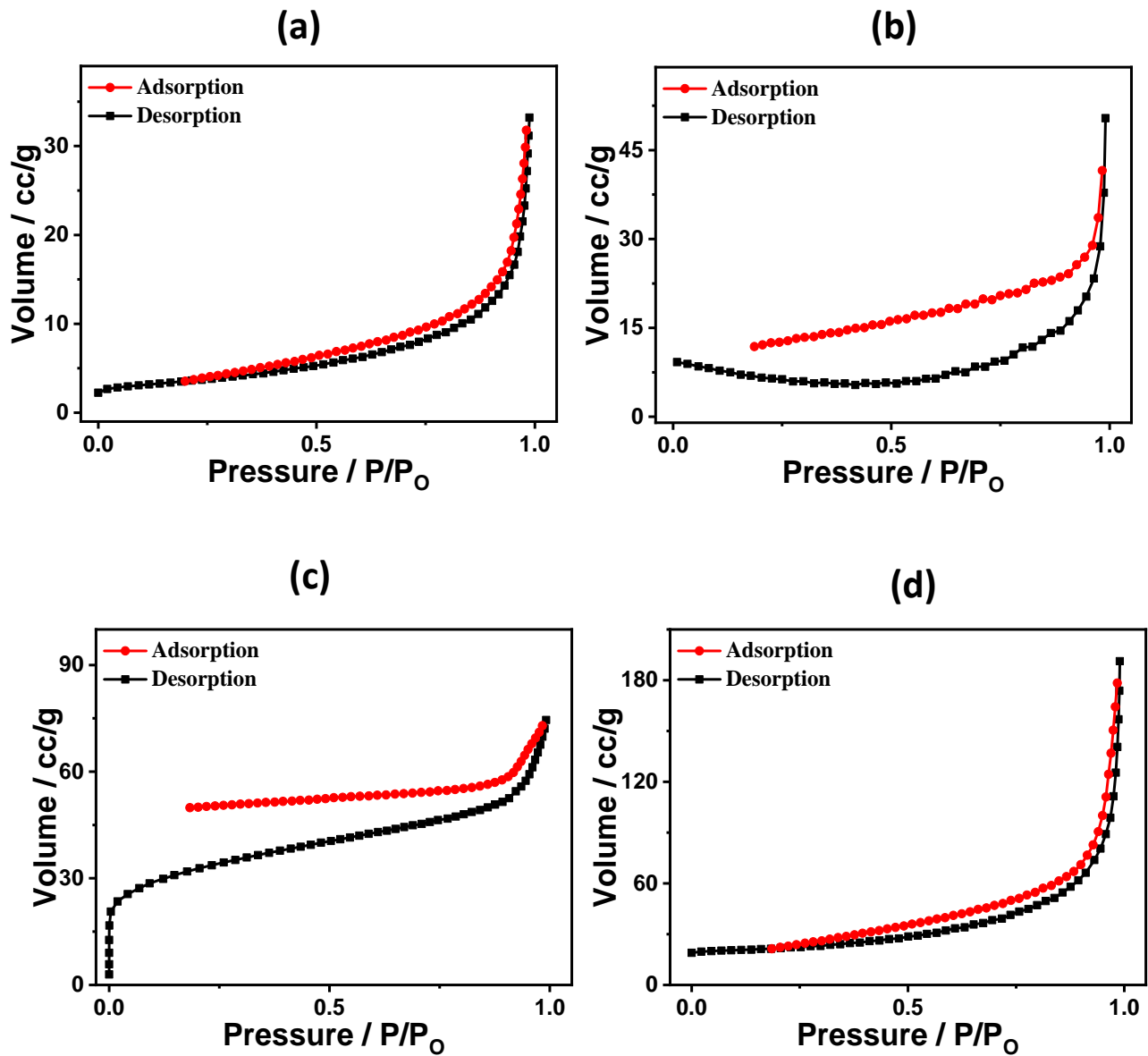


Figure 49. N<sub>2</sub> adsorption-desorption isotherms at 77 K for mesoporous g-C<sub>3</sub>N<sub>4</sub> nanocapsules doped with (a) 0.0 , (b) 0.5 , (c) 1.0 and (d) 2.0g ZnO, respectively.

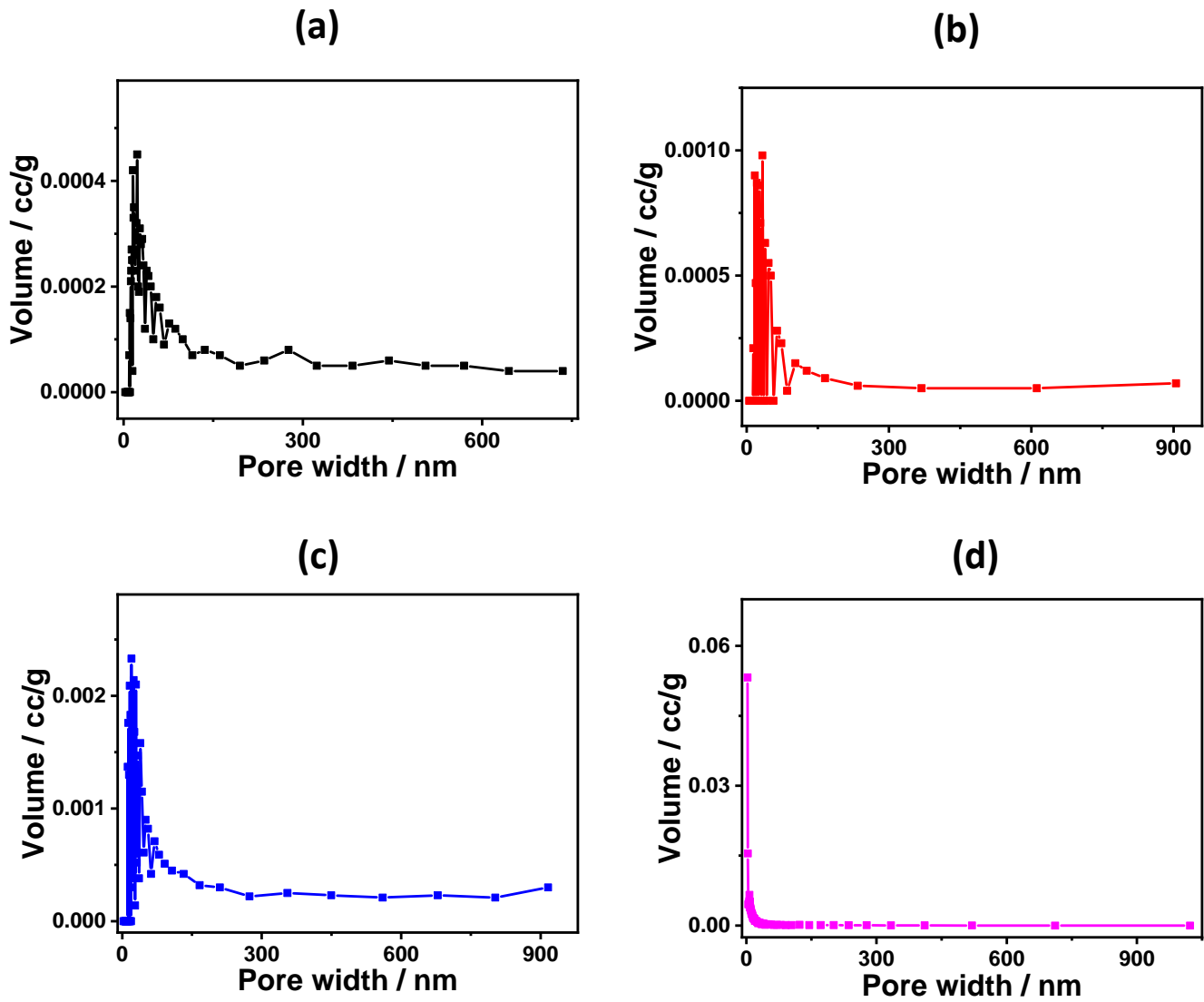


Figure 50. Pore size and volume characterization for mesoporous g-C<sub>3</sub>N<sub>4</sub> nanocapsules doped with (a) 0.0 , (b) 0.5 , (c) 1.0 , and (d) 2.0g ZnO, respectively